Ultrafast Terahertz Response of Epitaxial and Chemical-Vapor-Deposited Graphene and of Germanium and Germanium/Silicon Core/Shell Nanowires

by

Momchil Tsvetanov Mihnev

A dissertation submitted in partial fulfillment
of the requirements for the degree of
Doctor of Philosophy
(Electrical Engineering)
in the University of Michigan
2015

Doctoral Committee:

Professor Theodore B. Norris, Chair
Professor Cagliyan Kurdak
Associate Professor Wei Lu
Professor Duncan G. Steel
Associate Professor Zhaohui Zhong

© Momchil Tsvetanov Mihnev
All Rights Reserved
2015

To my loving family.

Acknowledgements

First and foremost I would like to thank my family for their boundless love, care, support, patience and encouragement during my doctoral studies. I would not have been able to complete my degree without them. To my family, I say "I love you!"

The research work presented in this dissertation would not have been possible if it was not for my numerous mentors, colleagues, collaborators and friends.

I am sincerely grateful to my research advisor Prof. Theodore Norris for generously giving me the opportunity to pursue my academic aspirations and for kindly guiding me on my doctoral journey. I would also like to thank my dear colleagues and friends in our group, Charles Divin, Dong Sun, Yunbo Guo, Malakeh Musheinesh, Jessica Ames, Pacha Mongkolwongrojn, You-Chia Chang, Miao-Bin Lien, Heather Ferguson, Laura Elgin, Gong Cheng and Nooshin Mohammadi Estakhri, for their immense help, friendship and enthusiasm. I am particularly indebted to Charles for laying the foundation of the terahertz spectroscopy work in our lab. Very special thank you also to Steve Katnik for his tremendous and indispensable assistance with the ultrafast laser system.

I am also deeply grateful to my close collaborators and friends for their valuable and vital collaboration on our joint projects. It was my enormous privilege to work with such a brilliant team of renowned experts from all over the world and I feel truly fortunate.

On the graphene project, I would like to thank Prof. Walt de Heer and Dr. Claire Berger for providing the multilayer epitaxial graphene and epitaxial graphene nanoribbons, and Prof. Edward Conrad and Feng Wang for providing the buckled epitaxial graphene. I would also like to thank Prof. Zhaohui Zhong, Seunghyun Lee and Che-Hung Liu for providing the polycrystalline chemical-vapor-deposited graphene, and Prof. Rodney Ruoff and Xiaohan Wang for providing the single-crystal chemical-vapor-deposited graphene.

All of these exceptional state-of-the-art samples enabled me to perform my experimental studies. I would also like to acknowledge Prof. Andreas Knorr, Dr. Ermin Malic, Dr. Torben Winzer and Faris Kadi for developing the microscopic theory of carrier-carrier and carrier-phonon interactions in graphene, and Prof. Allan MacDonald and John Tolsma for developing the interlayer energy transfer theory of screened Coulomb interactions in multilayer epitaxial graphene. I need to point out that precisely the union of theory and experiment was the key to our exciting discoveries.

On the semiconductor nanowire project, I would like to thank Prof. Wei Lu, Wayne Fung and Ugo Otuonye for providing the germanium and germanium/silicon core/shell nanowires. These outstanding state-of-the-art samples represented a fascinating system for my experimental investigations. I would also like to acknowledge Prof. Mackillo Kira and Phillip Springer for their important collaboration on the microscopic theory calculations of exciton response and quantum confinement effects in the semiconductor nanowires. I should again note that the combination of theory and experiment was the source of our interesting findings.

Finally, I would like to express my profound gratitude to the other two members of my doctoral committee, Prof. Duncan Steel and Prof. Cagliyan Kurdak, for their vast curiosity in and kind recognition of my research work. I especially appreciate the mentoring of Prof. Duncan Steel, who is a source of infinite inspiration for me and is one of the main reasons for my chosen path.

Table of Contents

List of Figures

List of Tables

Abstract

Nanotechnology has recently enjoyed a tremendous interest, and many emerging nanoscale and low-dimensional materials and devices are under active investigation. This dissertation presents research work on the physics of the ultrafast terahertz (THz) response and the hot-carrier dynamics in two sample classes of state-of-the-art materials, namely graphene and semiconductor nanowires, by using ultrafast time-resolved THz spectroscopy. Thorough understanding of this physics is indispensable for the implementation of novel high-speed nanoelectronic and nanophotonic devices based on these materials.

The dynamic THz response of a wide variety of high-quality graphene, including epitaxial and chemical-vapor-deposited, is systematically studied. In pristine epitaxial and chemical-vapor-deposited graphene, the dynamics depend critically on the doping density with relaxation times ranging from a few picoseconds in highly doped to hundreds of picoseconds in quasi-neutral layers; a microscopic density-matrix theory of carrier-carrier and carrier-phonon interactions accounts quantitatively for the experimental results. In multilayer epitaxial graphene with a few highly doped and many lightly doped layers, low-energy relaxation times of hundreds of picoseconds are measured in the lightly doped layers consistent with a first-principles theory of interlayer energy transfer via screened Coulomb interactions. In semiconducting epitaxial graphene, the relaxation of the dynamics is up to two orders of magnitude faster relative to metallic epitaxial graphene attributed to large enhancement of the phase-space available for carrier scattering due to an energy gap. In epitaxial graphene nanoribbons, a highly anisotropic response arises from two-dimensional quantum confinement with carrier lifetimes of tens of picoseconds in the high-energy subbands.

The dynamic THz response of quasi-one-dimensional high-quality single-crystal germanium and germanium/silicon core/shell nanowires is also extensively investigated. The dynamics are characterized by fast few-picosecond intraband carrier relaxation followed by slower sub-nanosecond interband carrier recombination processes. Clear evidence for ballistic carrier transport on tens of nanometers is observed, and surface defect states are identified as the dominant carrier recombination and scattering mechanism limiting carrier lifetime and transport. Three possible physical origins giving rise to the observed highly anisotropic response are considered including free-carrier response, exciton response and quantum confinement effects.

Chapter 1
Introduction

Section 1.1 Dissertation Motivation and Organization

Nanotechnology has for some time appeared to be the natural next state in the evolution of modern technology. Specifically, in electronics and photonics, the insatiable desire for ever smaller, faster, more powerful, less power-consuming, less expensive, more portable and in general more pervasive devices and systems has been long being appeased by "Cramming more components onto integrated circuits" [1], and has driven these technologies well into the nanoscale world. Not surprisingly, the research work into novel nanoscale and low-dimensional materials and devices has recently experienced astoundingly rapid progress fueled largely by a plethora of exciting applications in nanoelectronics and nanophotonics. Some of the most prominent applications include field-effect transistors, p-n junction diodes, lasers, light-emitting diodes, photodetectors, solar cells and optical modulators.

In this dissertation, I study systematically the physics of the ultrafast terahertz (THz) response and the hot-carrier relaxation and cooling dynamics in two sample classes of state-of-the-art nanoscale low-dimensional materials, namely graphene and semiconductor nanowires. Both graphene and semiconductor nanowires have shown remarkable technological potential and have attracted tremendous interest by the scientific and engineering community. Graphene, a monolayer of carbon atoms arranged in a two-dimensional (2D) honeycomb lattice, has been known and studied for decades in different forms [2, 3, 4], but it was not until the pioneering research work in the early 2000s [5, 6, 7, 8, 9], when graphene was truly and widely recognized. Graphene boasts exceptionally high carrier mobility, excellent thermal conductivity, very long ballistic carrier mean free path and strong light-matter interaction among other supreme properties [10, 11, 12]. Within the brief timespan of about a decade, it began to be often referred to as a “wonder

material". Semiconductor nanowires, cylindrical semiconductor structures with nanometer size diameters, were synthesized for the first time in the late 1990s. They also exhibit unique electronic and optical properties stemming from their quasi-1D nanostructure and possible quantum confinement effects [13, 14, 15, 16]. A particularly intriguing feature is the ability to synthesis semiconductor nanowires from the bottom-up with precise nanoscale control over their structure and composition, and then combine these diverse building blocks into larger and more complex functional systems.

Graphene and semiconductor nanowires are among the emerging candidates for the industrial realization of novel, scalable, highly-integrated, multifunctional, high-performance nanoelectronic and nanophotonic devices and systems operating into the THz frequencies. The design and development of such devices based on these two classes of materials would require further advances on both the science and the technology fronts. Firstly, the thorough understanding of the physics of their dynamic response and electronic transport up to THz frequencies is indispensable. Secondly, the device operation at these high frequencies would rely on high-energy and possibly ballistic carriers, and hence the hot-carrier behavior and the mechanisms responsible for carrier relaxation, cooling and recombination is essential. Thirdly, the electronic and optical properties and the nature of light-matter interaction in these nanoscale structures would be strongly influenced by quantum confinement, and hence these effects are critical. Finally, the ability to fabricate these devices in large quantities, with the same quality and with high yield is also vital. Previously, the semiconductor and optical communications technologies succeeded in establishing themselves as mature industries, because their components could be produced in the millions and by the kilometers with exceptional reliability.

In this research work, I utilize ultrafast time-resolved THz spectroscopy, which is a relatively new experimental technique emerging in the late 1980s, when it was first demonstrated that near single-cycle THz pulses can be generated, propagated through free space and detected in the time-domain [17, 18, 19]. The THz spectroscopy has experienced very rapid development and found a wide spectrum of applications including in chemistry, biology, medicine and pharmaceuticals for chemical analysis and molecular spectroscopy, in physics for material spectroscopy and light-matter interaction studies in condensed-

matter systems, and in engineering for THz imaging, remote sensing and failure analysis [20, 21]. Relevant for the area of material spectroscopy, this experimental technique has a number of useful characteristics including being convenient (could be used both in research and industrial settings), direct (directly accesses light-matter interaction), ultrafast (has sub-picosecond temporal resolution), broadband (has one decade or more spectral bandwidth), sensitive (can measure the response of a single atomic layer such as graphene), non-contact (does not require electrical contacts, which can largely complicate the interpretation of the experimental results), and non-destructive (does not require special irreversible material processing and does not physically alter the material). In addition, the THz (also referred to as far-infrared) radiation lies right between low electronics frequencies and high photonics frequencies in the so-called "THz gap" and can be considered as a natural bridge between electronics and photonics. Hence, the ultrafast time-resolved THz spectroscopy is an ideal tool for investigating the physics of the ultrafast THz response and the hot-carrier relaxation and cooling dynamics in nanoscale low-dimensional materials such as graphene and semiconductor nanowires.

The dissertation is organized as follows. In Section 1.2, we first introduce the ultrafast time-resolved THz spectroscopy technique, which we use to study the dynamic THz response and the hot-carrier relaxation and cooling dynamics in graphene and semiconductor nanowires. We describe essential details of the experimental set-up and the data analysis procedure.

In Chapter 2, we discuss the dynamic THz response and the hot-carrier dynamics of graphene following ultrafast photoexcitation. We look at a wide variety of high quality graphene, including epitaxial and chemical-vapor-deposited (CVD). In Section 2.1, we first introduce graphene, focusing on the studied epitaxial and CVD types of graphene, and its electronic and optical properties. In Section 2.2, we discuss the dynamic THz response of pristine epitaxial and CVD graphene, which is characteristic for a pristine disorder-free graphene layer. In Section 2.3, we discuss the dynamic THz response of multilayer epitaxial graphene, in which interlayer interactions play an important role. In Section 2.4, we discuss the dynamic THz response of buckled epitaxial graphene, in which an energy gap has been carefully engineered. In Section 2.5, we discuss the dynamic THz response

of epitaxial graphene nanoribbons, in which quantum confinement effects become prominent. In Section 2.6, we finally present a brief summary of the results in Chapter 2.

In Chapter 3, we discuss the dynamic THz response and the hot-carrier dynamics of semiconductor nanowires following ultrafast photoexcitation. We look specifically at high quality single-crystal germanium (Ge) and germanium/silicon (Ge/Si) core/shell nanowires (NWs). In Section 3.1, we first introduce the studied Ge and Ge/Si core/shell NWs. In Section 3.2, we discuss the THz carrier dynamics of the NWs. In Section 3.3, we discuss the full dynamic THz response of the NWs. In Section 3.4, we finally present a brief summary of the results in Chapter 3.

In Chapter 4, we present a brief conclusion of the research work in this dissertation and remarks on some further directions in which the work can be continued in the future.

Section 1.2 Ultrafast Time-Resolved THz Spectroscopy

To study the dynamic THz response of graphene and semiconductor nanowires following ultrafast photoexcitation, we utilize ultrafast time-resolved THz spectroscopy [17, 18, 19]. The ultrafast time-resolved THz spectroscopy has established itself as a very powerful all-optical experimental technique for directly probing the relaxation and cooling dynamics of photoexcited carriers in wide variety of condensed-matter and solid-state systems, because it is sensitive to both the number of carriers and their distribution in energy. The experimental set-up is illustrated schematically in Figure 1.2.1. Our laser system consists of a Ti:Sapphire oscillator (Mira 900-F, Coherent) followed by a Ti:Sapphire regenerative amplifier (RegA 9050, Coherent) and produces ultrafast optical pulses with a center wavelength of 800 nm, a pulse width of ~60 fs and a repetition rate of 250 kHz. A portion of the laser beam is quasi-collimated at the sample position with an intensity spot size diameter of ~1600 μm, and optically injects hot carriers in the samples. A second portion of the laser beam is used to generate a single-cycle THz pulse in a low temperature grown GaAs photoconductive emitter (Tera-SED 3/4, Gigaoptics) [22, 23] and the emitted broadband THz radiation is focused on the sample with an intensity spot size diameter of ~500 μm to probe the dynamic THz response. The transmitted portion of the THz probe is detected by using time-domain electro-optic sampling in a 1 mm thick ZnTe crystal [24, 25, 26] and a pair of balanced Si photodiodes. The electrical signal is modulated

by a mechanical chopper, placed in either the optical pump or the THz probe arm, and recorded by using a conventional lock-in amplifier data acquisition technique. The sample is mounted inside a liquid helium continuous flow cryostat (ST-100, Janis), so that the substrate temperature can be varied from 10 K to 300 K. The time delays between the optical pump, the THz probe and the sampling pulse are controlled by two motorized stages. All THz optics is surrounded by an enclosure purged with purified nitrogen gas to minimize water vapor absorption. The detection bandwidth of the system is in the range of ~0.2-2.5 THz and the temporal resolution of the measurements is limited by the duration of the THz probe pulse to the sub-picosecond timescale. The experimental error is due primarily to long-term drift of the optomechanical components and the ultrafast Ti:Sapphire laser system, and is estimated not to exceed ~5%.

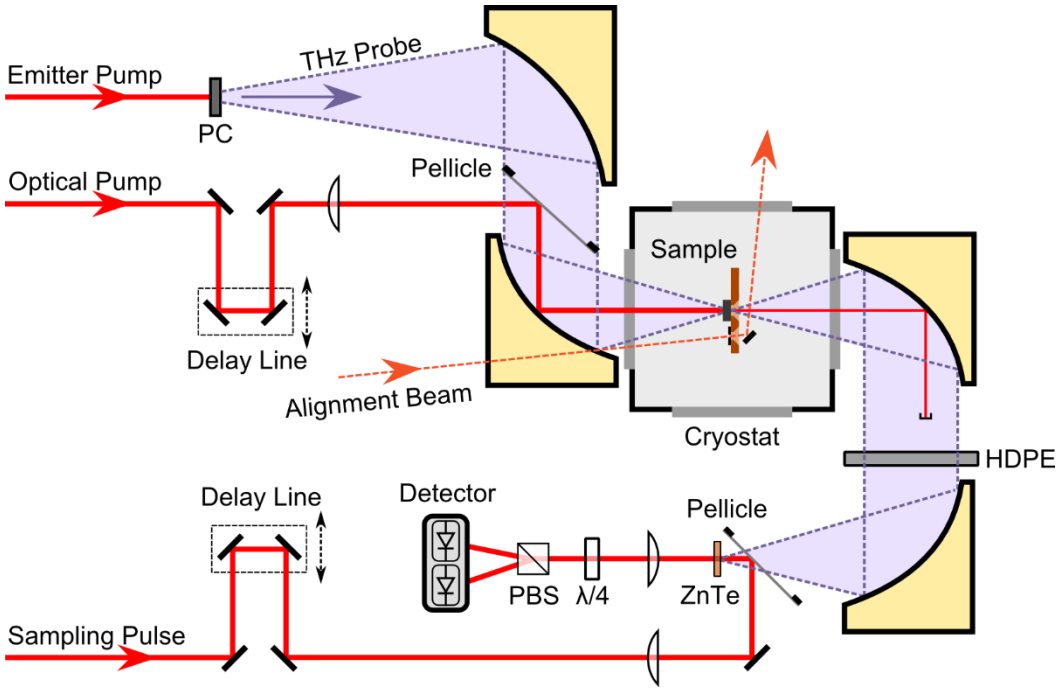

Figure 1.2.1 – Schematic diagram of the ultrafast time-resolved THz spectroscopy set-up.

The ultrafast time-resolved THz spectroscopy is essentially a three-pulse spectroscopic technique and each of the three pulses has independent temporal and spatial positions. Figure 1.2.2(a) shows the pulse timing between the three pulses including the optical pump pulse, the THz probe pulse and the sampling pulse. The optical pump and THz probe interact at the sample position, while the sampling pulse and the THz probe interact at the ZnTe detection crystal position. Hence, the pulse timing involves two

independent time delays – the time delay between the optical pump and the THz probe at the sample position, $\tau_{pump-probe}$, and the time delay between the sampling pulse and the THz probe at the ZnTe detection crystal position, $\tau_{sampling-probe}$. Thus, the experimentally measured THz signal is a function of both $\tau_{pump-probe}$ and $\tau_{sampling-probe}$, and in general we need to scan both time delays to extract the dynamic THz response of the sample. In practice, we fix one of the time delays at discrete values and we scan continuously the other time delay to record the THz signal. This implies two separate experimental approaches.

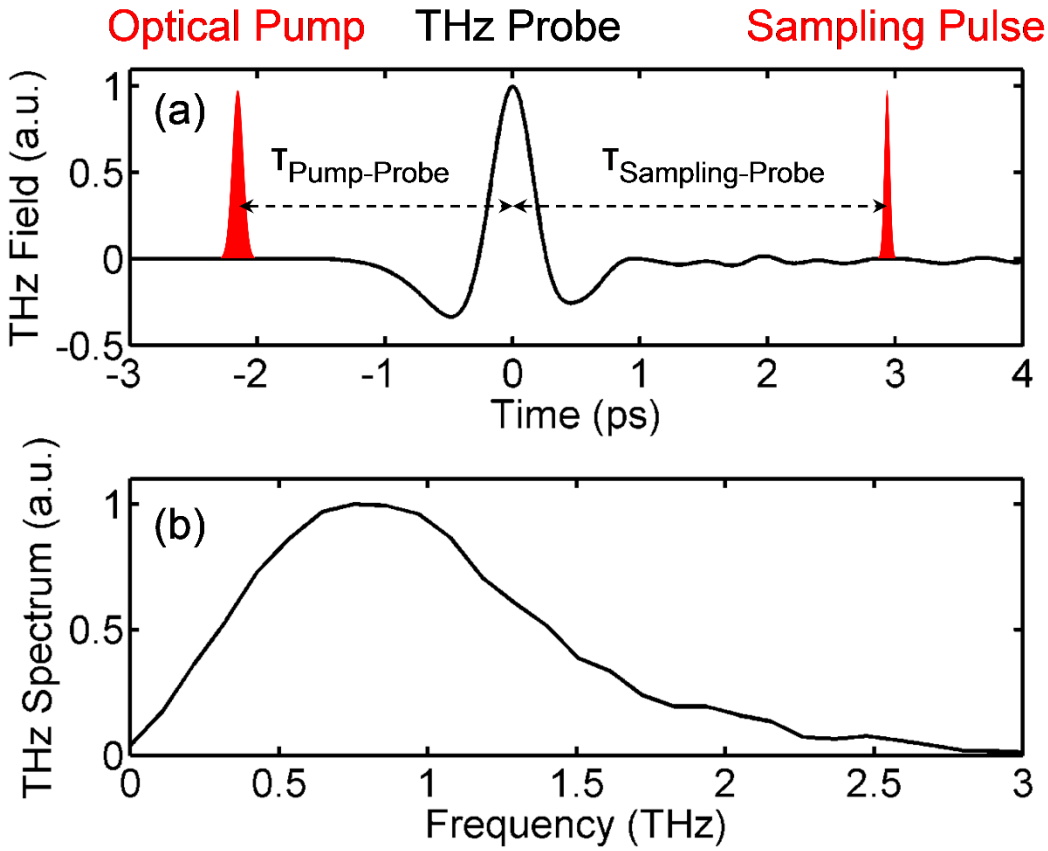

Figure 1.2.2 – Ultrafast time-resolved THz spectroscopy in (a) time and (b) frequency domain.

In the first experimental approach, we fix the pump-probe delay and we scan the sampling-probe delay to measure the full time-domain THz probe pulse transmission. From the measured time-domain THz electric field, $E(t)$, we can obtain the frequency-domain THz spectrum, $E(\omega)$, by straightforward numerical Fourier transformation as shown in Figure 1.2.2(b). By recording the THz transmission both without photoexcitation by the

optical pump and with photoexcitation for different THz probe delays after the optical pump, we extract the full dynamic THz response of the sample. In the second experimental approach, we fix the sampling-probe delay (usually the peaks of the sampling and the probe pulses overlap to maximize the measured THz signal) and we scan the pump-probe delay to measure the relaxation of the THz probe pulse transmission. Again, by recording the THz transmission both without and with photoexcitation by the optical pump, we extract the transient THz carrier dynamics of the sample. In this dissertation, we apply both experimental approaches to study the graphene and the semiconductor nanowire samples.

The next important step is the analysis of the experimental data recorded in ultrafast time-resolved THz spectroscopy. The key issue is to relate the THz transmission (the experimental quantity that we measure) to the dynamic THz response of the studied sample or material (the physical quantity that we are interested in). In general, this relationship is very complex, but it can be simplified within some approximation to allow gaining useful physical insight into the dynamic THz response [27, 28, 29].

First, we describe the interaction of the THz probe with the studied sample. The THz electric field, $E(t)$, incident on the sample at a time delay τ after ultrafast photoexcitation by the optical pump, sets up a transient macroscopic current density, $j(t,\tau)$, given by [29]:

$$j(t,\tau) = \int_{-\infty}^{+\infty} E(t')g(t,t',\tau)dt', \qquad (1.2.1)$$

where $g(t,t',\tau)$ is the current response function of the sample. Upon photoexcitation, the optical pump creates a non-equilibrium photoexcited carrier density, $n(\tau)$, which decays with the delay τ. Every photoexcited carrier contributes a portion of the total macroscopic current density via its single-carrier current response function, $g_0(t)$, upon interacting with a delta-function incident THz electric field. Hence, the current response function can be decomposed into $g(t,t',\tau) = n(t'+\tau)g_0(t-t')$ and the macroscopic current density becomes:

$$j(t,\tau) = \int_{-\infty}^{+\infty} E(t')n(t'+\tau)g_0(t-t')dt'. \qquad (1.2.2)$$

Equation 1.2.2 can be rewritten as a straight-forward convolution:

$$j(t,\tau) = [E(t)n(t+\tau)] * [g_0(t)]. \quad (1.2.3)$$

If we assume that the photoexcited carrier density decays slowly on a timescale compared to the duration of the THz probe pulse, which implies that $n(\tau)$ is in a quasi-steady state, Equation 1.2.3 can be conveniently simplified to:

$$j(t,\tau) = n(\tau)([E(t)] * [g_0(t)]). \quad (1.2.4)$$

By Fourier transforming Equation 1.2.4, we obtain:

$$j(\omega,\tau) = n(\tau)\varsigma(\omega)E(\omega), \quad (1.2.5)$$

where $\varsigma(\omega)$ is the single-carrier conductivity. By defining the quasi-conductivity of the sample as $\sigma(\omega,\tau) = n(\tau)\varsigma(\omega)$, we obtain the well-known Ohm's Law:

$$j(\omega,\tau) = \sigma(\omega,\tau)E(\omega). \quad (1.2.6)$$

Next, we describe the transmission of the THz probe through the studied sample. The THz electric field, $E_t(t,\tau)$, transmitted through the sample at a time delay τ after ultrafast photoexcitation by the optical pump is related to the incident THz electric field, $E(t)$, via:

$$E_t(t,\tau) = \int_{-\infty}^{+\infty} E(t')h(t,t',\tau)dt', \quad (1.2.7)$$

where $h(t,t',\tau)$ is the transmission response function of the sample. If we assume that the sample is a linear and time-invariant system, Equation 1.2.7 can be conveniently simplified to:

$$E_t(t,\tau) = \int_{-\infty}^{+\infty} E(t')h(t-t',\tau)dt'. \quad (1.2.8)$$

Equation 1.2.8 can be rewritten as a straight-forward convolution:

$$E_t(t,\tau) = [E(t)] * [h(t,\tau)]. \quad (1.2.9)$$

By Fourier transforming Equation 1.2.9, we obtain:

$$E_t(\omega,\tau) = H(\omega,\tau)E(\omega), \quad (1.2.10)$$

where $H(\omega,\tau)$ is the transmission transfer function of the sample. We note that the approximations we made in deriving Equations 1.2.6 and 1.2.10 are essentially equivalent

in that the sample is assumed to be a linear and time-invariant system. Another necessary assumption is that the sample is sufficiently thin compared to the skin depth of both the optical pump and the THz probe, so that it is uniformly and homogenously photoexcited and probed.

Finally, we relate the measured THz transmission to the dynamic THz response of the studied sample. To achieve that we need to express the transmission transfer function of the sample $H(\omega,\tau)$ in terms of its THz response. There are a few different standard electromagnetic approaches to obtain the electromagnetic transmission through an arbitrary system, which is modeled by its electromagnetic response expressed, for example, by its permittivity $\epsilon(\omega)$, its conductivity $\sigma(\omega)$ or its susceptibility $\chi(\omega)$ [30]. The most general one is the transfer matrix approach, which can be applied to a very complex and multilayered system and yields the transmission, the reflection and the absorption of the system. For a simpler system consisting of a thin-film sample on a transparent substrate, the Fabry-Perot approach can be used to yield identical results for the transmission of the system, which is often completely sufficient. When the thin-film sample is ultra-subwavelength compared to both the optical and the THz wavelength, the Tinkham formula [31] can be used to yield a very accurate approximation for the transmission of the system. The Tinkham formula is rigorously derived for an infinitely thin film by solving the Maxwell's equations with the proper boundary conditions for the incident and transmitted electromagnetic radiation. The electric field form of the Tinkham formula is given by:

$$\frac{t(\omega)}{t_0(\omega)} = \frac{n_{sub}+n_{air}}{n_{sub}+n_{air}+\eta_0\sigma(\omega)}, \tag{1.2.11}$$

where $t(\omega)$ and $t_0(\omega)$ are the electric fields transmitted through the sample and a reference substrate, respectively, $\sigma(\omega)$ is the complex sheet conductivity of the sample, n_{sub} and n_{air} are the refractive indices of the substrate and the environment, respectively, and η_0 is the impedance of free space.

In the ultrafast time-resolved THz spectroscopy, the ultrafast photoexcitation by the optical pump induces a transient change in the complex conductivity of the studied sample, $\Delta\sigma(\omega,\tau) = \sigma(\omega,\tau) - \sigma(\omega)$, which is probed by the THz probe arriving after a time delay τ. This results in a corresponding transient change in the THz electric field transmitted

through the sample, $\Delta t(\omega,\tau) = t(\omega,\tau) - t(\omega)$. For very small differential changes $\Delta\sigma(\omega,\tau)$ and $\Delta t(\omega,\tau)$, we can apply the Tinkham formula to obtain an approximate relationship between the measured THz transmission and the THz conductivity of the sample. For a truly two-dimensional (2D) sample (for example graphene), where the electron wavefunction is confined in one direction, we have:

$$\Delta\sigma_s(\omega,\tau) \approx -\frac{n_{sub}+n_{air}}{\eta_0} \times \frac{\Delta t(\omega,\tau)}{t(\omega)}. \tag{1.2.12}$$

where $\Delta\sigma_s(\omega,\tau)$ is the photoinduced change in the complex sheet conductivity of the sample, n_{sub} and n_{air} are the THz refractive indices of the substrate and the environment, respectively, and η_0 is the impedance of free space. On the other hand, for a thin-film sample with a finite thickness d (for example semiconductors at the nanoscale), where the electron wavefunction is not truly confined in any direction, we have:

$$\Delta\sigma_b(\omega,\tau) \approx -\frac{n_{sub}+n_{air}}{\eta_0 d} \times \frac{\Delta t(\omega,\tau)}{t(\omega)}, \tag{1.2.13}$$

where $\Delta\sigma_b(\omega,\tau)$ is the photoinduced change in the complex bulk conductivity of the sample.

We note that within the relevant approximations Equations 1.2.12 and 1.2.13 present a direct linear relationship between the differential THz transmission (an experimental quantity that we can measure) to the photoinduced THz conductivity of the sample (a physical quantity that we are interested in). However, the photoinduced THz conductivity is a macroscopic quantity, which is useful from an engineering point of view for the design and development of practical devices, but it cannot by itself explain the microscopic origins of the dynamic THz response of the sample. To answer this question, we need a physical model for the photoinduced THz conductivity (or THz absorption). The final important step is the development of such theoretical model, which describes the true physics of the particular sample or material under study.

Section 1.3 References

[1] G. E. Moore, "Cramming more components onto integrated circuits," *Electronics* **38**, 8 (1965).

[2] H. Boehm et al., "Dunnste Kohlenstof-Folien," *Z. Naturforsch. Pt. B* **17**, 150-153 (1962).

[3] A. Van Bommel et al., "LEED and Auger-electron observations of SiC (0001) surface," *Surf. Sci.* **48**, 463-472 (1975).

[4] N. R. Gall et al., "Two dimensional graphite films on metals and their intercalation," *Int. J. Mod. Phys. B* **11**, 1865-1911 (1997).

[5] K. S. Novoselov et al., "Electric Field Effect in Atomically Thin Carbon Films," *Science* **306**, 666-669 (2004).

[6] K. S. Novoselov et al., "Two-dimensional gas of massless Dirac fermions in graphene," *Nature* **438**, 197-200 (2005).

[7] C. Berger et al., "Ultrathin Epitaxial Graphite: 2D Electron Gas Properties and a Route toward Graphene-based Nanoelectronics," *J. Phys. Chem. B* **108**, 19912-19916 (2004).

[8] C. Berger et al., "Electronic confinement and coherence in patterned epitaxial graphene," *Science* **312**, 1191-1196 (2006).

[9] W. A. de Heer et al., "Large area and structured epitaxial graphene produced by confinement controlled sublimation of silicon carbide," *Proc. Natl. Acad. Sci. U.S.A.* **108**, 16900-16905 (2011).

[10] F. Bonaccorso et al., "Graphene photonics and optoelectronics," *Nat. Photon.* **4**, 611-622 (2010).

[11] K. Kim et al., "A role for graphene in silicon-based semiconductor devices," *Nature* **479**, 338-344 (2011).

[12] K. S. Novoselov et al., "A roadmap for graphene," *Nature* **490**, 192-200 (2012).

[13] M. Law et al., "Semiconductor nanowires and nanotubes," *Annu. Rev. Mater. Res.* **34**, 83-122 (2004).

[14] W. Lu and C. M. Lieber, "Semiconductor nanowires," *J. Phys. D: Appl. Phys.* **39**, 387-406 (2006).

[15] C. M. Lieber, "The Incredible Shrinking Circuit," *Scientific American Reports*, 64-71 (2007).

[16] W. Lu and J. Xiang, "Semiconductor Nanowires: From Next-Generation Electronics to Sustainable Energy," Royal Society of Chemistry, Print ISBN: 978-1-84973-815-6 (2014).

[17] M. C. Beard et al., "Terahertz spectroscopy," *J. Phys. Chem. B* **106**, 7146-7159 (2002).

[18] C. A. Schmuttenmaer, "Exploring dynamics in the far-infrared with terahertz spectroscopy," *Chem. Rev.* **104**, 1759-1779 (2004).

[19] J. B. Baxter and G. W. Guglietta, "Terahertz spectroscopy," *Anal. Chem.* **83**, 4342-4368 (2011).

[20] B. Ferguson and X.-C. Zhang, "Materials for terahertz science and technology," *Nat. Mater.* **1**, 26-33 (2002).

[21] M. Tonouchi, "Cutting-edge terahertz technology," *Nat. Photon.* **1**, 97-105 (2007).

[22] N. Katzenellenbogen and D. Grischkowsky, "Efficient generation of 380 fs pulses of THz radiation by ultrafast laser pulse excitation of a biased metal-semiconductor interface," *Appl. Phys. Lett.* **58** (3), 222-224 (1991).

[23] M. Tani et al., "Emission characteristics of photoconductive antennas based on low-temperature-grown GaAs and semi-insulating GaAs," *Appl. Opt.* **36**, 7853-7859 (1997).

[24] Q. Wu and X. C. Zhang, "Free-space electro-optic sampling of terahertz beams," *Appl. Phys. Lett.* **67** (24), 3523-3525 (1995).

[25] Q. Wu and X. C. Zhang, "Ultrafast electro-optic field sensors," *Appl. Phys. Lett.* **68** (12), 1604-1606 (1996).

[26] A. Nahata et al., "A wideband coherent terahertz spectroscopy system using optical rectification and electro-optic sampling," *Appl. Phys. Lett.* **69** (16), 2321-2323 (1996).

[27] J. T. Kindt and C. A. Schmuttenmaer, "Theory for determination of the low-frequency time-dependent response function in liquids using time-resolved terahertz pulse spectroscopy," *J. Chem. Phys.* **110**, 8589-8596 (1999).

[28] H. Němec et al., "Methodology of an optical pump-terahertz probe experiment: An analytical frequency-domain approach," *J. Chem. Phys.* **117**, 8454- 8466 (2002).

[29] H.-K. Nienhuys and V. Sundström, "Intrinsic complications in the analysis of optical-pump, terahertz probe experiments," *Phys. Rev. B* **71**, 235110 (2005).

[30] R. D. Guenther, "Modern Optics," John Wiley & Sons, ISBN: 0-471-60538-7 (1990).

[31] M. Tinkham, "Energy gap interpretation of experiments on infrared transmission through superconducting films," *Phys. Rev.* **104**, 845-846 (1956).

Chapter 2
Ultrafast THz Response of Graphene

In Chapter 2, we discuss the dynamic THz response and the hot-carrier dynamics of graphene following ultrafast photoexcitation. We look at a wide variety of high quality graphene, including epitaxial and chemical-vapor-deposited (CVD). In Section 2.1, we first introduce graphene, focusing on the studied epitaxial and CVD types of graphene, and its electronic and optical properties. In Section 2.2, we discuss the dynamic THz response of pristine epitaxial and CVD graphene, which is characteristic for a pristine disorder-free graphene layer. In Section 2.3, we discuss the dynamic THz response of multilayer epitaxial graphene, in which interlayer interactions play an important role. In Section 2.4, we discuss the dynamic THz response of buckled epitaxial graphene, in which an energy gap has been carefully engineered. In Section 2.5, we discuss the dynamic THz response of epitaxial graphene nanoribbons, in which quantum confinement effects become prominent. In Section 2.6, we finally present a brief summary of the results in Chapter 2.

Section 2.1 Epitaxial and CVD Graphene

In this section, we introduce graphene and its electronic and optical properties. We focus on the studied epitaxial and CVD types of graphene including synthesis, fabrication and characterization.

Graphene is a monolayer of carbon atoms arranged in a two-dimensional (2D) hexagonal honeycomb lattice. Graphene can be considered to be the 2D member of a larger carbon family consisting of 3D graphite, 1D graphene nanoribbons and carbon nanotubes, and 0D graphene nanodots and fullerenes (also called buckyballs) [1]. Figure 2.1.1(a) and (b) [2] show the physical lattice in real space and the corresponding reciprocal lattice in wavevector space of graphene, respectively. The honeycomb lattice in real space can be decomposed into two equivalent triangular lattices, A and B, with a basis of an A-B pair

of atoms per unit cell. The corresponding reciprocal lattice in wavevector space is also hexagonal with two sets of equivalent points, K and K', which are called Dirac points, at the corners of the graphene Brillouin zone (BZ). This equivalence gives rise to a valley degeneracy of two for the electrons, which is often referred to as pseudo-spin degeneracy. Combined with the real spin degeneracy of two, this gives a total degeneracy of four for the electrons in graphene.

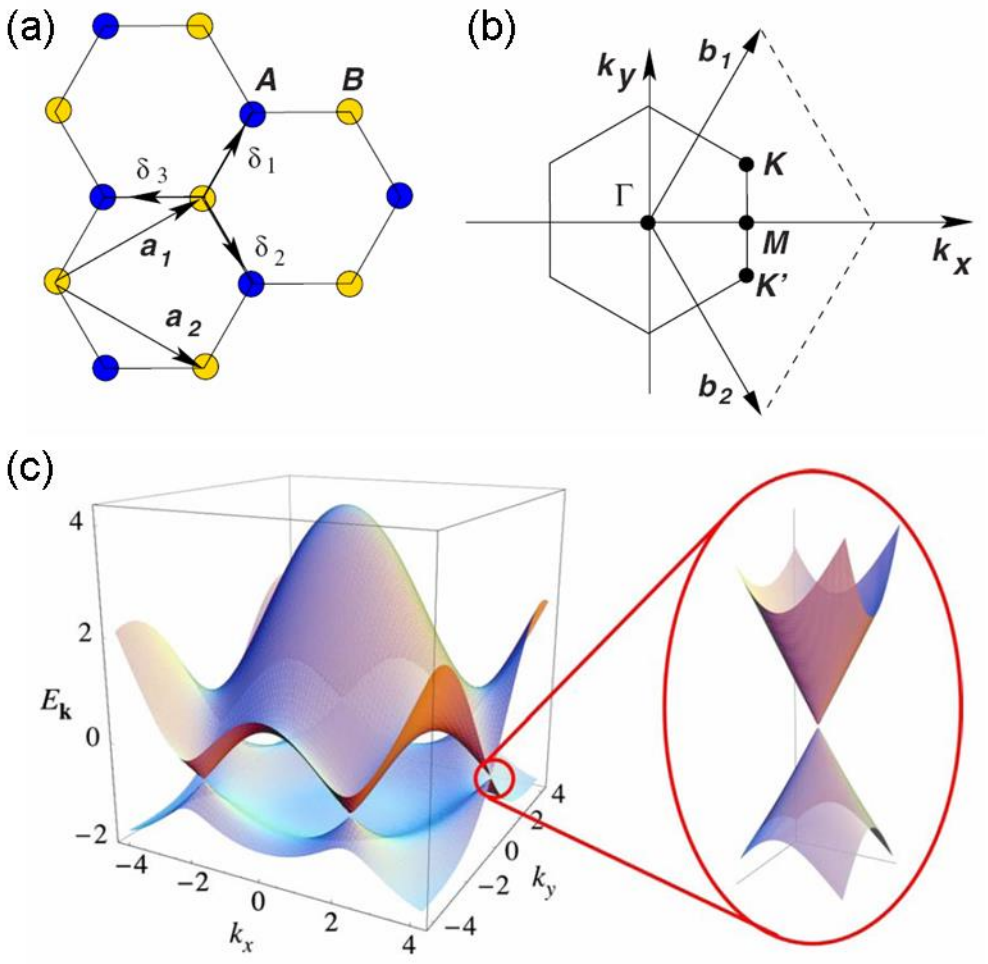

Figure 2.1.1 – (a) Physical lattice in real space and (b) reciprocal lattice in wavevector space of graphene. (c) Energy band structure of graphene. (Adapted from Ref. [2].)

In a conventional tight-binding model calculation [2], which includes both nearest and next-nearest neighbor atoms, the energy band structure has the form:

$$E_{\pm}(\boldsymbol{k}) = \pm t\sqrt{3 + f(\boldsymbol{k})} - t' f(\boldsymbol{k}), \tag{2.1.1}$$

$$f(\boldsymbol{k}) = 2cos\left(\sqrt{3}k_y a\right) + 4cos\left(\frac{\sqrt{3}}{2}k_y a\right)cos\left(\frac{3}{2}k_x a\right), \quad (2.1.2)$$

where the plus and the minus sign applies to the upper (π or conduction) and the lower (π^* or valence) band, respectively, $t \approx 2.8$ eV and t' is the nearest and the next-nearest neighbor hopping energy, respectively, and $a \approx 1.42$ Å is the carbon-carbon distance. The full calculated band structure is shown in Figure 2.1.1(c) [2]. Arguably, the most interesting feature is that the conduction and valences bands touch at the Dirac points and the band structure is linear in the vicinity. The energy dispersion in the vicinity of the Dirac point is approximately given by:

$$E_{\pm}(\boldsymbol{k}) = \pm v_F \boldsymbol{k}, \quad (2.1.3)$$

where $v_F = 3ta/2$ is the Fermi velocity, with a value of $v_F \approx 1 \times 10^6$ m/s. Consequently, the electrons in graphene move at the remarkably high (relativistic) Fermi velocity, which is only ~1/300 of the speed of light in vacuum, c, much like photons move in vacuum. The important implication is that the electron wavefunction in the vicinity of the Dirac point obeys the 2D Dirac equation:

$$-iv_F \boldsymbol{\sigma} \cdot \nabla\psi(\boldsymbol{r}) = E\psi(\boldsymbol{r}). \quad (2.1.4)$$

Hence, the electrons in graphene are also termed Dirac electrons or Dirac fermions. Another interesting consequence of the linear energy dispersion in the vicinity of the Dirac point is that the light absorption of graphene is determined only by the fine structure constant, $\alpha = e^2/\hbar c$, and is completely independent of the light frequency [3]. Despite being only one atom thick, graphene absorbs $\pi\alpha \approx 2.3\%$ of the incident light from the visible to the THz frequency range, where the linear approximation is valid.

To date a number of techniques have been demonstrated for the synthesis of high quality graphene, and the most important include exfoliation, epitaxial and CVD growth methods. Graphene can be obtained from simple repetitive mechanical exfoliation of ultra-pure pyrolytic graphite by using a regular scotch tape until a single graphene layer is isolated [4, 5]. The exfoliation method yields graphene with very high quality, but it is very difficult to scale up and is expected to have mostly research applications. Graphene can be epitaxially grown on both the Si-face and the C-face of single-crystal silicon carbide (SiC)

substrates by thermal decomposition of Si atoms [6, 7, 8]. The C-face epitaxial growth is more important than the Si-face, because it yields graphene stacks with very high quality that consist of from a few up to a hundred layers, referred to as multilayer epitaxial graphene. It is scalable, compatible with the Si technology and is expected to have high-frequency device applications. Graphene can also be synthesized usually on metal foils from gas precursors by using a CVD growth method [9]. The CVD growth method yields graphene with usually lower quality, but it is scalable, versatile and is expected to have low-cost, large-area device applications. These three and other novel techniques are actively and continuously being developed and improved.

In this chapter, we report a comprehensive study of the dynamic THz response of graphene synthesized using three different methods. The first type is multilayer epitaxial graphene (MEG), which is grown on the C-face of single-crystal 4H-SiC($000\bar{1}$) substrates by thermal decomposition of Si atoms [10, 11]. Figure 2.1.2 [12] shows a schematic diagram illustrating the epitaxial growth method. The MEG grows conformally across atomic terraces on the SiC substrate resulting into large continuous layers with domain sizes exceeding hundreds of micrometers in size. The individual layers in MEG are electronically decoupled due to their unique rotational stacking and each layer exhibits a single graphene layer Dirac cone near the Dirac point. Figures 2.1.3 [13], 2.1.4 [14] and 2.1.5 [15] show a representative high-resolution scanning tunneling microscopy (STM) image, a Raman spectroscopy measurement and a high-resolution angle-resolved photoemission spectroscopy (ARPES) measurement, respectively, of MEG. The key conclusion supported by a whole range of characterization techniques is that MEG behaves in essence as multilayer graphene.

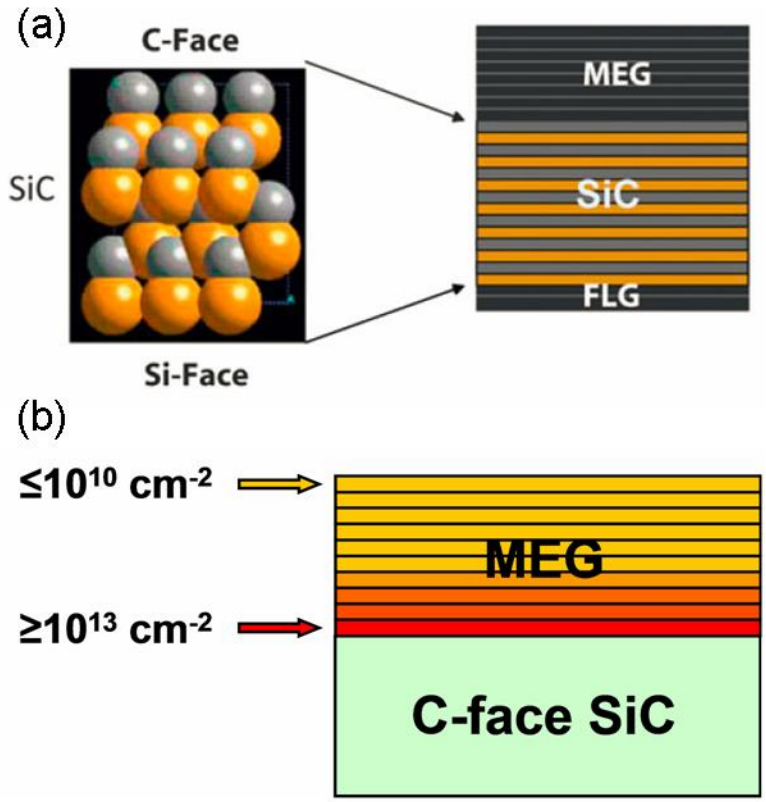

Figure 2.1.2 – Schematic diagram of MEG on SiC. (Adapted from Ref. [12].)

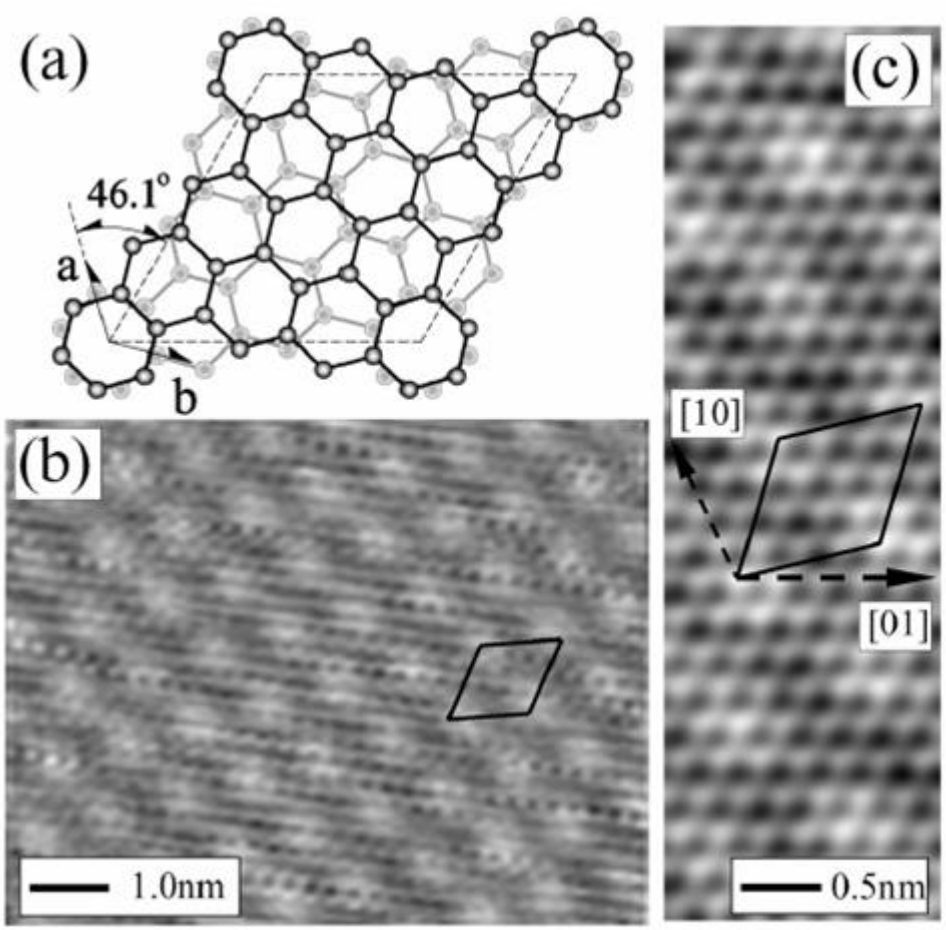

Figure 2.1.3 – High-resolution scanning tunneling microscopy (STM) image of MEG. (Adapted from Ref. [13].)

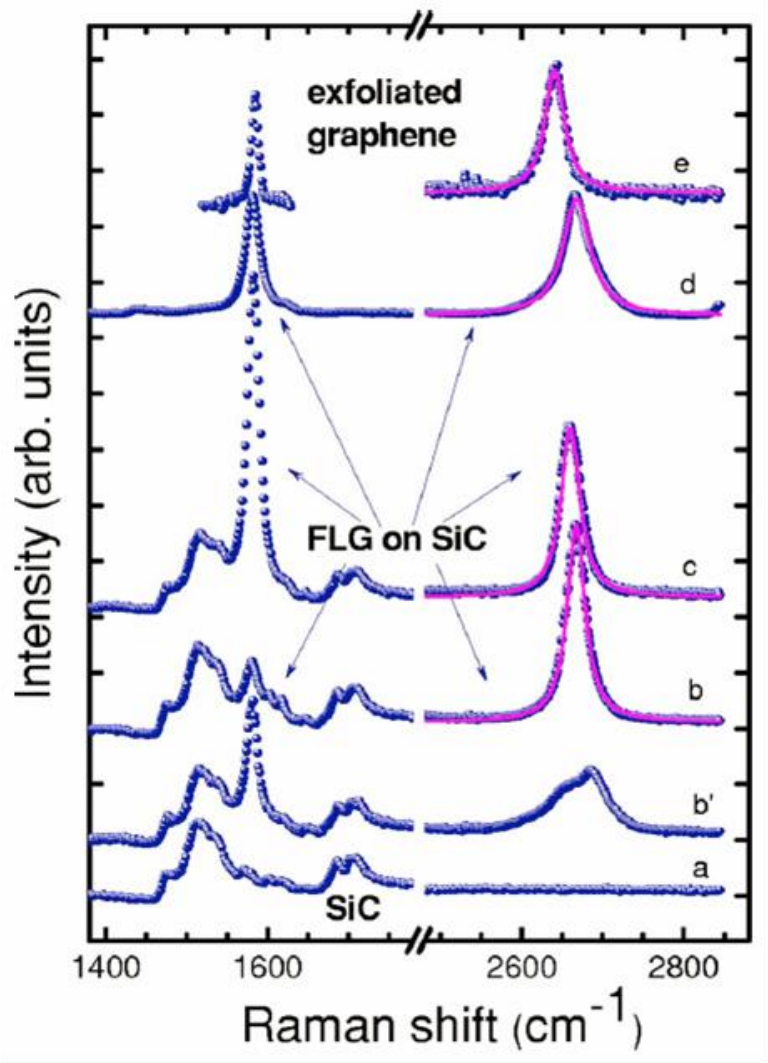

Figure 2.1.4 – Raman spectroscopy measurement of MEG. (Adapted from Ref. [14].)

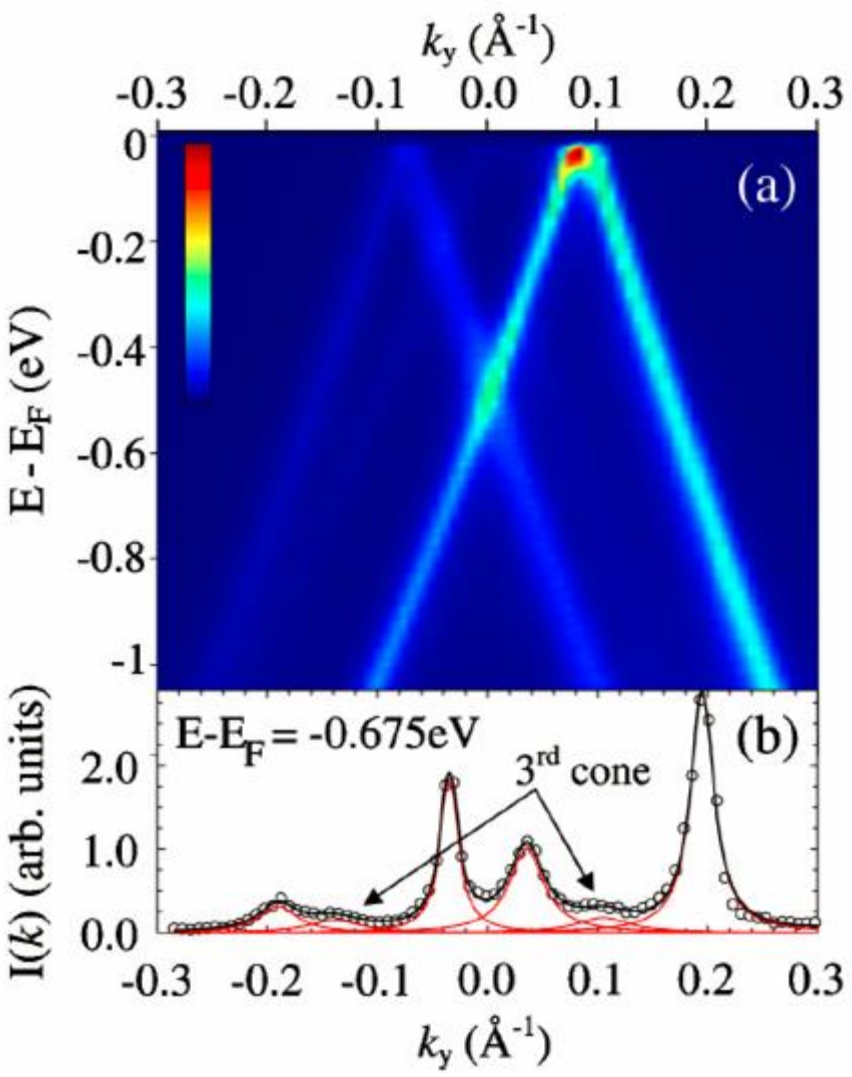

Figure 2.1.5 – High-resolution angle-resolved photoemission spectroscopy (ARPES) measurement of MEG. (Adapted from Ref. [15].)

The second type is single-crystal CVD graphene (sCVDG), which is grown on oxygen-rich copper foil into large individual single crystals exceeding hundreds of micrometers in size [16]. Figure 2.1.6 [16] shows a representative scanning electron microscopy (SEM) image, an optical microscopy (OM) image and a Raman spectroscopy measurement of sCVDG.

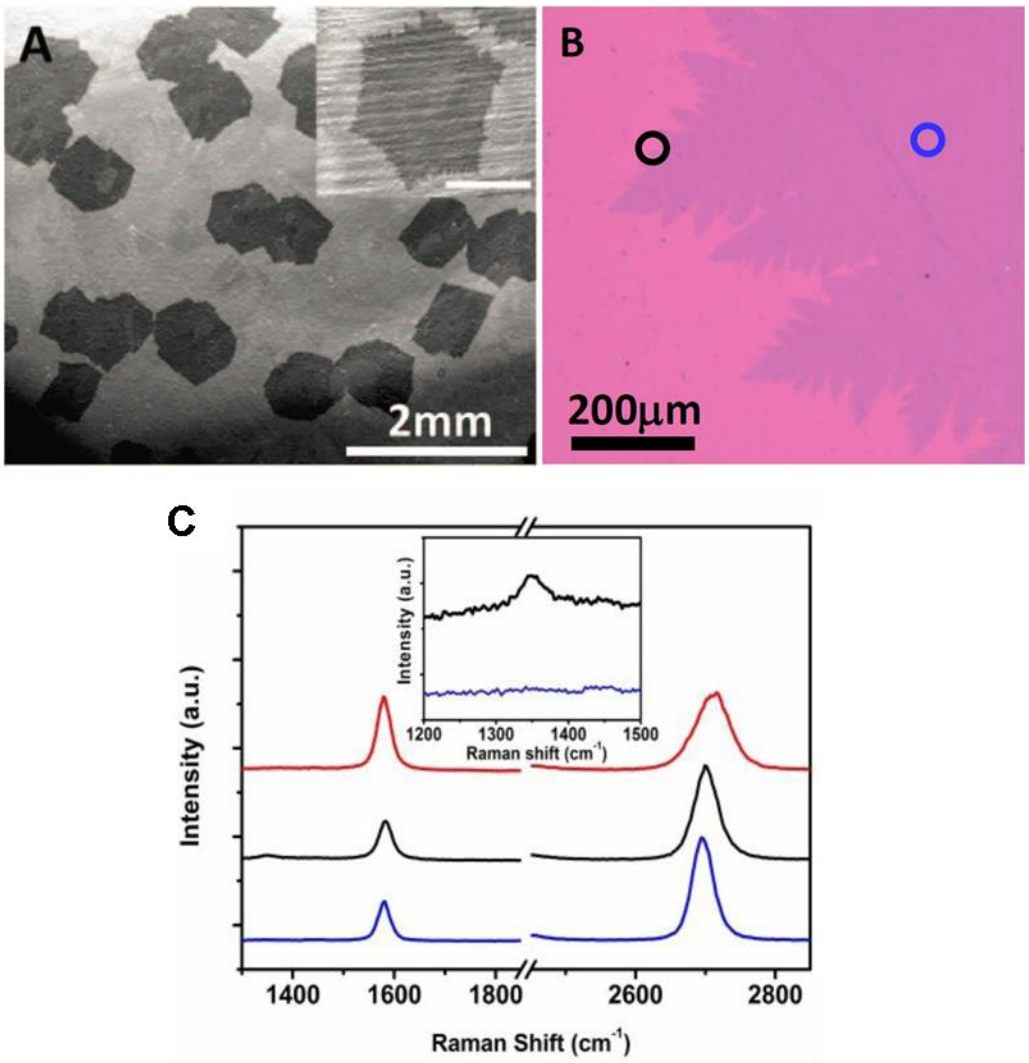

Figure 2.1.6 – (a) Scanning electron microscopy (SEM) image, (b) optical microscopy (OM) image and (c) Raman spectroscopy measurement of sCVDG. (Adapted from Ref. [16].)

The third type is polycrystalline CVD graphene (pCVDG), which is grown on copper foil into large continuous layers with domain sizes on the order of hundreds of nanometers [17]. By carefully tuning the chemical recipe, both mono- and bi-layer pCVDG samples can be reliably grown. Figure 2.1.7 [17] shows a representative photographic image and a Raman spectroscopy measurement of pCVDG.

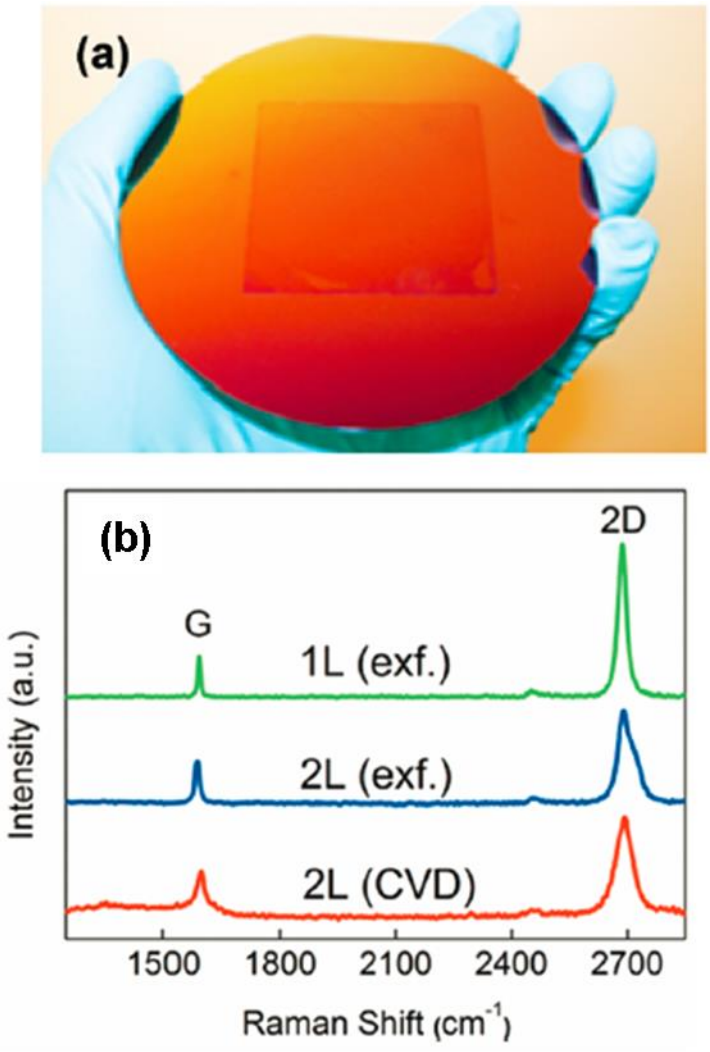

Figure 2.1.7 – (a) Photographic image and (b) Raman spectroscopy measurement of pCVDG. (Adapted from Ref. [17].)

The as-grown CVD graphene samples are later transferred to various substrates including C-cut single-crystal sapphire (Alfa Aesar) and amorphous polyethylene (TOPAS cyclic olefin copolymer, TOPAS Advanced Polymers) for the ultrafast time-resolved THz spectroscopy measurements. Figure 2.1.8 [18] shows a representative ARPES measurement of high quality exfoliated graphene transferred to a SiO_2 substrate. The ARPES results for transferred CVD graphene are expected to be very similar. It is very important to note that the transfer of exfoliated and CVD graphene to an arbitrary substrate introduces a substantial amount of defects, charge impurities, wrinkles and ripples [19, 20, 21]. The introduced imperfections have a strong influence on the carrier transport and dynamics of these graphene samples.

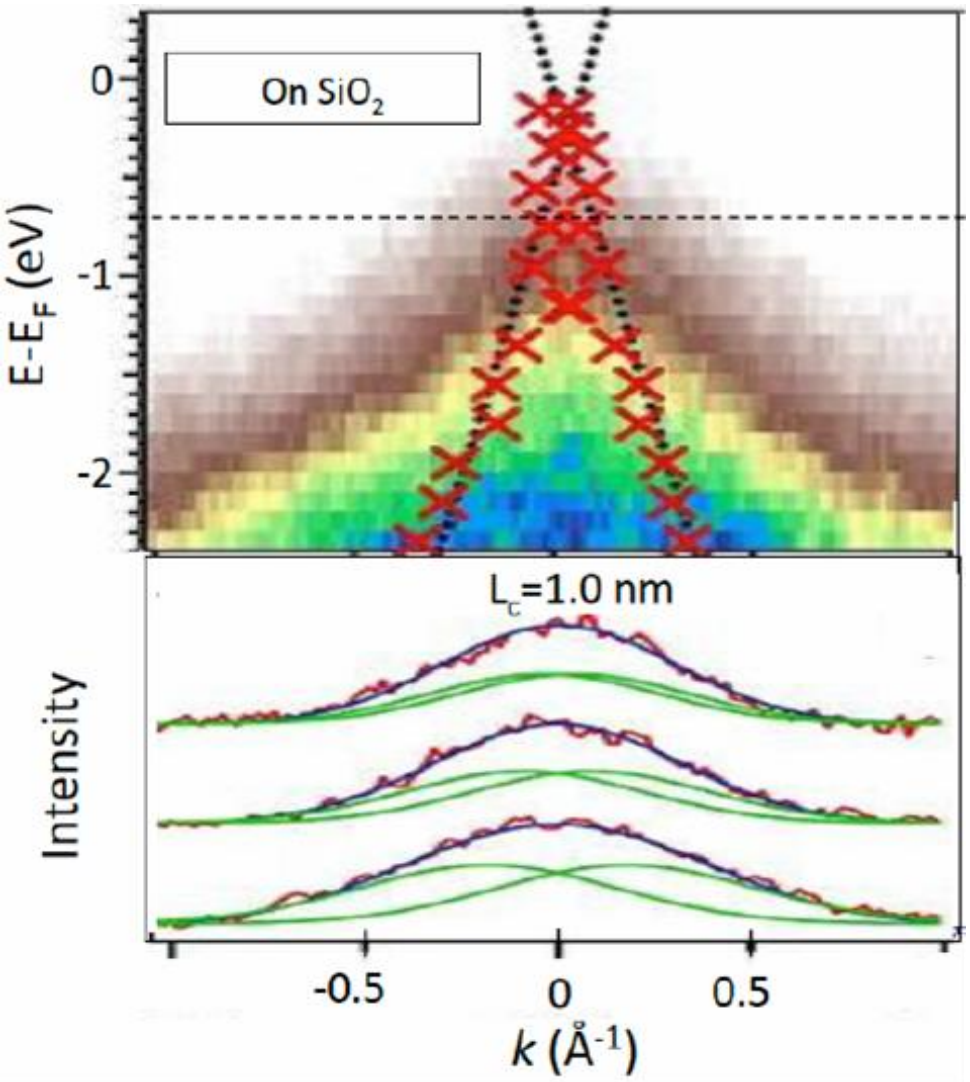

Figure 2.1.8 – High-resolution angle-resolved photoemission spectroscopy (ARPES) measurement of high quality exfoliated graphene transferred to a SiO_2 substrate. (Adapted from Ref. [18].)

Because the different graphene samples are synthesized using completely different techniques, their doping density and degree of disorder are also very different, which allows us to study the dynamic THz response for different Fermi levels and different degrees of disorder. The MEG samples have a gradient doping density profile, where the first few layers closest to the underlying SiC substrate are highly n-doped (Fermi level E_F ~ 100-400 meV) due to electron transfer from the interface, and the Fermi level in subsequent layers decreases exponentially away from the substrate to around E_F ~ 10 meV [10, 11, 22, 23, 24]. The CVDG samples are highly p-doped (Fermi level E_F ~ 200-400 meV) due to water vapor adsorption from the environment [25]. Thus, we can directly

compare the dynamic THz response of graphene with Fermi level far above, far below and very close to the Dirac point.

The graphene degree of disorder is in general not straightforward to quantify, but it can be estimated from various characterization techniques including ARPES, STM, Raman spectroscopy and electronic transport measurements. Raman spectroscopy measurements of all three types of our graphene samples show negligible D peaks suggesting extremely low disorder [14, 16, 17]. The width of the Dirac cone in the graphene band structure, which is directly measured by ARPES, can provide a more sensitive measure for the long range coherence of graphene [18]. Epitaxial graphene exhibits a very sharp, narrow and well defined Dirac cone indicating very smooth and homogenous graphene films with extremely high quality. On the other hand, exfoliated and especially CVD graphene transferred to an arbitrary substrate exhibits a rather smeared and broad Dirac cone indicating wrinkled and non-homogenous graphene films. From the width of the Dirac cone, we can extract a correlation length, which for epitaxial graphene exceeds l_c ~ 50 nm, limited *only* by the instrument resolution, but is expected to be much longer [18]. The correlation length for exfoliated and CVD graphene is l_c ~ 1-3 nm [18]. A similar disparity in the long range coherence is inferred also from electronic transport and magneto-optical spectroscopy measurements of the graphene carrier mobility. The carrier mobility of epitaxial graphene has been reported to exceed μ ~ 250,000 cm^2/(V·s) [10, 11] close to the theoretical value for a pristine disorder-free graphene layer. On the other hand, the carrier mobilities of exfoliated and CVD graphene transferred to an arbitrary substrate range from a few thousands to tens of thousands dominated by interactions with defects, charge impurities, wrinkles and ripples [26, 27]. The highest values of up to μ ~ 200,000 cm^2/(V·s) are achieved by minimizing these extrinsic scattering mechanisms including placing the graphene on ultra-smooth substrates such as hexagonal boron nitride (h-BN) [28] or suspending it [29]. Thus, we can also directly investigate the impact of disorder on the dynamic THz response of graphene.

Section 2.2 Pristine Epitaxial and CVD Graphene

The ultrafast dynamics of hot carriers in graphene are important both for understanding carrier-carrier interactions and carrier-phonon relaxation processes, and for

understanding the physics underlying novel high-speed electronic and optoelectronic devices. Early experimental and theoretical studies of hot-carrier dynamics focused on the visible and near infrared spectral regions [30, 31, 32]. There have recently been a number of experiments investigating the response in the terahertz (THz) region of the spectrum exhibiting a variety of dynamics; these have largely been interpreted in the framework of phenomenological models, and sometimes invoke extrinsic effects such as disorder. In this section, we use ultrafast time-resolved THz spectroscopy to systematically investigate the dynamic THz response and the hot-carrier dynamics in an array of graphene samples having varying amounts of disorder and with either low or high levels of doping. We model the experiments using a microscopic density-matrix theory incorporating all relevant time-dependent carrier-carrier and carrier-phonon scattering mechanisms, and explicitly account for the time-dependent interaction of the carriers with the optical and THz fields. We find that the observed dynamics can be accounted for quantitatively without the need for any extrinsic effects such as disorder, and without any free parameters. The relaxation dynamics are dominated by the combined effect of efficient carrier-carrier scattering, which maintains a thermalized carrier distribution, and carrier-optical-phonon scattering, which removes energy from the carrier liquid. We further demonstrate that the simple Drude model is insufficient to fully account for the THz interactions, that the carrier scattering rate scales linearly with the excess carrier energy, and that the experimental differential THz transmission is an approximate, though not exact, measure of the carrier temperature.

In graphene, a linearly polarized ultrafast optical pulse excitation gives rise to an initially anisotropic distribution of carriers at high energy [33, 34]. Efficient carrier-carrier and carrier-phonon interactions quickly relax the hot carriers into an isotropic thermal distribution, which is then followed by carrier cooling as energy is transferred from the carrier population to the lattice [30, 31, 32]. A variety of dynamical phenomena, such as the appearance of a significant carrier multiplication and transient optical gain, have been theoretically predicted [35, 36, 37, 38] and meanwhile also experimentally demonstrated [37, 39, 40]. The carrier dynamics in the THz region, however, exhibit a number of features that have been interpreted in the framework of phenomenological models, but have not been understood quantitatively as well as qualitatively in terms of fundamental microscopic

theory of many-particle processes. For example, the photoinduced THz conductivity may be either positive or negative. The positive photoinduced THz conductivity has been viewed in the context of simple Drude models as stemming from enhanced free-carrier intraband absorption upon photoexcitation [41, 42], while the negative photoinduced THz conductivity has been attributed variously to stimulated THz emission [43], enhanced carrier scattering with optical phonons, surface optical phonons or charge impurities [44, 45, 46], and carrier heating [47, 48, 49]. In the region close to the Dirac point, hot-carrier relaxation and cooling slow down considerably due to the vanishing density of states, the energetic mismatch with the energy of optical phonons, and the weak scattering with acoustic phonons [31, 50, 51]. Disorder-assisted electron-phonon (supercollision) scattering processes have been recently proposed to account for the experimentally observed cooling times in the THz region [52], but the underlying enhancement of the phase space restrictions should strongly depend on the quality and the degree of disorder of the particular graphene sample. Hence, both a methodical experimental investigation and a microscopic theoretical treatment are markedly needed to provide a rigorous foundation for understanding the THz dynamics of hot carriers in graphene.

In this section, we present the results of a coordinated experimental and theoretical program, using ultrafast time-resolved THz spectroscopy combined with microscopic modeling [53] to systematically study the THz carrier dynamics in a wide variety of graphene samples, including epitaxial and chemical-vapor-deposited (CVD) graphene. We experimentally vary the type of graphene and the degree of disorder, the Fermi level, the number of graphene layers and their stacking orientation, the substrate temperature, the initial carrier temperature, and the type of underlying substrate to determine the dominant mechanisms responsible for the hot-carrier relaxation and cooling dynamics for different graphene material parameters and under different experimental conditions. We also develop a comprehensive understanding of the intricate interplay between these processes by placing them on a solid and common theoretical foundation. The theory is based on the density matrix formalism providing microscopic access to the time- and momentum-resolved dynamics of the carrier occupation, the phonon population for different optical and acoustic modes, and the microscopic polarization determining the optical excitation of a disorder-free graphene system. Critically, the theory calculates explicitly the time-

dependent response of the system to the THz probe pulse; as described below, the macroscopic intraband current density induced by the THz probe, and hence the resulting dynamic THz response, is calculated by fully accounting microscopically for the time-dependent carrier-carrier and carrier-phonon interactions. This approach allows for a direct one-to-one comparison between theory and the measured ultrafast time-resolved THz signal and spectra. Our first-principles microscopic approach explains completely all experimental results without the need for any fitting parameters, phenomenological models or extrinsic effects. We shall see that this allows us to go beyond idealized Drude models for the THz response, and determine the limitations of such models. Specifically, we establish that the hot-carrier dynamics are governed by the coupling of extraordinarily efficient carrier-carrier and carrier-phonon interactions; this is in contrast to electronic transport, which in some graphene samples is dominated by interactions with defects, charge impurities, wrinkles and ripples (i.e. extrinsic effects) since carriers move at the Fermi energy.

A schematic illustration of the hot-carrier dynamics in graphene following ultrafast photoexcitation appears in Figure 2.2.1, which shows how they depend critically on the Fermi level. It is important to distinguish between carrier thermalization via carrier-carrier scattering, which only redistributes the deposited energy within the electron gas, and carrier cooling via carrier-phonon scattering, which takes energy from the electron gas into the phonon system (i.e. the lattice). Figure 2.2.1(a) and (b) show the hot-carrier relaxation and cooling dynamics in highly doped graphene. Initially, the ultrafast optical pump pulse injects high-energy non-equilibrium electrons in the conduction band and holes in the valence band. The strong intraband and interband carrier-carrier scattering processes lead to ultrafast carrier relaxation and thermalization which establish a single uniform hot-carrier Fermi-Dirac distribution within ~100-200 fs after photoexcitation [54]. At that point, carrier generation (through impact ionization) and carrier relaxation (through Auger recombination and intraband carrier-carrier scattering) processes just balance each other, while hot carriers cool via optical and acoustic phonon emission. The hot-carrier cooling is facilitated by these extraordinarily efficient Coulomb interactions by continuously rethermalizing the hot-carrier distribution and replenishing the carriers at high energies. The situation in undoped (very lightly doped) graphene is very different, as shown in Figure

2.2.1(c). Immediately after photoexcitation, the phase space for impact ionization processes is large, while Auger recombination processes are inhibited, which leads to a significant carrier multiplication in the conduction band up to a moderate excitation regime [35, 40]. Again, the strong intraband and interband carrier-carrier scattering processes establish a single uniform hot-carrier Fermi-Dirac distribution on an ultrafast timescale followed by hot-carrier cooling via optical and acoustic phonon emission. At later times, the small phase space near the Dirac point strongly reduces the efficiency of carrier rethermalization via the Coulomb interactions, which slows down phonon emission and hot-carrier cooling.

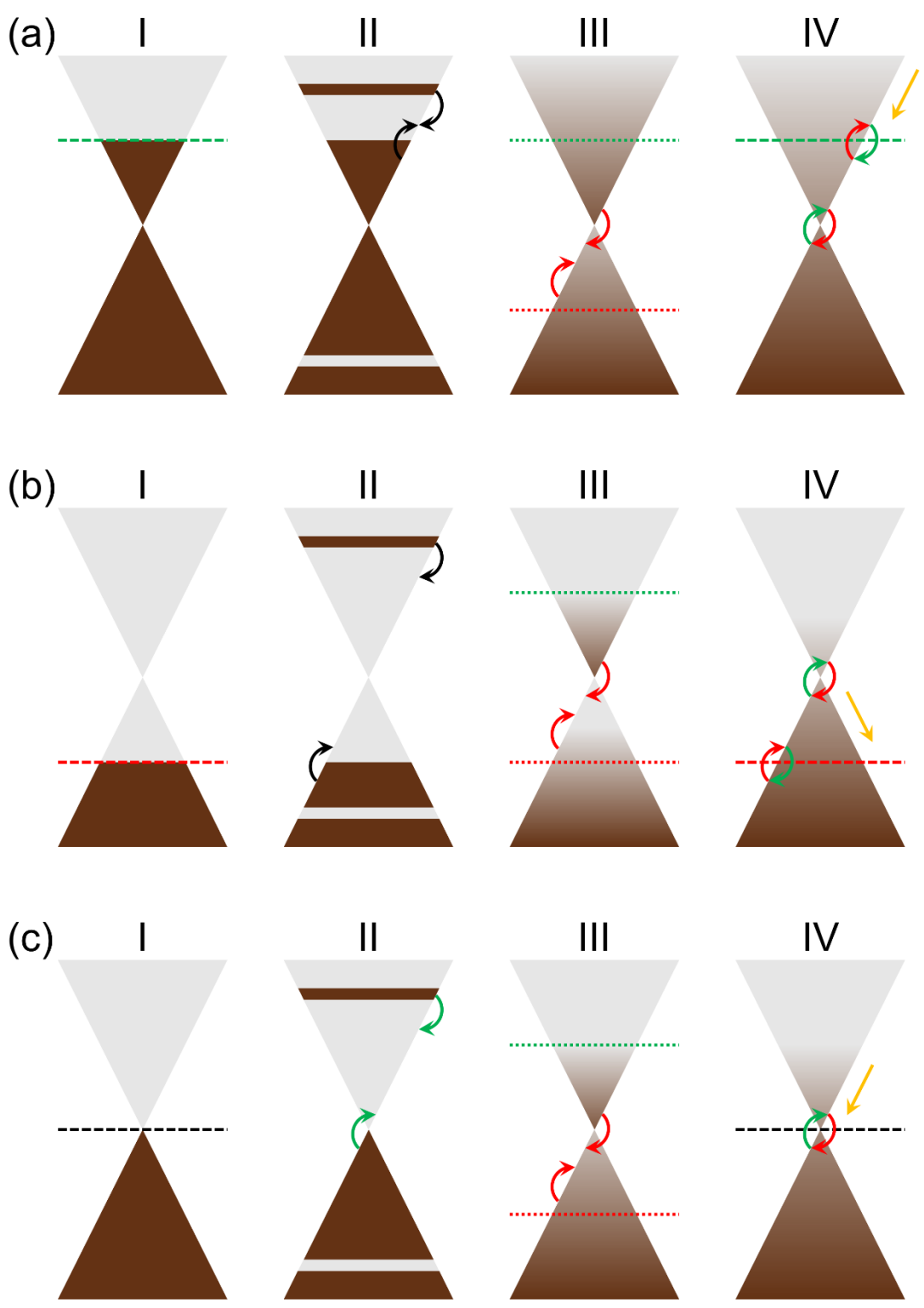

Figure 2.2.1 – Hot-carrier relaxation and cooling dynamics following ultrafast photoexcitation in (a) highly n-doped, (b) highly p-doped and (c) undoped graphene.

The hot-carrier relaxation processes illustrated in Figure 2.2.1 are directly accessible via the dynamic response of a THz probe pulse. Qualitatively, for both epitaxial and CVD graphene having high doping density, we observe in both experiment and theory a fast and substrate-temperature-independent THz carrier dynamics. On the other hand, for graphene having very low doping density, we observe a comparatively slower and strongly substrate-temperature-dependent THz carrier dynamics. A second feature of our experiments is that we find that graphene samples with very different degrees of disorder show essentially the same hot-carrier relaxation times; this suggests that disorder-assisted electron-phonon (supercollision) scattering processes might not play a crucial role in the hot-carrier dynamics as has been proposed in previous literature [52, 55, 56]. We shall show that the dependence of the dynamic THz response on Fermi level, substrate temperature and initial carrier temperature, and its independence of disorder, can be quantitatively understood in the microscopic theory.

Section 2.2.1 Dynamic THz Response

In this section, we discuss the dynamic THz response of pristine epitaxial and CVD graphene, which is characteristic for a pristine disorder-free graphene layer.

Using the ultrafast time-resolved THz spectroscopy technique, we measure the full time-domain differential change in the THz probe pulse transmission through the graphene samples due to photoexcitation by the optical pump pulse, which we then normalize to the THz transmission in the absence of photoexcitation, $\Delta t/t$. To gain physical insight we vary a large set of parameters including the pump fluence, the substrate temperature and the pump-probe delay for each graphene sample. We present experimental data for one graphene sample, which is representative in most of its features for all pristine epitaxial and CVD graphene samples.

Figure 2.2.2(a) shows the full time-domain direct THz transmission through a multilayer epitaxial graphene (MEG) sample with ~63 layers recorded both without photoexcitation by the optical pump and with photoexcitation for a few different THz probe delays after the optical pump. We observe that for this specific MEG sample the THz transmission decreases and hence the THz absorption increases upon photoexcitation. For other graphene samples, we measure the opposite change. We explain the physical origins

of the positive and negative change in the THz transmission (or the THz absorption) in detail later in the section. However, we note that in both cases the temporal shape of the THz probe is completely undistorted, because the graphene films are ultra-subwavelength compared to the THz wavelength (λ/Nc on the order of ~10^4-10^6 depending on the number of layers N in the graphene film, where we use the nominal layer-to-layer separation in graphite $c \approx 3.35$ Å). Experimentally, we directly record with higher signal-to-noise ratio (SNR) the full time-domain differential change in the THz transmission through the graphene samples due to photoexcitation as shown in Figure 2.2.2(b).

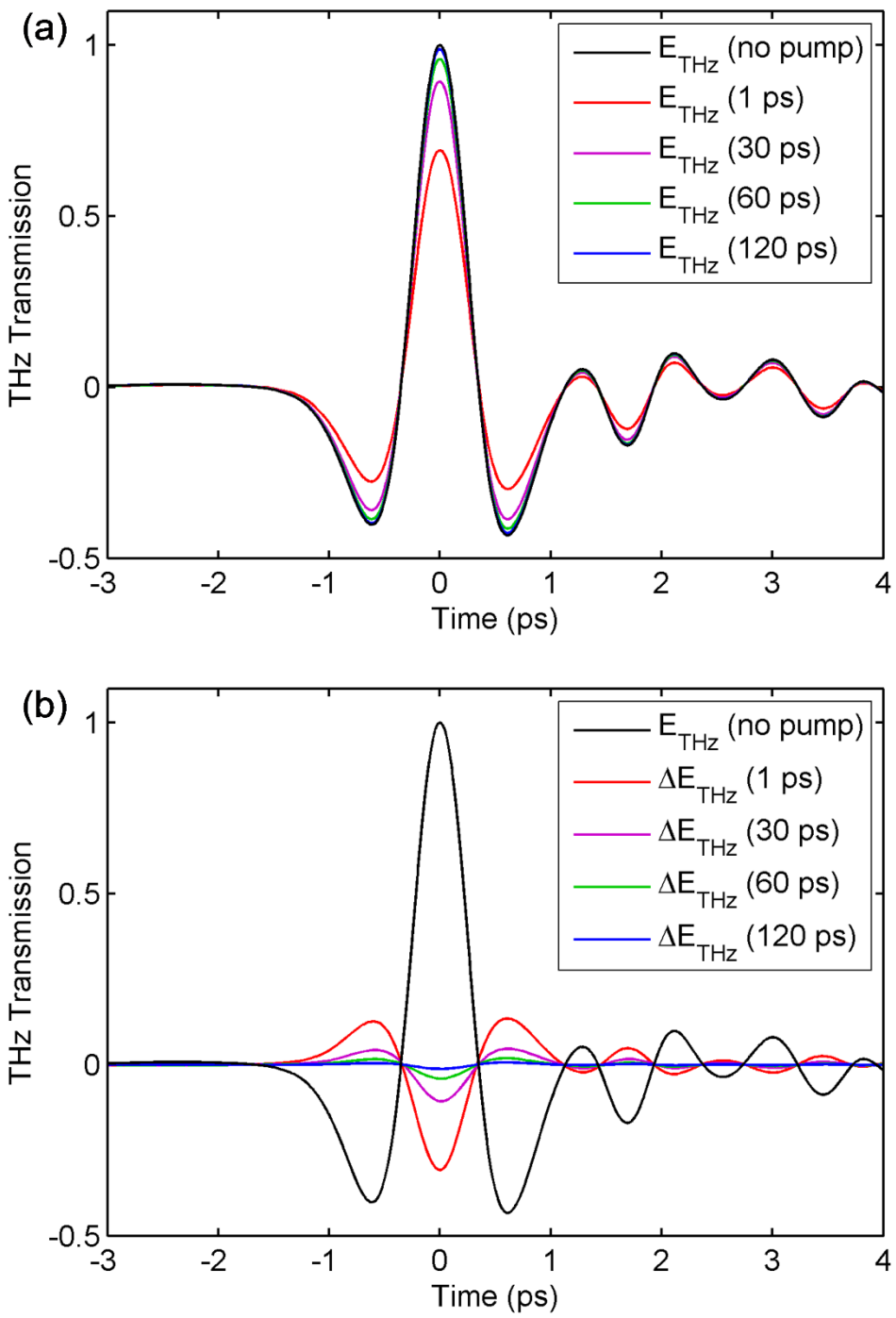

Figure 2.2.2 – (a) Direct and (b) differential THz transmission waveform for variable pump-probe delay for an MEG sample with ~63 layers.

From the measured time-domain differential THz electric field, $\Delta t/t$, we can obtain the frequency-domain differential THz spectrum, $\Delta t(\omega)/t(\omega)$, by straightforward numerical Fourier transformation. Figure 2.2.3(a), (b) and (c) show the differential THz

transmission spectra normalized to the THz transmission without photoexcitation, $\Delta t(\omega)/t(\omega)$, for variable pump-probe delay, variable substrate temperature and variable pump fluence, respectively, for the same MEG sample with ~63 layers. Then, using purely electromagnetic analysis, by solving the Maxwell's equations with the proper boundary conditions for the incident and transmitted THz radiation, this experimental quantity can be related through the Tinkham formula [57] to the photoinduced change in the complex sheet conductivity of graphene, $\Delta\sigma(\omega)$, via:

$$\Delta\sigma(\omega) \approx -\frac{n_{sub}+n_{air}}{\eta_0} \times \frac{\Delta t(\omega)}{t(\omega)}, \tag{2.2.1}$$

where n_{sub} and n_{air} are the THz refractive indices of the substrate and the environment, respectively, and η_0 is the impedance of free space. We note that the THz conductivity of MEG is a summation of the THz conductivities of the individual epitaxial graphene layers in the MEG stack, because the layers are electronically decoupled.

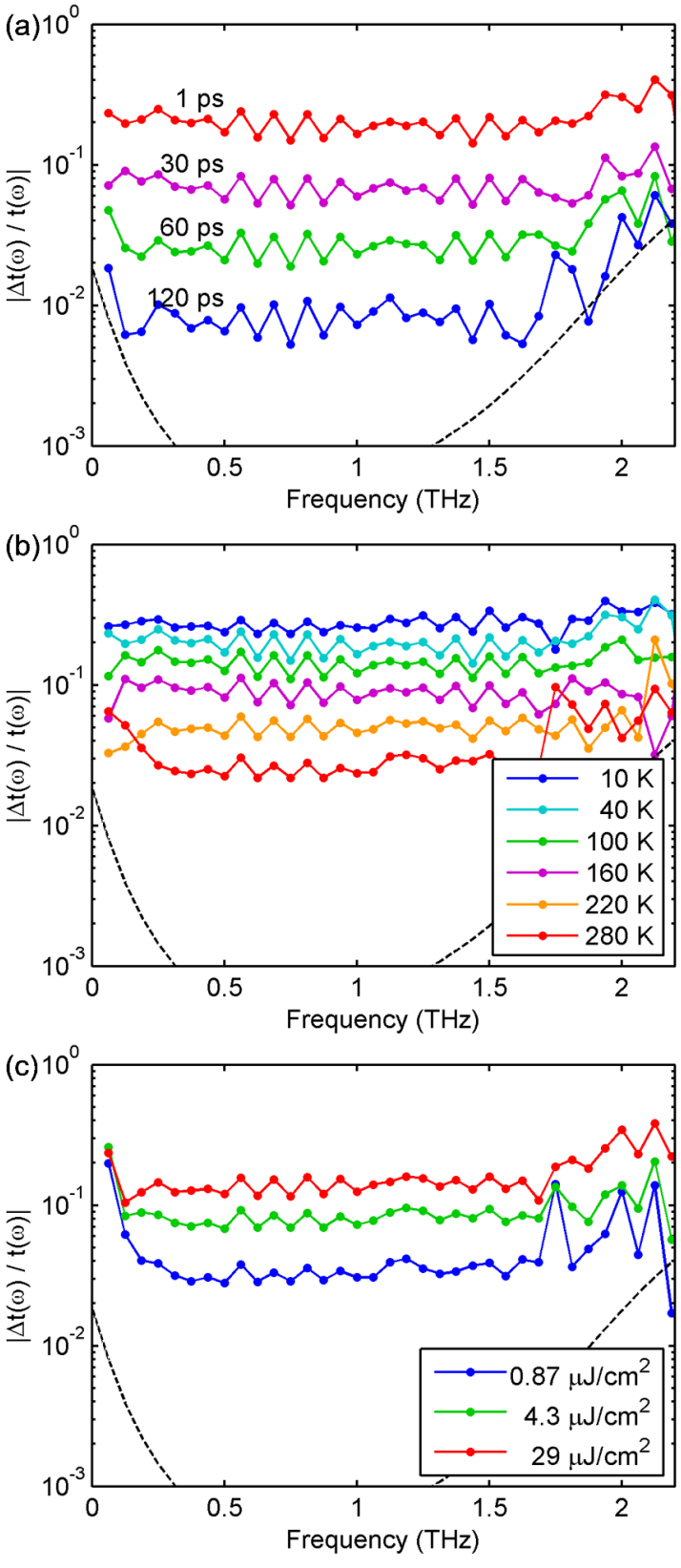
(a)
1 ps
30 ps
60 ps
120 ps
|Δt(ω) / t(ω)|
Frequency (THz)
(b)
10 K
40 K
100 K
160 K
220 K
280 K
|Δt(ω) / t(ω)|
Frequency (THz)
(c)
0.87 μJ/cm2
4.3 μJ/cm2
29 μJ/cm2
|Δt(ω) / t(ω)|
Frequency (THz)

Figure 2.2.3 – Absolute value of differential THz transmission spectrum for (a) variable pump-probe delay, (b) variable substrate temperature and (c) variable pump fluence for an MEG sample with ~63 layers.

Thus, we can directly relate the differential THz transmission (an experimental quantity that we can measure) to the photoinduced THz conductivity of graphene (a physical quantity that we are interested in). However, the photoinduced THz conductivity is a macroscopic quantity, which is useful from an engineering point of view for the design and development of practical graphene-based devices, but it cannot by itself explain the microscopic origins of the dynamic THz response of graphene. To answer this question, we need a physical model for the photoinduced THz conductivity (or THz absorption), which we discuss in detail later in the section. However, we note that the normalized differential THz transmission spectra are remarkably dispersionless in the detectable frequency range under all experimental conditions and for all pristine epitaxial and CVD graphene samples. This dynamic THz response is qualitatively consistent with the simple Drude model and is characteristic for a pristine disorder-free graphene layer. This justifies the application of a simpler data acquisition scheme in which we record the normalized differential THz transmission only at the peak of the THz probe pulse as a function of pump-probe delay to map out the relaxation dynamics of the photoexcited carriers. By doing so, we lose the frequency information, but we gain experimental convenience and enhance the SNR of the measurements.

Section 2.2.2 THz Carrier Dynamics

In this section, we discuss the THz carrier dynamics of pristine epitaxial and CVD graphene, which is characteristic for a pristine disorder-free graphene layer.

First, we consider epitaxial and CVD graphene with high doping density. Figure 2.2.4(a) and (b) show representative differential THz transmission signals at the peak of the THz probe pulse normalized to the THz transmission without photoexcitation, $\Delta t/t$, as a function of pump-probe delay, for variable pump fluence (corresponding to different pump-induced initial carrier temperature) and for variable substrate temperature, respectively, for an MEG sample with ~3 layers. The secondary peak in the differential THz transmission at ~7 ps is due to a round-trip reflection of the optical pump pulse inside the substrate that photoexcites additional carriers. Similar results are obtained for the other

two types of our graphene samples. Based on extensive measurements on many graphene samples under various experimental conditions, we find that the THz carrier dynamics of all graphene samples with high doping are strikingly similar. The differential THz transmission is positive under all experimental conditions, which corresponds to a pump-induced increase of the THz transmission or a decrease of the THz absorption. This observation has been previously phenomenologically attributed to an increase of the carrier scattering rate and a corresponding decrease of the THz conductivity of graphene as the carrier temperature is raised upon photoexcitation, which is essentially a metal-like behavior [44, 45, 46]. In addition, the THz carrier dynamics are weakly dependent on the pump fluence and completely independent of the substrate temperature.

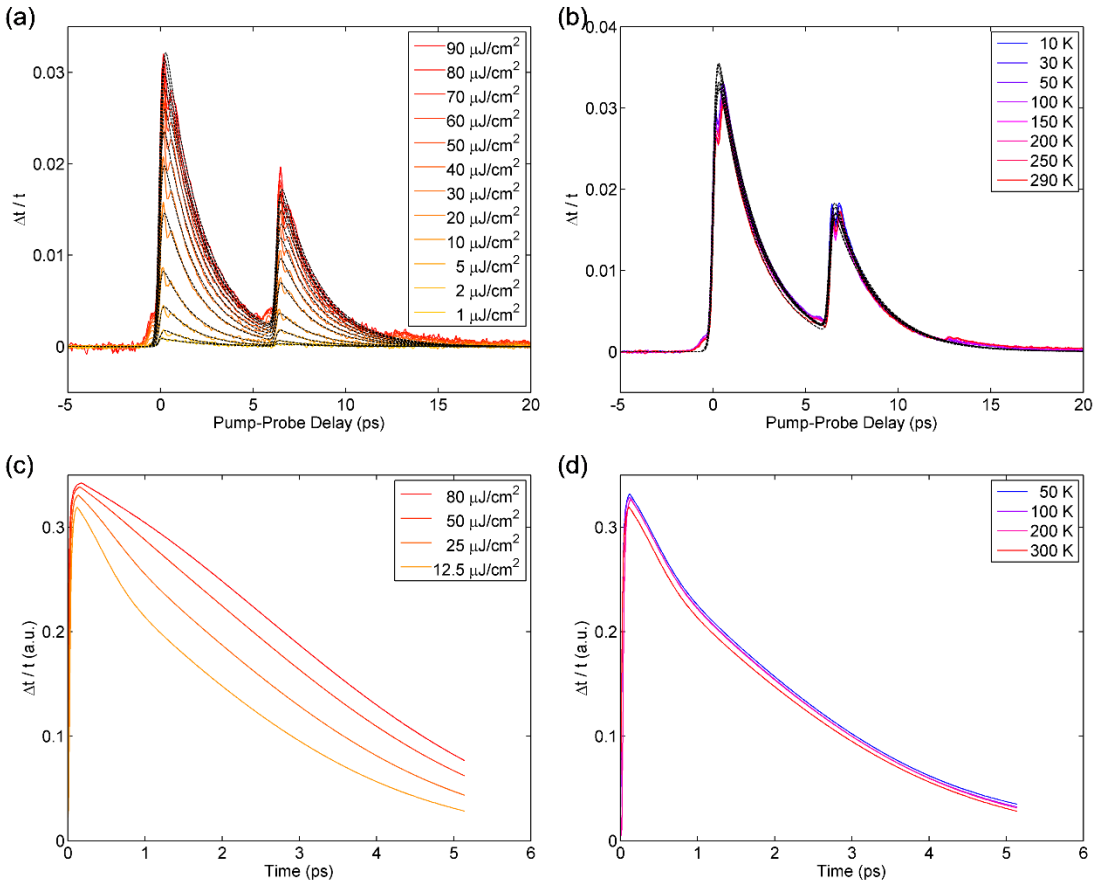

Figure 2.2.4 – Experimental differential THz transmission (a) at a substrate temperature of 300 K for a few different pump fluences and (b) at a pump fluence of 60.0 μJ/cm^2 for a few different substrate temperatures for a highly doped MEG sample with ~3 layers. Theoretical differential THz transmission (c) at a substrate temperature of 300 K for a few different pump fluences and (d) at a pump fluence of 12.5 μJ/cm^2 for a few different substrate temperatures for disorder-free highly doped graphene.

We perform phenomenological fits to the data in Figure 2.2.4(a) and (b) and we discover that the differential THz transmission follows closely a mono-exponential relaxation form under all experimental conditions. A summary of the extracted carrier relaxation times as a function of pump fluence and substrate temperature, respectively, for all graphene samples with high doping is presented in Figure 2.2.5(a) and (b). We note that the relaxation times of all graphene samples with high doping are weakly dependent on the pump fluence and completely independent of the substrate temperature. In addition, they are very similar in magnitude and in the range of ~1-2 ps with sample-to-sample variation within ~20-30%. On average, MEG samples exhibit slightly longer relaxation times than sCVDG and pCVDG samples, which can be attributed to a degree of disorder arising from charge impurities, substrate roughness, wrinkling and breaking of the transferred CVDG samples that can provide additional parallel channels for carrier cooling [52, 55, 56]. We note, however, that the relaxation times of some CVDG samples can approach or exceed these of MEG samples, indicating that disorder-assisted electron-phonon (supercollision) cooling is not the dominant cooling mechanism in our high quality graphene samples, but generally provides at most only a modest correction.

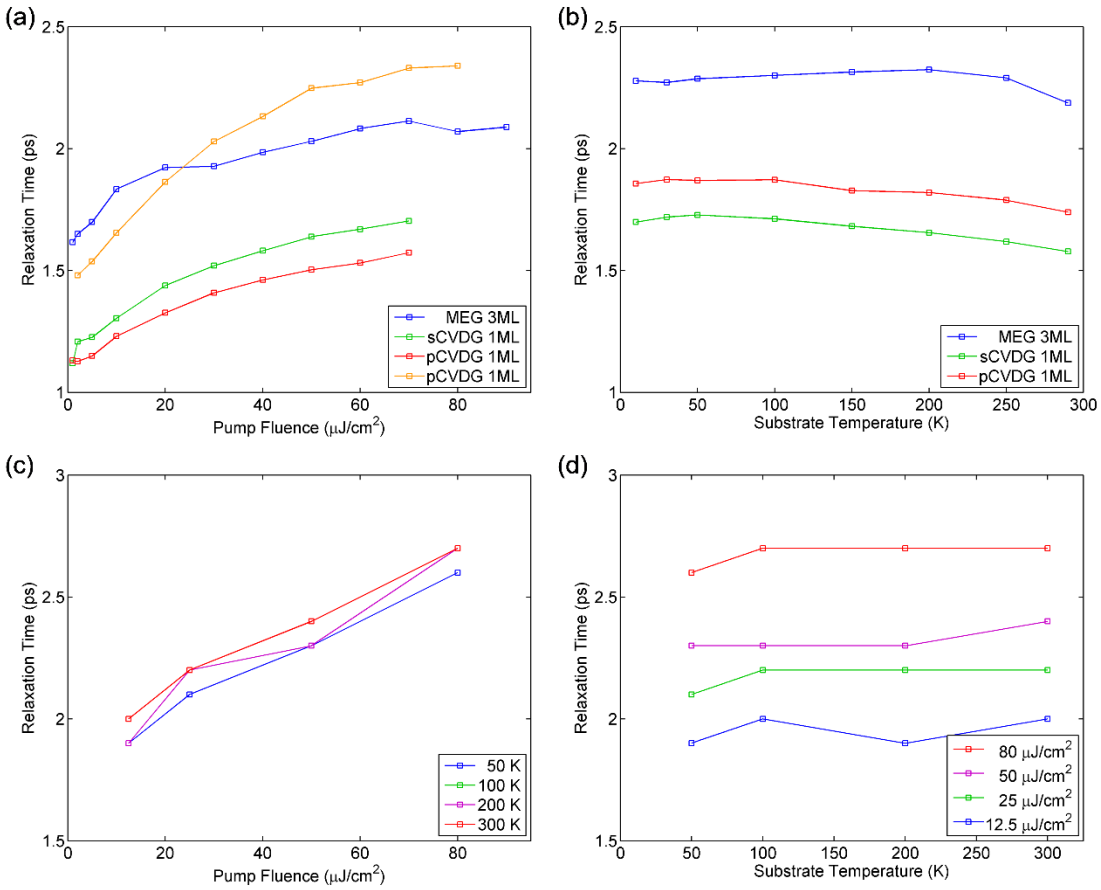

Figure 2.2.5 – Experimental carrier relaxation times as a function of (a) pump fluence at a substrate temperature of 300 K and (b) substrate temperature at a pump fluence of 60.0 μJ/cm^2 for highly doped MEG, sCVDG and pCVDG samples. Theoretical carrier relaxation times as a function of (c) pump fluence for a few different substrate temperatures and (d) substrate temperature for a few different pump fluences for disorder-free highly doped graphene.

Figure 2.2.4(c) and (d) show the THz carrier dynamics calculated within the microscopic theory for disorder-free highly doped graphene ($|E_F|$ = 300 meV) under similar experimental conditions. We observe that the theoretical results reproduce all trends observed in the experiments. The hot-carrier dynamics are a result of the interplay between very efficient carrier-carrier scattering and carrier-optical-phonon scattering. The physical reason for the negligible substrate temperature dependence of the differential THz transmission is that the direct THz absorption itself is insensitive to the substrate temperature for highly doped graphene at least up to room temperature. Similarly, Figure 2.2.5(c) and (d) show the calculated carrier relaxation times to directly compare with the experiments. We note that the slight increase of the relaxation times with the pump fluence

is due to the re-absorption of hot optical phonons generated during the initial carrier thermalization.

To further illustrate the excellent agreement between the experimental data and the theoretical calculations, we compare the maximum absolute values of the THz carrier dynamics of all types of graphene samples with high doping density. Figure 2.2.6(a) and (b) show the maximum absolute value of the differential THz transmission at the peak of the THz probe pulse, $max\{|\Delta t/t|\}$, as a function of pump fluence and substrate temperature, respectively, for MEG, sCVDG and pCVDG samples with high doping, while Figure 2.2.6(c) and (d) show the results obtained within the microscopic theory for disorder-free highly doped graphene ($|E_F|$ = 300 meV) under similar experimental conditions. We observe that the theory captures very well the saturation of the $max\{|\Delta t/t|\}$ signal with the pump fluence and its invariance with the substrate temperature for highly doped graphene samples.

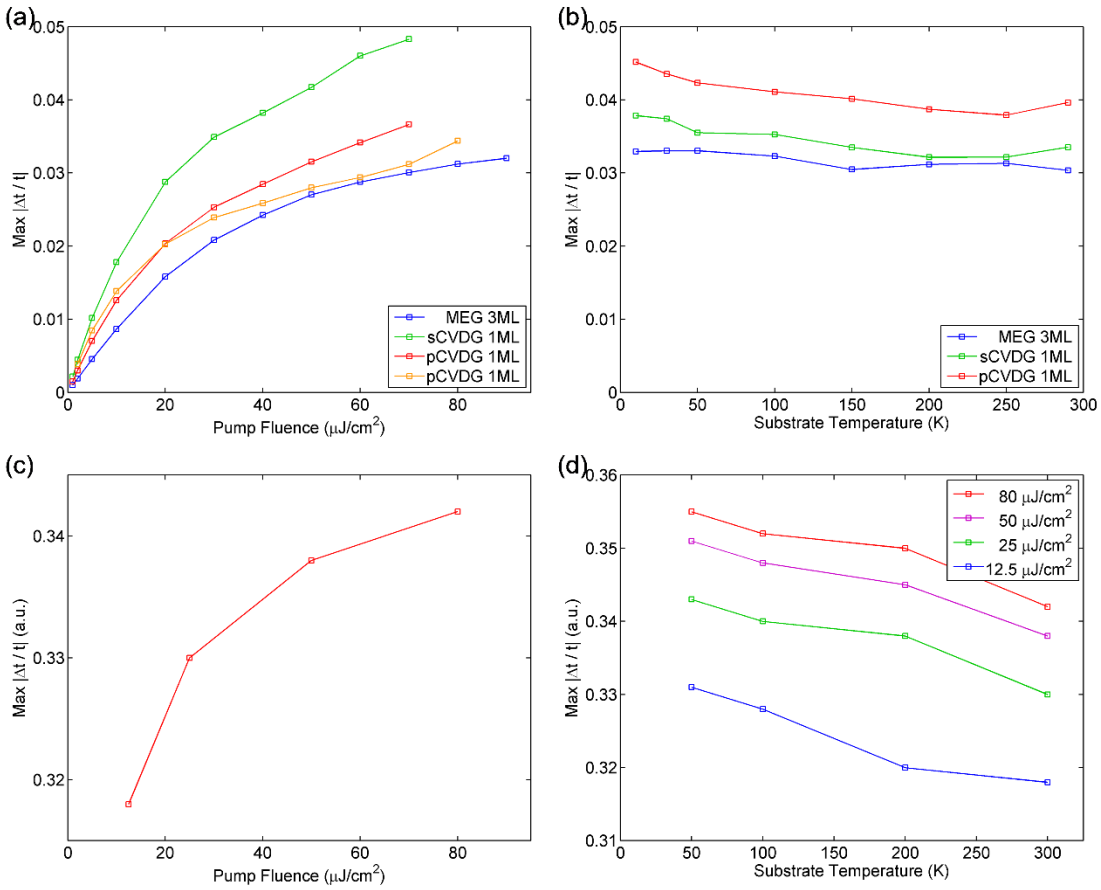

Figure 2.2.6 – Maximum absolute value of experimental differential THz transmission as a function of (a) pump fluence at a substrate temperature of 300 K and (b) substrate temperature at a pump fluence of 60.0 μJ/cm^2 for highly doped MEG, sCVDG and pCVDG samples. Maximum absolute value of theoretical differential THz transmission as a function of (c) pump fluence at a substrate temperature of 300 K and (d) substrate temperature for a few different pump fluences for disorder-free highly doped graphene.

Next, we consider MEG, in which only the first few layers closest to the underlying SiC substrate have high doping density and the large number of top layers have very low doping density. In these MEG samples, the many top layers with low doping completely dominate the measured THz carrier dynamics. Figure 2.2.7(a) and (b) show representative normalized differential THz transmission at the peak of the THz probe pulse, $\Delta t/t$, as a function of pump-probe delay, for variable pump fluence (corresponding to different initial carrier temperature) and for variable substrate temperature, respectively, for an MEG sample with ~63 layers. The secondary dip in the differential THz transmission at ~7 ps is again due to a round-trip reflection of the optical pump pulse inside the substrate that photoexcites additional carriers. In sharp contrast to the high doping case, the differential THz transmission is negative under all experimental conditions, which corresponds to a

pump-induced decrease of the THz transmission or an increase of the THz absorption. This observation can be phenomenologically attributed to an increase of the THz conductivity of graphene as the carrier occupation in the conduction band increases upon photoexcitation, which resembles a semiconductor-like behavior [41, 42]. In addition, the THz carrier dynamics are weakly dependent on the pump fluence, but strongly dependent on the substrate temperature, in contrast to the high doping case.

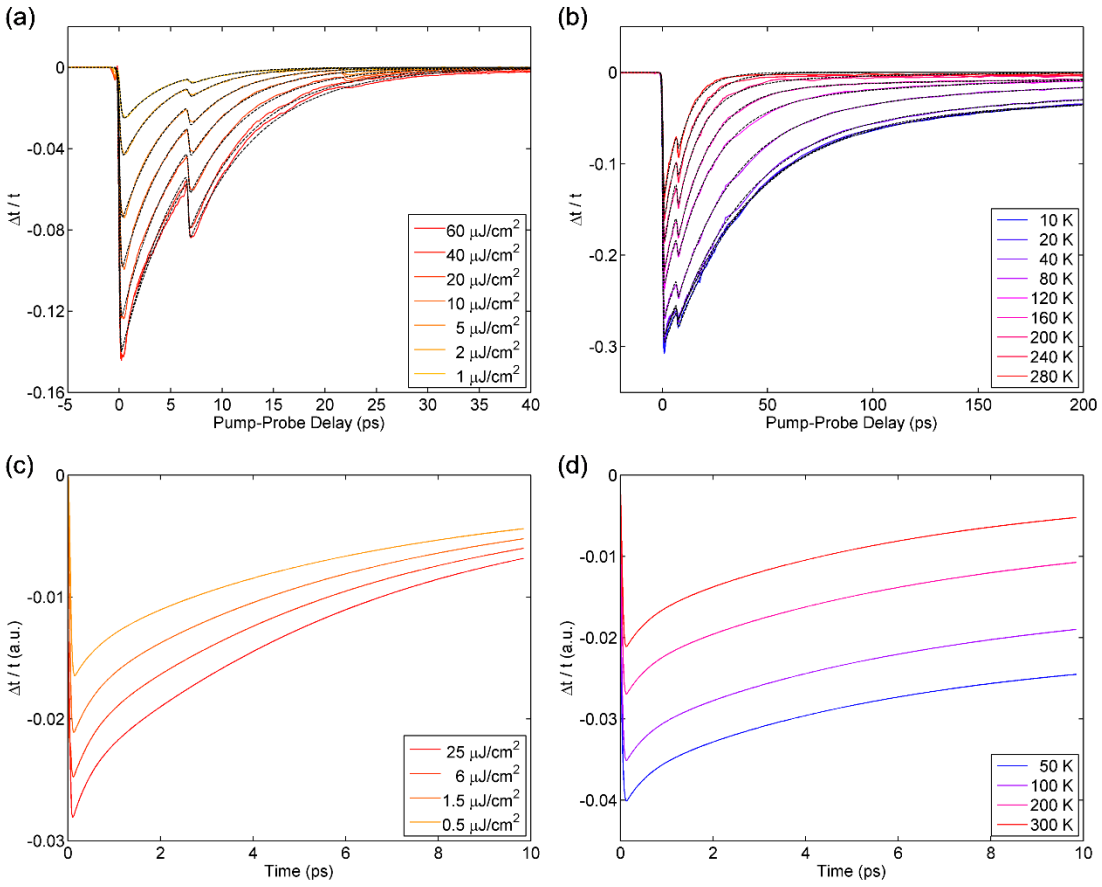

Figure 2.2.7 – Experimental differential THz transmission (a) at a substrate temperature of 300 K for a few different pump fluences and (b) at a pump fluence of 23.4 μJ/cm^2 for a few different substrate temperatures for a lightly doped MEG sample with ~63 layers. Theoretical differential THz transmission (c) at a substrate temperature of 300 K for a few different pump fluences and (d) at a pump fluence of 1.5 μJ/cm^2 for a few different substrate temperatures for disorder-free undoped graphene.

We also perform phenomenological fits to the data in Figure 2.2.7(a) and (b) and we discover that the differential THz transmission evolves from a faster mono-exponential relaxation form at room temperature to a slower bi-exponential relaxation form at cryogenic temperatures. As we explain below, the fast carrier relaxation component is

governed by optical phonon emission. A summary of the extracted carrier relaxation times as a function of pump fluence at room temperature for two MEG samples with ~35 and ~63 layers is presented in Figure 2.2.8(a). We note that the relaxation times at room temperature do not depend on the number of layers, which supports the interpretation that the measured THz carrier dynamics are dominated by the large number of top layers with low doping. This conclusion is further supported by the fact that the maximum differential THz transmission signal scales linearly with the number of layers (see Figure 2.2.9(a)). In addition, the relaxation times of graphene samples with low doping are in the range of ~4-7 ps, which is longer than the relaxation times for graphene samples with high doping (see Figure 2.2.5(a)), because the efficiency of carrier-carrier scattering increases with doping density. At cryogenic temperatures, we extract both short and long carrier relaxation times from the bi-exponential fits, which we associate with two distinct cooling mechanisms. Figure 2.2.8(b) shows the short relaxation times, which we attribute to carrier-optical-phonon scattering, as a function of substrate temperature for variable pump fluence for the MEG sample with ~63 layers. We note that the short relaxation times of graphene samples with low doping are weakly dependent on the pump fluence, but strongly dependent on the substrate temperature.

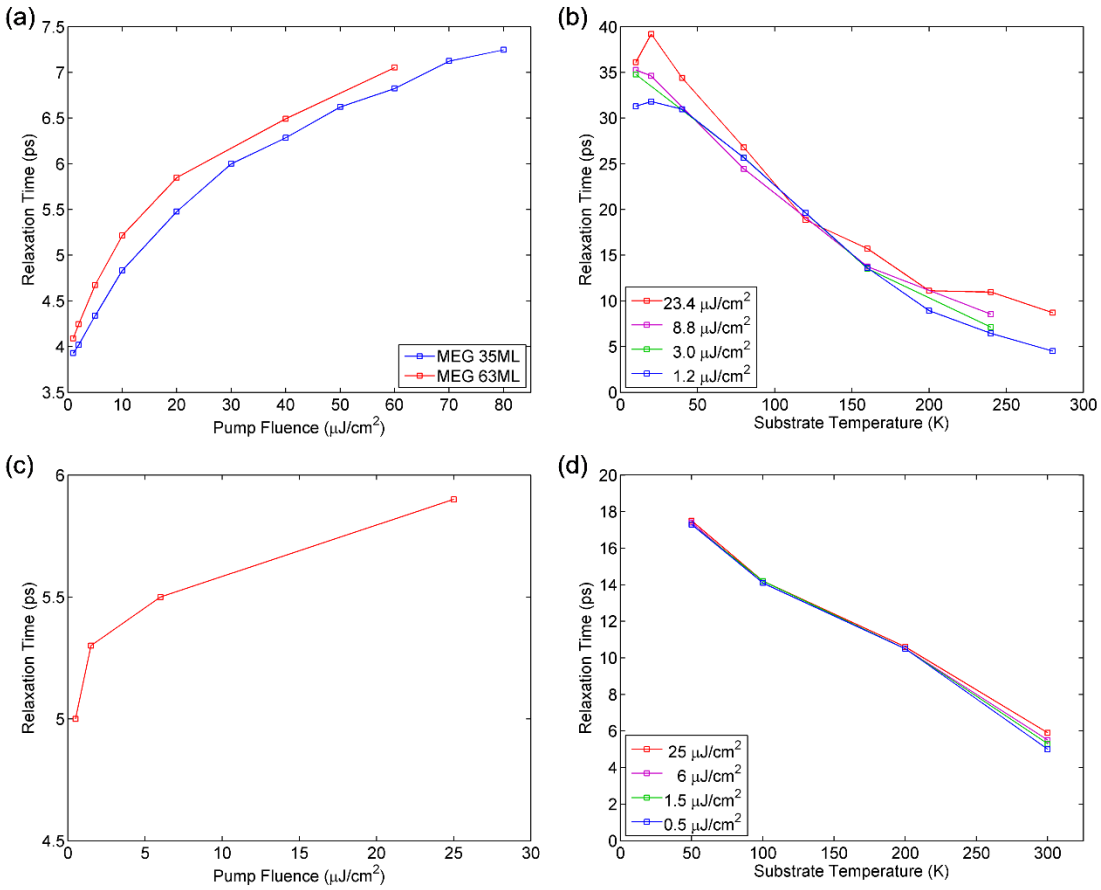

Figure 2.2.8 – Experimental carrier relaxation times as a function of (a) pump fluence at a substrate temperature of 300 K and (b) substrate temperature for a few different pump fluences for lightly doped MEG samples. Theoretical carrier relaxation times as a function of (c) pump fluence at a substrate temperature of 300 K and (d) substrate temperature for a few different pump fluences for disorder-free undoped graphene.

Figure 2.2.7(c) and (d) show the THz carrier dynamics calculated within the microscopic theory for disorder-free undoped graphene ($|E_F|$ = 0 meV) under similar experimental conditions. The theoretical results reproduce again all trends observed in the experiments. As in the high doping case, the hot-carrier relaxation occurs via the interplay between efficient carrier-carrier scattering and carrier-optical-phonon scattering. Figure 2.2.8(c) and (d) also show the calculated carrier relaxation times to directly compare with the experiments. In contrast to the high doping case, however, the relaxation times decrease significantly with increasing substrate temperature. In the microscopic theory, the impact of substrate-temperature-dependent carrier-phonon scattering on the THz carrier dynamics is found to be negligible; instead, the initial Fermi surface, where the THz probe pulse acts on the carriers, strongly depends on the substrate temperature for undoped graphene.

Additionally, the fewer thermal carriers are present, the less efficient carrier-carrier scattering is, and this results in longer relaxation times. The theory also shows a modest increase in the relaxation times with increasing pump fluence that can be traced back to hot phonon effects.

At low substrate temperatures, the THz carrier dynamics in the MEG samples with low doping show a long tail on the timescale of hundreds of picoseconds, corresponding to the slow carrier relaxation component in the bi-exponential decay. We analyze the physical origin of this dynamics in Section 2.3, as the underlying processes become more complex. In particular, the THz carrier dynamics become dependent on the number of layers in the MEG sample, indicating that interlayer thermal coupling effects are important. It suffices to emphasize here that the initial fast carrier relaxation on the timescale of tens of picoseconds is fully accounted for by the combined effect of carrier-carrier scattering and carrier-optical-phonon scattering in the absence of disorder.

To further illustrate the excellent agreement between the experimental data and the theoretical calculations, we compare the maximum absolute values of the THz carrier dynamics of MEG samples with low doping density. Figure 2.2.9(a) and (b) show the maximum absolute value of the differential THz transmission at the peak of the THz probe pulse, $max\{|\Delta t/t|\}$, as a function of pump fluence and substrate temperature, respectively, for MEG samples with low doping, while Figure 2.2.9(c) and (d) show the results obtained within the microscopic theory for disorder-free undoped graphene ($|E_F|$ = 0 meV) under similar experimental conditions. Similarly, we observe that the theory captures very well the saturation of the $max\{|\Delta t/t|\}$ signal with the pump fluence and its decrease with the substrate temperature. We can also point out that the maximum absolute value of the differential THz transmission scales roughly linearly with the number of graphene layers, because the intraband THz conductivities of the individual layers simply add up to first order.

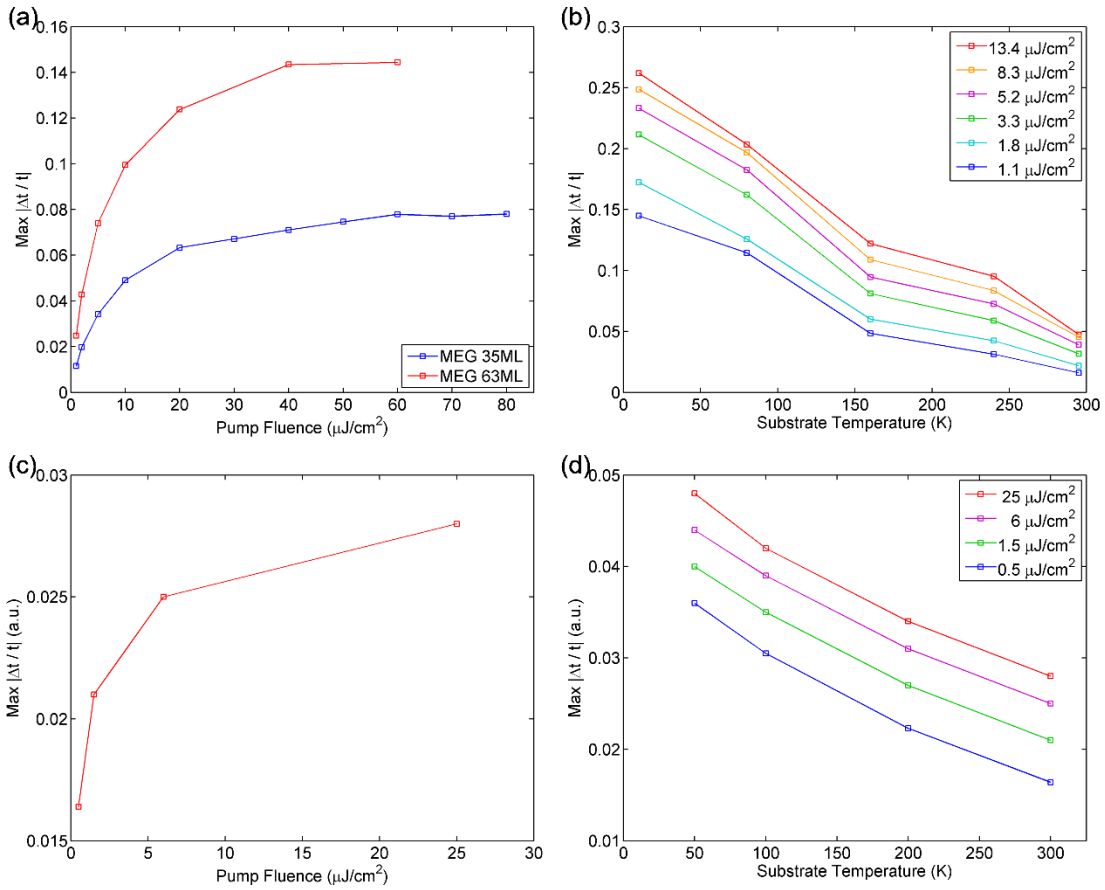

Figure 2.2.9 – Maximum absolute value of experimental differential THz transmission as a function of (a) pump fluence at a substrate temperature of 300 K and (b) substrate temperature for a few different pump fluences for lightly doped MEG samples. Maximum absolute value of theoretical differential THz transmission as a function of (c) pump fluence at a substrate temperature of 300 K and (d) substrate temperature for a few different pump fluences for disorder-free undoped graphene.

We now turn to a discussion of the theoretical approach used to calculate the dynamic THz response described above. The theory is based on the density matrix formalism providing microscopic access to the time- and momentum-resolved dynamics of the carrier occupation, the phonon population for different optical and acoustic modes, and the microscopic polarization determining the optical excitation of a disorder-free graphene system. The full graphene Bloch equations are given in Section 2.2.3. The theory includes all relevant optical and acoustic phonon modes. We have found that, by selectively switching on and off the different scattering processes in the model, the acoustic modes have negligible contribution to the observed THz carrier dynamics on the timescale of tens of picoseconds; the observed dynamics may be fully accounted for by the combined effect of carrier-optical-phonon scattering (which transfers energy from the carrier system to the

lattice) and carrier-carrier scattering (which rethermalizes the carrier population as high energy carriers lose their energy to the lattice).

The theory is an extension of the methods developed previously [32, 33, 34, 36, 39, 40]. In this work, the theory is extended to rigorously include the effect of the THz probe pulse. The dominant contribution to the THz probe-induced carrier dynamics $\delta\rho_{\boldsymbol{k}}^{\lambda}(t)$ (change of carrier occupation at wavevector $\boldsymbol{k}$) are intraband transitions described by:

$$\frac{d}{dt}\delta\rho_{\boldsymbol{k}}^{\lambda}(t) = -\frac{e_0}{\hbar}\boldsymbol{E}\cdot\nabla_{\boldsymbol{k}}\rho_{\boldsymbol{k}}^{\lambda,0}(t) - \Gamma_{\lambda\boldsymbol{k}}^{0}(t)\delta\rho_{\boldsymbol{k}}^{\lambda}(t), \tag{2.2.2}$$

where $\boldsymbol{E}$ represents the THz probe pulse, $\Gamma_{\lambda\boldsymbol{k}}^{0}(t)$ is the dominant contribution of the linearized scattering kernel, and $\rho_{\boldsymbol{k}}^{\lambda,0}(t)$ is the time-dependent pump-induced carrier population obtained by solving the full graphene Bloch equations. Accounting microscopically for carrier-carrier and carrier-phonon interactions, we calculate the macroscopic intraband current density:

$$\boldsymbol{j}(t) = \frac{2e_0\hbar}{im_0L^2}\sum_{\boldsymbol{k},\lambda}\mathbf{M}_{\boldsymbol{k}}^{\lambda\lambda}\delta\rho_{\boldsymbol{k}}^{\lambda}(t), \tag{2.2.3}$$

induced by the THz probe and the resulting dynamic THz response by solving Equation 2.2.2. This approach allows for a direct one-to-one comparison between experiment and theory. As seen in the comparisons between experiment and theory above, this first-principles microscopic approach explains completely all experimental results without the need for any fitting parameters, phenomenological models, or extrinsic effects.

In order to obtain additional insight into the physics governing the THz carrier dynamics, we consider a simplified theoretical model by temporally assuming a constant time- and momentum-independent scattering kernel for the THz probe-induced carrier dynamics; we show in Section 2.2.3 that this reduces Equations 2.2.2 and 2.2.3 to a standard Drude model. In this case the intraband current is determined for an arbitrary THz frequency by the gradient of the carrier distribution (see Equation 2.2.2) in terms of its carrier temperature T and Fermi level ε_F via:

$$j(T,\varepsilon_F) \propto Tln\left(2 + 2cosh\left(\frac{\varepsilon_F}{k_BT}\right)\right). \tag{2.2.4}$$

The resulting delay-dependent Drude-like THz response is given by:

$$\Delta t/t(\tau) \propto j\big(T_0, \varepsilon_{F,0}\big) - j(T(\tau), \varepsilon_F(\tau)), \tag{2.2.5}$$

where $\varepsilon_{F,0}$ and T_0 denote the initial Fermi level and carrier temperature before the arrival of the optical pump pulse at τ = 0. The time-varying carrier temperature $T(\tau)$ and quasi-Fermi level $\varepsilon_F(\tau)$ are formed after the thermalization of the pump-induced non-equilibrium carrier population. The Drude-like differential THz transmission $\Delta t/t$ (see Equation 2.2.5) calculated for disorder-free highly doped graphene ($|E_F|$ = 300 meV) is mapped in Figure 2.2.10(a). It is apparent (see the dashed line) that if the effect of the optical pump pulse was only to heat the carriers without changing the Fermi level ($\varepsilon_F = \varepsilon_{F,0}$), then a *negative* sign of the $\Delta t/t$ signal would always be observed. We conclude that, for a constant $\Gamma^0_{\lambda \boldsymbol{k}}(t) = \Gamma$, carrier heating alone cannot explain the positive sign of the differential THz transmission observed in highly doped graphene.

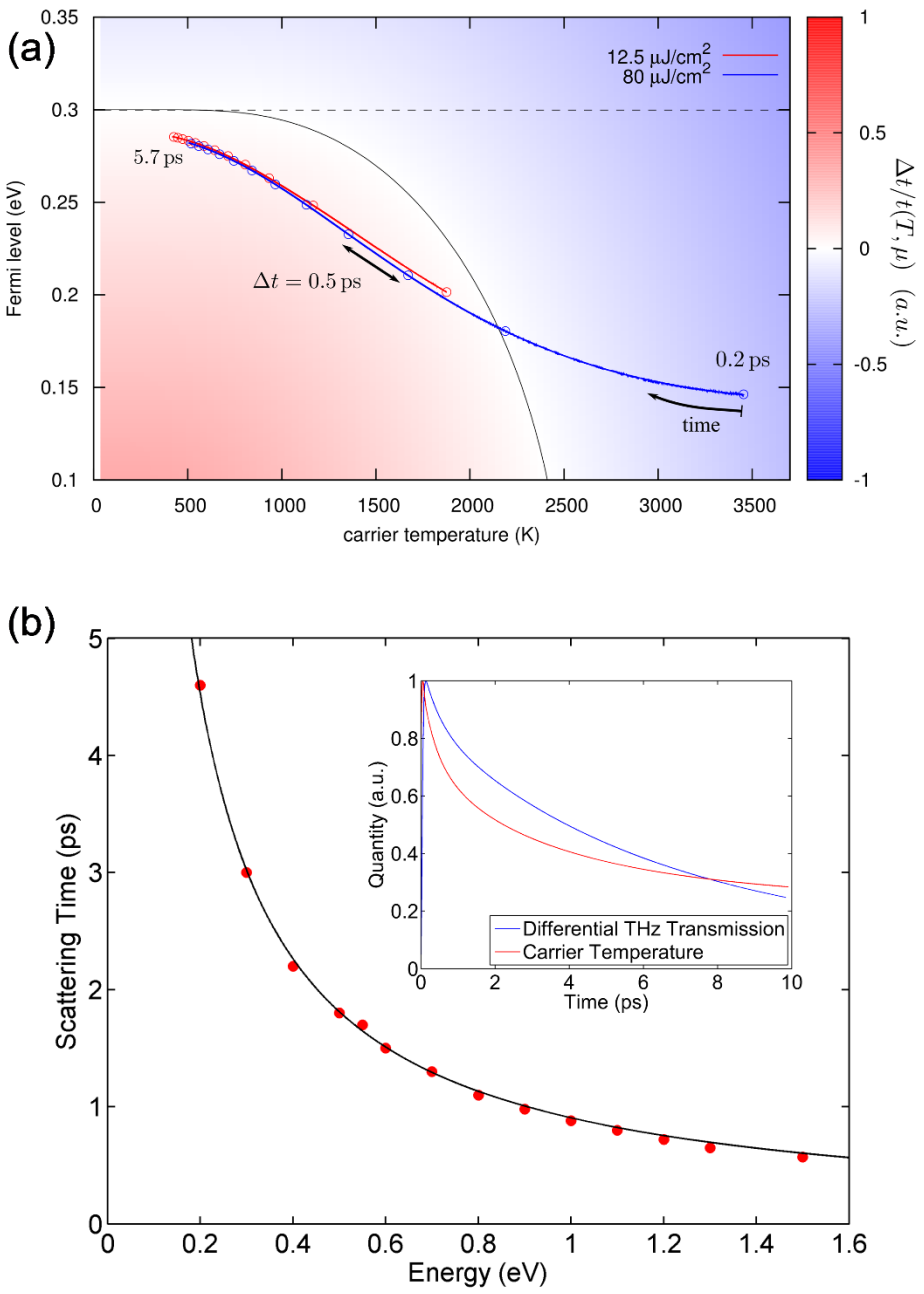

Figure 2.2.10 – (a) Differential THz transmission expected from a Drude model for an initial carrier temperature of 300 K and a Fermi level of 300 meV as a function of the transient carrier temperature and Fermi level. (b) Theoretical carrier scattering time as a function of carrier energy at a substrate temperature of 300 K for disorder-free undoped graphene. (Inset: Comparison between theoretical differential THz transmission and theoretical carrier temperature dynamics at a substrate temperature of 300 K and a pump fluence of 1.5 μJ/cm^2 for disorder-free undoped graphene.)

Figure 2.2.10(a) also illustrates the pump-induced temporal evolution of $T(\tau)$ and $\varepsilon_F(\tau)$ obtained by solving the full graphene Bloch equations within this approximation for low and high excitation (12.5 μJ/cm^2 (red line) and 80 μJ/cm^2 (blue line)). Interestingly,

we find not only carrier heating, but also a transient decrease of the quasi-Fermi level which reduces the THz absorption, as implied by Equation 2.2.4. Obviously, the pump-induced shift of the Fermi level outweighs the impact of carrier heating. As a consequence, we find a *positive* sign of the $\Delta t/t$ signal for the lower pump fluence (red line) at zero time delay and for the higher pump fluence (blue line) just after ~0.8 ps. Thus, the positive $\Delta t/t$ signal for highly doped graphene observed in the measurements can be explained to a large extent by a standard Drude model with constant Γ, provided that the carrier heating and cooling dynamics as well as the Fermi level dynamics are described correctly. Previously, the observation of a positive differential THz transmission in doped graphene has been attributed phenomenologically to a pump-induced increase in the carrier scattering rate, and a corresponding decrease of the THz conductivity within a Drude model [44, 45, 46], which is essentially a metal-like behavior, although the mechanism responsible for the increase in the carrier scattering rate could not be positively identified. Here, we find that the positive $\Delta t/t$ signal can be partly explained within a simple Drude picture as a consequence of the Fermi level shift. However, the simple Drude model is not sufficient to explain the behavior at higher pump fluence, for which the short time dynamics would exhibit a negative $\Delta t/t$ signal, unless other phenomenological parameters such as a carrier heating efficiency [47, 48] or a non-monotonic carrier-temperature-dependent Drude weight [49] are included.

A complete understanding is obtained by applying the full microscopic formalism, Equations 2.2.2 and 2.2.3, including the explicitly time- and momentum-dependent scattering rates $\Gamma^0_{\lambda \boldsymbol{k}}(t)$ of the THz probe-induced carrier dynamics. The results are shown in Figure 2.2.4(c) and (d), exhibiting excellent agreement with the experiment, for low as well as high pump fluence. Specifically, we observe, in both experiment and theory, an overall positive differential THz transmission at all time delays and all pump fluences. Thus, the microscopic model for the pump-induced carrier scattering is essential to capture the very initial THz carrier dynamics correctly. In the regime of high fluence and short time, even if carrier thermalization is complete, a constant carrier scattering rate approximation cannot be trusted. In particular, we find that in the strong excitation regime efficient time-dependent Coulomb scattering provides the major contribution. All results

presented in the comparisons with experiment above are obtained from the full microscopic formalism beyond the standard Drude model.

An important question in the hot-carrier dynamics is the possible energy dependence of the carrier scattering rate (inverse time), and the consequences for the THz carrier dynamics. The microscopic theory calculations performed here give further insight into this issue. We consider the carrier scattering rate as the exponential decay of the carrier occupation (see Section 2.2.3). For weak THz probe excitations as is the case here, the Boltzmann equation reveals a direct relation between the microscopic scattering rates and the exponential decay of the carrier occupation. By fitting the numerically calculated hot-carrier dynamics, we obtain the energy relaxation time $\tau(\varepsilon)$ of the photoexcited carriers. Figure 2.2.10(b) shows the calculated carrier scattering time $\tau(\varepsilon)$ as a function of carrier energy ε for disorder-free undoped graphene ($|E_F|$ = 0 meV) at a substrate temperature of 300 K. We observe that the carrier scattering time is precisely *inverse* to the carrier energy, $\tau(\varepsilon) = \beta/|\varepsilon|$ (with $\beta \approx 0.9$ eV ps), over a very broad energy range ($|\varepsilon|$ ~ 0.2-1.5 eV) in agreement with previous experimental studies on MEG [58] and graphite [59, 60]. These results are in sharp contrast with the linear relation on carrier energy, $\tau(\varepsilon) = \alpha|\varepsilon|$, [61, 62] that is inferred from electrical transport measurements in some graphene samples. This is attributed to the fact that in electrical transport measurements carriers have energies close to the Fermi energy and carrier scattering in these graphene samples is dominated by extrinsic mechanisms such as defects, charge impurities, wrinkles and ripples [26, 27] likely introduced during the multistep synthesis, transfer and fabrication processes. It has been extensively investigated that when graphene is transferred to an arbitrary substrate (e.g. SiO_2), local spatial charge inhomogeneities form under overall charge-neutral conditions due to disorder, charge impurities or surface corrugation [19, 20, 21]. These charge fluctuations or puddles obscure the low energy graphene band structure and prevent one from studying the true graphene physics near the Dirac point. Such effects can be minimized by placing the graphene on ultra-smooth substrates such as hexagonal boron nitride (h-BN) [28] or by suspending it [29]. The lightly doped layers in MEG are naturally protected, which makes them an ideal graphene system for studying the carrier dynamics within a few meV of the Dirac point.

Finally, the microscopic theory allows us to directly address another important question in ultrafast time-resolved THz spectroscopy, namely, to what extent does the differential THz transmission measure the carrier temperature dynamics? Rigorously speaking, the transient differential THz transmission and transient carrier temperature are not directly proportional to each other, but are connected through the macroscopic current density. The inset of Figure 2.2.10(b) shows a direct comparison between the differential THz transmission and the carrier temperature dynamics calculated within the microscopic theory for disorder-free undoped graphene ($|E_F|$ = 0 meV) at a substrate temperature of 300 K and a pump fluence of 1.5 μJ/cm^2. We can clearly see that the differential THz transmission does *not* exactly follow the carrier temperature dynamics, which clearly reveals that both transient carrier temperature and Fermi level shifts are essential to capture the dynamic THz response correctly. In particular, the relaxation times extracted from the decay of the differential THz transmission are in general not exactly equal to the electronic cooling times, although they may serve as a useful approximation as the two dynamics relax on similar timescales.

Section 2.2.3 Microscopic Theory

In this section, we turn our attention to a detailed presentation of the microscopic theory of carrier-carrier and carrier-phonon interactions in pristine disorder-free graphene.

First, we discuss the microscopic theory calculation of the dynamic THz response of graphene. The dynamic THz response due to an optical excitation can be microscopically addressed by evaluating the graphene Bloch equations, which describe the coupled dynamics of the carrier occupation $\rho_{\boldsymbol{k}}^{\lambda}$ at the wave vector $\boldsymbol{k}$ in conduction ($\lambda = c$) and valence band ($\lambda = v$), the microscopic polarization $p_{\boldsymbol{k}}$, and the phonon population $n_{\boldsymbol{q}}^{j}$ at the momentum $\boldsymbol{q}$ for different optical and acoustic phonon modes j [32]:

$$\frac{d}{dt}\rho_{\boldsymbol{k}}^{\lambda} = -\frac{e_0}{\hbar}\boldsymbol{E}\cdot\nabla_{\boldsymbol{k}}\rho_{\boldsymbol{k}}^{\lambda} + 2\Im[\Omega_{\boldsymbol{k}}^{vc*}p_{\boldsymbol{k}}] + \Gamma_{\lambda\boldsymbol{k}}^{in}\left[1-\rho_{\boldsymbol{k}}^{\lambda}\right] - \Gamma_{\lambda\boldsymbol{k}}^{out}\rho_{\boldsymbol{k}}^{\lambda}, \tag{2.2.6}$$

$$\frac{d}{dt}p_{\boldsymbol{k}} = [i\Delta\omega_{\boldsymbol{k}} - \gamma_{\boldsymbol{k}}]p_{\boldsymbol{k}} - i\Omega_{\boldsymbol{k}}^{vc}[\rho_{\boldsymbol{k}}^{c} - \rho_{\boldsymbol{k}}^{v}]. \tag{2.2.7}$$

An external excitation of the system is considered via the Rabi-frequency $\Omega_{\boldsymbol{k}}^{vc}$ accounting for interband transitions, where $\Delta\omega_{\boldsymbol{k}} = v_F k$ is the transition frequency and v_F is the Fermi

velocity. Furthermore, we include a drift term $\boldsymbol{E}\cdot\nabla_{\boldsymbol{k}}\rho_{\boldsymbol{k}}^{\lambda}$ expressing the light-induced intraband transitions, which are crucial for the THz dynamics driven by the probe pulse. The carrier-carrier and carrier-phonon interactions are taken into account by a Boltzmann-like equation with time- and momentum-dependent scattering rates $\Gamma_{\lambda\boldsymbol{k}}^{in/out}$ for the carrier occupations and by the diagonal dephasing $\gamma_{\boldsymbol{k}}=\frac{1}{2}\sum_{\lambda}\Gamma_{\lambda\boldsymbol{k}}^{in}+\Gamma_{\lambda\boldsymbol{k}}^{out}$ for the microscopic polarization. The explicit form of the many-particle contributions as well as the equation for the phonon dynamics can be found elsewhere [32, 53].

The differential THz transmission is given by $\Delta t/t(\tau,\omega)\propto\alpha^{(t)}(\omega)-\alpha^{(p,t)}(\omega)$ with the absorption coefficient $\alpha^{(p,t)}(\omega)$ including both the pump and the probe pulse and $\alpha^{(t)}(\omega)$ including only the probe pulse. The absorption $\alpha(\omega)=\Im\left[j(\omega)/\left(\epsilon_0\omega^2A(\omega)\right)\right]$ is determined by the macroscopic current density [53]:

$$\boldsymbol{j}(\omega)=\frac{4e_0\hbar}{m_0L^2}\sum_{\boldsymbol{k}}\mathbf{M}_{\boldsymbol{k}}^{vc}\Im[p_{\boldsymbol{k}}(\omega)]+\frac{2e_0\hbar}{im_0L^2}\sum_{\boldsymbol{k},\lambda}\mathbf{M}_{\boldsymbol{k}}^{\lambda\lambda}\rho_{\boldsymbol{k}}^{\lambda}(\omega), \tag{2.2.8}$$

where $\mathbf{M}_{\boldsymbol{k}}^{\lambda\lambda'}$ is the optical matrix element, m_0 is the free electron mass and L^2 is the structure area of the system that cancels out after performing the summation over $\boldsymbol{k}$. The current contains an interband contribution that is driven by the microscopic polarization $p_{\boldsymbol{k}}(\omega)$ and an intraband contribution that is determined by the carrier occupation $\rho_{\boldsymbol{k}}^{\lambda}(\omega)$. Assuming a weak THz probe pulse, $\rho_{\boldsymbol{k}}^{\lambda}(\omega)$ can be treated perturbatively:

$$\rho_{\boldsymbol{k}}^{\lambda}(t)=\rho_{\boldsymbol{k}}^{\lambda,0}(t)+\delta\rho_{\boldsymbol{k}}^{\lambda}(t), \tag{2.2.9}$$

where $\rho_{\boldsymbol{k}}^{\lambda,0}(t)$ is the pump pulse-induced occupation, while $\delta\rho_{\boldsymbol{k}}^{\lambda}(t)$ describes the weak carrier occupation excited by the THz probe pulse.

To obtain the dynamic THz response from the differential THz transmission spectra, we exploit the fact that ultrafast carrier-carrier scattering in graphene forms a uniform Fermi-Dirac distribution within the first tens of femtoseconds after the excitation [30, 37, 54] and the subsequent dynamics is fully characterized by the temporal evolution of the transient temperature $T_{\lambda}(t)$ and transient Fermi level $\varepsilon_{F,\lambda}(t)$ of electrons and holes. Thus, by iteratively evaluating $T_{\lambda}(t)$ and $\varepsilon_{F,\lambda}(t)$ on the basis of the numerically calculated carrier dynamics at each time step, we obtain the pump pulse-induced occupation $\rho_{\boldsymbol{k}}^{\lambda,0}(t)$.

For the dynamics of the probe pulse-induced carrier occupation, we derive a separate equation of motion yielding:

$$\frac{d}{dt}\delta\rho_{\boldsymbol{k}}^{\lambda}(t) = -\frac{e_0}{\hbar}\boldsymbol{E}\cdot\nabla_{\boldsymbol{k}}\rho_{\boldsymbol{k}}^{\lambda,0}(t) - \Gamma_{\lambda\boldsymbol{k}}^{0}(t)\delta\rho_{\boldsymbol{k}}^{\lambda}(t), \tag{2.2.10}$$

where $\Gamma_{\lambda\boldsymbol{k}}^{0}(t) = \Gamma_{\lambda\boldsymbol{k}}^{in,0}(t) + \Gamma_{\lambda\boldsymbol{k}}^{out,0}(t)$ is the diagonal contribution stemming from the Boltzmann-like scattering terms (see Equation 2.2.6), which are independent of the probe pulse as denoted by the index 0. Non-linear contributions in the probe pulse and non-diagonal terms have been neglected here. For the response of the THz probe field, the interband contribution in Equation 2.2.8 is negligibly small, since the intraband processes are dominating. By inserting the numerically evaluated Fourier transform of $\delta\rho_{\boldsymbol{k}}^{\lambda}(t)$ in Equation 2.2.8, we have microscopic access to the Coulomb- and phonon-assisted dynamics induced by the THz probe pulse.

Next, we discuss the microscopic theory calculation of the carrier scattering time in graphene. The collision part of the Boltzmann equation, which is given by:

$$\frac{d}{dt}\rho_{\boldsymbol{k}}^{\lambda} = \Gamma_{\lambda\boldsymbol{k}}^{in}\left[1-\rho_{\boldsymbol{k}}^{\lambda}\right] - \Gamma_{\lambda\boldsymbol{k}}^{out}\rho_{\boldsymbol{k}}^{\lambda}, \tag{2.2.11}$$

can be rewritten as:

$$\frac{d}{dt}\rho_{\boldsymbol{k}}^{\lambda} = -\frac{\rho_{\boldsymbol{k}}^{\lambda}-\tau_{\lambda\boldsymbol{k}}\Gamma_{\lambda\boldsymbol{k}}^{in}}{\tau_{\lambda\boldsymbol{k}}}, \tag{2.2.12}$$

where we define:

$$\tau_{\lambda\boldsymbol{k}} := \frac{1}{\Gamma_{\lambda\boldsymbol{k}}^{in}+\Gamma_{\lambda\boldsymbol{k}}^{out}}. \tag{2.2.13}$$

The term $\tau_{\lambda\boldsymbol{k}}\Gamma_{\lambda\boldsymbol{k}}^{in}$ can be written as:

$$\tau_{\lambda\boldsymbol{k}}\Gamma_{\lambda\boldsymbol{k}}^{in} = \frac{\Gamma_{\lambda\boldsymbol{k}}^{in}}{\Gamma_{\lambda\boldsymbol{k}}^{in}+\Gamma_{\lambda\boldsymbol{k}}^{out}} = \frac{1}{1+\Gamma_{\lambda\boldsymbol{k}}^{out}/\Gamma_{\lambda\boldsymbol{k}}^{in}}. \tag{2.2.14}$$

Accounting only for weak excitations, the scattering rates can be approximated with the equilibrium rates $\Gamma_{\lambda\boldsymbol{k}}^{in/out,0}$ fulfilling the principle of detailed balance (D.B.):

$$\frac{\Gamma_{\lambda\boldsymbol{k}}^{out}}{\Gamma_{\lambda\boldsymbol{k}}^{in}} \approx \frac{\Gamma_{\lambda\boldsymbol{k}}^{out,0}}{\Gamma_{\lambda\boldsymbol{k}}^{in,0}} = e^{(\varepsilon_k-\varepsilon_F)/k_BT}. \tag{2.2.15}$$

Thus, Equation 2.2.14 represents the initial Fermi distribution $\rho_{\boldsymbol{k}}^{\lambda,0} \approx \tau_{\lambda \boldsymbol{k}} \Gamma_{\lambda \boldsymbol{k}}^{in}$ and the Boltzmann equation yields the relaxation-time model:

$$\frac{d}{dt}\rho_{\boldsymbol{k}}^{\lambda} = -\frac{\rho_{\boldsymbol{k}}^{\lambda} - \rho_{\boldsymbol{k}}^{\lambda,0}}{\tau_{\lambda \boldsymbol{k}}}. \tag{2.2.16}$$

Within the approximation in Equation 2.2.15, Equation 2.2.16 clearly reveals a direct relation between the microscopic scattering rates and the exponential decay of the carrier population. However, by fitting the numerical data stemming from the full scattering equation (Equation 2.2.11), our method for the determination of the carrier scattering time (see Figure 2.2.10(b) in Section 2.2.2) goes beyond the relaxation-time approximation.

To obtain a simple Drude model, we approximate the scattering rate as a constant: $\Gamma_{\lambda \boldsymbol{k}}^{0}(t) = \Gamma$. The Fourier transform of Equation 2.2.10 yields:

$$\delta\rho_{\boldsymbol{k}}^{\lambda}(\omega) = i\omega \boldsymbol{e}_x \frac{e_0 A_0}{\hbar} \times \frac{1}{i\omega - \Gamma} \nabla_{\boldsymbol{k}} \rho_{\boldsymbol{k}}^{\lambda,0}. \tag{2.2.17}$$

The intraband current density is given by:

$$\boldsymbol{j}(\omega) = \frac{2e_0\hbar}{im_0 L^2} \sum_{\boldsymbol{k},\lambda} \mathbf{M}_{\boldsymbol{k}}^{\lambda\lambda} \delta\rho_{\boldsymbol{k}}^{\lambda}(\omega). \tag{2.2.18}$$

Assuming a Fermi-Dirac distribution for the carrier occupation, the gradient yields:

$$\nabla_{\boldsymbol{k}} \rho_{\boldsymbol{k}}^{\lambda} = -\sigma_\lambda \boldsymbol{e}_{\boldsymbol{k}} \frac{v_F \hbar}{4k_B T} sech^2[\sigma_\lambda (k v_F \hbar - \varepsilon_F)/2k_B T], \tag{2.2.19}$$

where σ_λ is 1 (-1) for $\lambda = c$ $(\lambda = v)$ and ε_F is the Fermi level. For a constant scattering rate Γ and with the optical intraband matrix element $\mathbf{M}_{\boldsymbol{k}}^{\lambda\lambda} \approx i\sigma_\lambda M \boldsymbol{e}_{\boldsymbol{k}}$ ($\sigma_c = 1$ and $\sigma_v = -1$), the intraband current can be evaluated analytically using Equations 2.2.17 and 2.2.18:

$$j(\omega) = \frac{e_0^2 M A_0 k_B}{m_0 \pi c^2} \left[i \frac{\Gamma}{\Gamma^2 + \omega^2} - \frac{\omega}{\Gamma^2 + \omega^2} \right] \times T\left[ln\left(1 + e^{\mu/k_B T}\right) + ln\left(1 + e^{-\mu/k_B T}\right) \right], \tag{2.2.20}$$

which corresponds to the Drude model. For a constant Γ and an arbitrary THz frequency, Equation 2.2.20 yields Equation 2.2.4 in Section 2.2.2.

We note that in principle a $\boldsymbol{k}$-dependent $\Gamma_{\boldsymbol{k}}$ could also be considered in Equations 2.2.17 and 2.2.18 to obtain a more advanced Drude model. However, this would require also an approximate analytical model for $\Gamma_{\boldsymbol{k}}$. We again emphasize that we go beyond the

approximation by using the numerically calculated microscopic scattering rates for the evaluation of the current.

Section 2.3 Multilayer Epitaxial Graphene

The dynamics of electrons in atomic-layer two-dimensional (2D) electron systems like graphene is a subject of considerable current interest, partly because of its relevance to a wide variety of potential electronic and optoelectronic applications. Many proposed and prototype devices employ stacks composed of many 2D electronic material layers. Examples of multilayer systems include multilayer epitaxial graphene (MEG) [10, 11], van der Waals bonded layered sheets [63, 64], transition metal dichalcogenides [65] and others [66]. In these structures the interactions between electrons in different layers in the stack becomes a subject of key importance. One important property is that phonon-mediated interlayer thermal coupling is weak relative to that in bulk 3D materials. In this section, we demonstrate, however, that Coulomb interactions between carriers in different layers of MEG provide an important mechanism for interlayer thermal transport even though all electronic states are strongly confined to individual 2D layers. This effect is manifested in the cooling dynamics of hot carriers in ultrafast time-resolved terahertz (THz) spectroscopy. We develop a theory of interlayer Coulomb coupling containing no free parameters that accounts for the experimentally observed trends in hot-carrier dynamics as temperature and the number of layers is varied.

In van der Waals bonded or rotationally disordered multilayer stacks of 2D layers, the electronic states remain tightly confined within individual 2D layers. As a result, electron-phonon interactions occur primarily within layers and interlayer electrical conductivities are low. In addition, strong covalent in-plane intralayer bonding combined with weak van der Waals interlayer bonding results in weak phonon-mediated thermal coupling between the layers. In the example of MEG, rotational stacking arrangements decouple electronic states localized in different layers [13, 15]. As a result, interlayer thermal coupling is strongly reduced relative to typical bulk behavior in 3D materials.

The question thus arises as to what other mechanisms can contribute to thermal equilibration between different layers. We consider this question here in the context of hot carrier dynamics. If electrons are heated in one layer (e.g. by optical excitation or electrical

injection), they will normally cool to the lattice temperature by optical phonon emission at high carrier energies, and by acoustic phonon emission at low carrier energies. For graphene, it is well established that electron cooling by acoustic phonons is very efficient in highly doped layers [50, 51, 67]. The situation is quite different, however, for lightly doped or nearly neutral graphene in which a small joint-density-of-states for electronic transitions combines with a small acoustic phonon energy at typical scattering wavevectors to diminish the acoustic phonon cooling power [50, 51]. (The cooling power in this limit can, however, be substantially enhanced by disorder, because it relaxes momentum conservation limits [52, 55, 56] on allowed processes.)

An interesting case thus arises when a multilayer stack contains both highly doped (HD) and nearly neutral lightly doped (LD) graphene layers. This is exactly the situation that occurs in MEG grown on the C-face of SiC [10, 11], and is likely to be relevant to gated multilayer 2D systems due to interlayer screening [23, 24]. If electrons are heated in the multilayer structure, then acoustic-phonon-mediated cooling would result in the rapid buildup of a thermal gradient between the HD and LD layers; the HD layers would quickly approach the lattice temperature, while carriers in the LD layers would remain hot. Eventually, of course, thermal equilibrium would be restored, as thermal energy flows from the LD to the HD layers. The HD layers can be a heat sink for the LD layers if there is an effective interlayer energy transfer mechanism.

In this section, we show that Coulomb scattering between electrons in LD and HD layers of MEG can provide an efficient means for interlayer thermal coupling, and provide an alternate mechanism for cooling of hot electrons in the LD layers that acts in parallel with acoustic-phonon-mediated intralayer cooling. This process is illustrated schematically in Figure 2.3.1(a). We note that interlayer thermal coupling via Coulomb scattering has been considered recently in the context of 2D electron gases in transport devices [68, 69]. We begin by outlining a heuristic analytical model calculation for a pair of graphene layers to establish the magnitude of the effect relative to acoustic-phonon-mediated intralayer cooling. This simple calculation establishes the significance of the effect; we then discuss how hot-carrier cooling in multilayer systems is accessible experimentally by ultrafast time-resolved THz spectroscopy and ultrafast infrared (IR) pump-probe spectroscopy

measurements. Following a discussion of the features of the data that point to interlayer energy transfer, we present the details of a theory of interlayer energy transfer via screened Coulomb interactions. The calculated cooling powers imply asymptotic cooling times on the sub-nanosecond scale. We show that the calculated dynamics and trends with lattice temperature and number of epitaxial graphene layers are fully consistent with the experimental results, without the need for any fitting parameters.

Section 2.3.1 Interlayer Energy Transfer Heuristics

In this section, we first ask whether or not interlayer Coulomb coupling can potentially dominate over acoustic phonon cooling [50] and disorder-assisted electron-phonon (supercollision) cooling [52] in multilayer graphene samples. A simple comparison of the cooling powers of the different mechanisms suggests that the answer is yes. The low-temperature cooling power Q^{el} of interlayer Coulombic energy transfer between a hot LD and a cold HD graphene layer is:

$$Q^{el} = \frac{\pi^2 k_B^4 \nu_{LD}}{15\hbar^3 v_F^2 \nu_{HD}} T^4 ln\left(\frac{E_{F,LD}}{k_B T}\right), \tag{2.3.1}$$

where $\nu_i = 2E_{F,i}/(\pi\hbar^2 v_F^2)$ is the density of states at the Fermi level. Equation 2.3.1 is plotted in Figure 2.3.1(b) as a function of electron temperature for Fermi level $E_{F,HD}$ = 300 meV in the HD layer and various Fermi levels $E_{F,LD}$ in the LD layer; even at very low carrier density in the LD layer, the cooling power is quite substantial. We can compare Equation 2.3.1 with the cooling powers of both acoustic phonon cooling $Q^a \propto T$ and disorder-assisted electron-phonon (supercollision) cooling $Q^{sc} \propto T^3$ of an isolated LD layer. The ratio of cooling powers Q^{el}/Q^a is plotted in Figure 2.3.1(c) as a function of electron temperature for $E_{F,HD}$ = 300 meV and various values of $E_{F,LD}$. As it can be expected, acoustic phonon cooling is very inefficient in graphene with very low carrier density. The ratio of cooling powers Q^{el}/Q^{sc} is also plotted in Figure 2.3.1(d) as a function of electron temperature (above the Bloch-Grüneisen temperature $T_{BG} \approx 5$ K) for $E_{F,HD}$ = 300 meV, $E_{F,LD}$ = 10 meV (typical for C-face MEG on SiC) and various values of the low-density-layer mean free path. It is apparent that for high quality graphene such as C-face MEG on SiC [18], interlayer Coulombic energy transfer can dominate for a wide range of electron temperatures and sample characteristics.

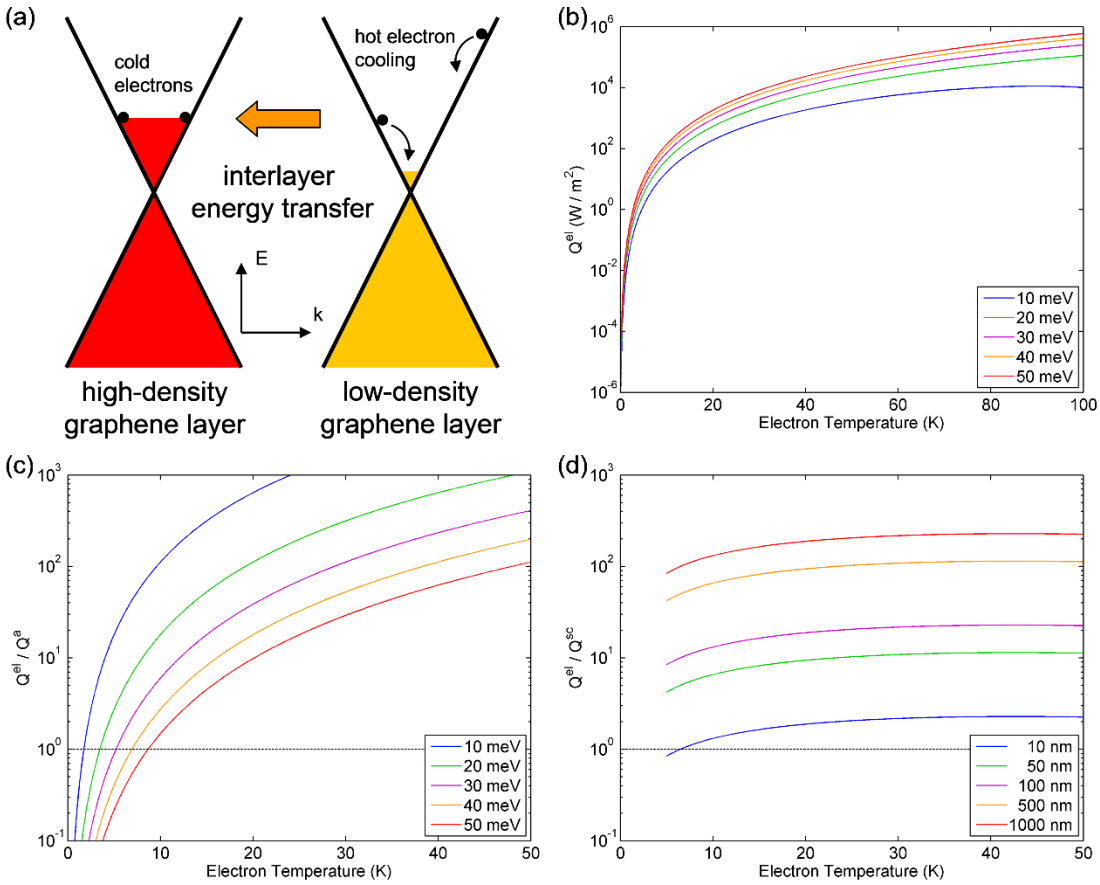

Figure 2.3.1 – (a) Schematic diagram of interlayer Coulombic energy transfer from a hot LD to a cold HD graphene layer. (b) Cooling power of interlayer Coulombic energy transfer Q^{el} as a function of electron temperature for Fermi level $E_{F,HD}$ = 300 meV in the HD graphene layer and various Fermi levels $E_{F,LD}$ in the LD graphene layer. (c) Ratio of cooling powers Q^{el}/Q^{a} as a function of electron temperature for $E_{F,HD}$ = 300 meV and various values of $E_{F,LD}$ showing that interlayer Coulombic energy transfer can dominate intralayer acoustic phonon cooling in the LD graphene layer. (d) Ratio of cooling powers Q^{el}/Q^{sc} as a function of electron temperature for $E_{F,HD}$ = 300 meV, $E_{F,LD}$ = 10 meV (typical for C-face MEG on SiC) and various values of the disorder mean free path in the LD graphene layer showing that interlayer Coulombic energy transfer can dominate intralayer disorder-assisted electron-phonon (supercollision) cooling in the LD graphene layer.

In the main body of this section, we investigate the physics of interlayer Coulomb coupling in MEG, grown on the C-face of single-crystal 4H-SiC(000$\bar{1}$) substrates by thermal decomposition of Si atoms [10, 11]. In Section 2.1, we mentioned that an important feature of this material is that it largely preserves distinct graphene-like electronic properties because of unique rotational stacking, which suppresses hybridization between low energy electronic states localized in neighboring planes of carbon atoms [13, 15]. MEG is doped by electron transfer from the interface with the supporting SiC substrate and the induced n-type carrier-density profile falls off rapidly with layer moving away from the

substrate (see Figure 2.1.2(b) in Section 2.1). We will refer to the few layers close to the SiC substrate, which have large carrier densities of $n_{HD} \geq 10^{12}$ cm^{-2} as determined from high-resolution angle-resolved photoemission spectroscopy (ARPES), scanning tunneling spectroscopy (STS), electronic transport, and ultrafast optical spectroscopy measurements [10, 11, 22, 23, 24], as high-density (HD) layers, and to those further away, whose carrier densities drop quickly [70] to the range of $n_{LD} \leq 10^{10}$ cm^{-2} as determined from STS, electronic transport, and magneto-optical spectroscopy measurements [10, 11], as low-density (LD) layers. The formation of local spatial charge inhomogeneities due to small amounts of disorder, impurities, or surface corrugation of the SiC substrate could explain the non-zero carrier density measured in the top layers of MEG [19, 20, 21].

In Section 2.2, we mentioned that when an MEG sample is illuminated with a short optical pulse, electrons are excited to high energies, leaving behind unoccupied states or holes. Due to strong intralayer carrier-carrier scattering, these hot carriers thermalize with the background of cold carriers within ~50 fs [30, 37, 54], forming two separate non-equilibrium Fermi-Dirac distributions for electrons and for holes. The electron and the hole quasi-Fermi levels subsequently merge within ~100-200 fs [54], establishing a uniform electron liquid within each layer i characterized by an elevated electron temperature, T_i. As the electron liquid cools, each layer's electron temperature approaches the equilibrium lattice temperature, T_L. It is generally accepted that initial fast cooling occurs in the first few picoseconds via the emission of energetic optical phonons, and that this process becomes increasingly inefficient as the electron energy falls below the relatively high optical phonon energy ($\hbar\omega_{op} \approx 200$ meV [14]). In the final stage of relaxation, low energy electronic cooling in an isolated layer would proceed by the much slower emission of acoustic phonons. Prior theoretical work has found that the rate of acoustic phonon cooling in disorder-free single-layer graphene is very strongly dependent on the carrier density, with cooling times ranging from tens of picoseconds for doping densities of ~10^{13} cm^{-2} to tens of nanoseconds for doping densities of ~10^{10} cm^{-2} [50, 51]. The strong carrier density dependence of the acoustic phonon emission implies that the LD and HD layers of MEG will exhibit very differing cooling rates following ultrafast optical excitation, leading to the buildup of a thermal gradient, which triggers an interlayer energy transfer.

We have applied two experimental techniques to probe the dynamics of the interlayer thermal energy transfer in MEG. The first is ultrafast time-resolved THz spectroscopy, which is a powerful tool for investigating the real time relaxation dynamics of photoexcited carriers, because it is sensitive to both the number of carriers and their distribution in energy. Due to the large number of layers in our MEG samples and the rapid decrease of carrier density with layer number, the measured differential THz transmission signal is dominated by the dynamic THz response of the many LD layers and reveals the cooling of the LD layers due to their coupling to the HD layers. The second is ultrafast degenerate IR pump-probe spectroscopy [23, 24], in which we optically inject hot carriers selectively into the LD layers and then observe directly the transfer of heat to the electron liquid in the most highly doped HD layer.

Section 2.3.2 THz Carrier Dynamics

In this section, we first consider the ultrafast time-resolved THz spectroscopy experiments. In Section 2.2, we discussed the dynamic THz response of pristine epitaxial graphene (EG), which is characteristic for a pristine disorder-free graphene layer. Here, we focus on the features of the THz carrier dynamics, which demonstrate the existence of interlayer energy transfer in MEG.

To study the THz carrier dynamics of MEG, we keep the delay of the sampling pulse fixed at the peak of the THz probe pulse, and we scan the pump-probe delay to map out the relaxation dynamics of the photoexcited carriers. Since the carrier-carrier scattering time in graphene is much shorter than the temporal duration of the THz probe, we study the relaxation of the THz transmission (or the THz conductivity) change induced by the optical pump in the limit, where it is determined by collective electronic cooling dynamics. Figure 2.3.2 shows the normalized differential THz transmission at the peak of the THz probe pulse, $\Delta t/t$, as a function of pump-probe delay for variable substrate temperature for an MEG sample with ~63 layers. At time zero, the optical pump photoexcites carriers in the MEG sample resulting in an overall increase of the THz conductivity and hence THz absorption, as manifested in a negative differential THz transmission. In Section 2.2, we mentioned that in graphene with very low doping, the increase of the electron temperature leads primarily to larger electron occupation in the conduction band and a corresponding

net increase of the THz conductivity, consistent with our interpretation that the measured dynamic THz response is dominated by the hot carriers in the many LD layers of MEG [42, 44, 45]. The differential THz transmission reaches its maximum magnitude within ~1 ps, with the rise time being limited mainly by the temporal duration of the THz probe. The differential THz transmission subsequently recovers as the thermalized hot carriers cool down to the substrate temperature with relaxation times ranging from a few picoseconds at room temperature to hundreds of picoseconds at cryogenic temperatures. The secondary decrease in the differential THz transmission at ~7 ps is due to a round-trip reflection of the optical pump inside the substrate that photoexcites additional carriers.

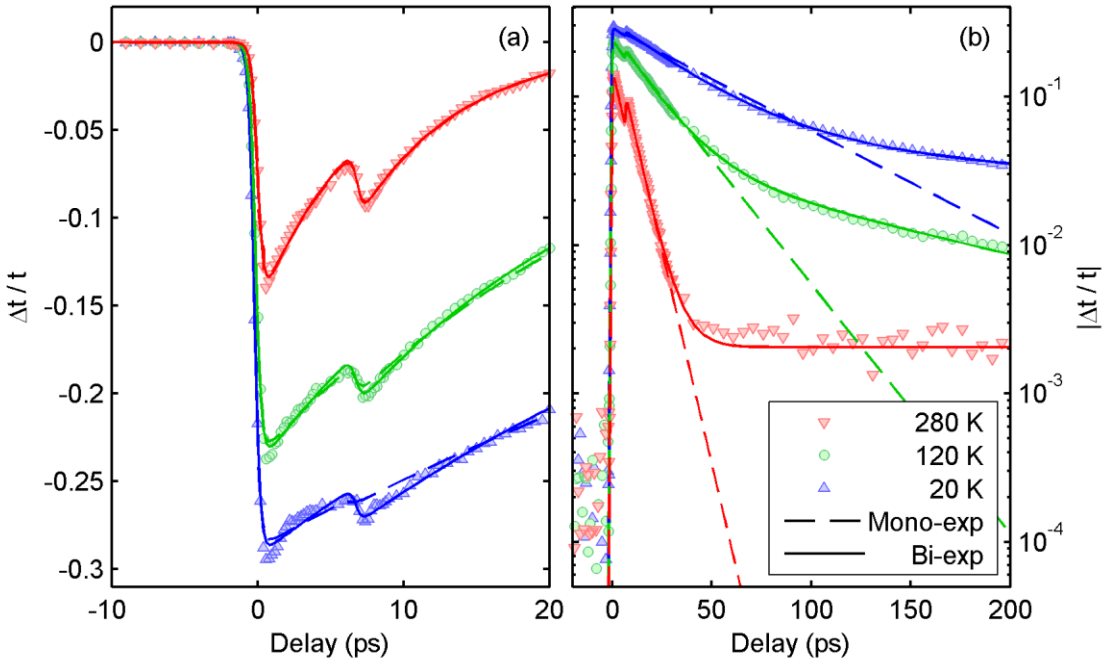

Figure 2.3.2 – (a) Linear and (b) logarithmic plots of differential THz transmission at a pump fluence of 23.4 μJ/cm^2 for a few different substrate temperatures for an MEG sample with ~63 layers.

We perform phenomenological fits to the experimental data in Figure 2.3.2, and we discover that the differential THz transmission evolves from a faster mono-exponential decay at room temperature to a slower bi-exponential decay at cryogenic temperatures. In Section 2.2, we discussed that the fast electronic cooling is governed by the intricate interplay of intralayer carrier-carrier and carrier-phonon interactions. As we explain below, the slow electronic cooling at low substrate temperatures is controlled by interlayer Coulombic energy transfer between the LD and HD layers. A summary of the extracted

carrier relaxation times as a function of substrate temperature for a few different pump fluences is presented in Figure 2.3.3(a). We observe that the relaxation times are largely independent of the pump fluence (or the initial electron temperature) except at high substrate temperatures. The slight increase in the relaxation times at the highest pump fluence can be attributed to heating of the HD layers above the substrate temperature, which decreases the rate of the energy transfer from the LD layers. Similarly, the energy transfer between layers becomes less efficient at high substrate temperatures, at which the difference between the electron temperatures in different layers is small. As a consequence, the contribution of the interlayer Coulomb coupling to electronic cooling is diminished at substrate temperatures above ~200 K as evidenced from the fits.

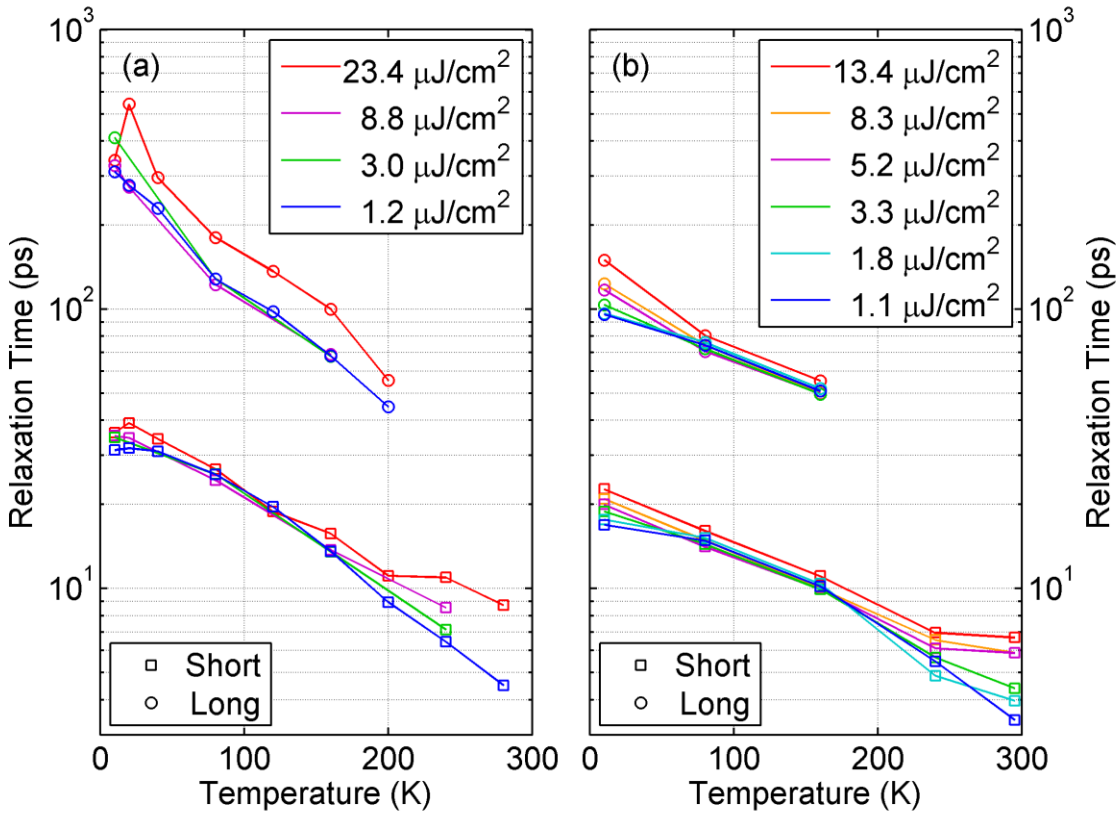

Figure 2.3.3 – Short and long carrier relaxation times as a function of substrate temperature for a few different pump fluences for an MEG sample with (a) ~63 and (b) ~35 layers.

We repeat identical experiments and analysis for a second MEG sample with ~35 layers and the corresponding summary of the extracted carrier relaxation times for the best fits are presented in Figure 2.3.3(b). Qualitatively, the THz carrier dynamics for the 35-

layer sample mirror those for the 63-layer sample by exhibiting a transition from a faster mono-exponential to a slower bi-exponential decay as the substrate temperature is decreased. Similarly, the relaxation times are independent of the pump fluence except at high substrate temperatures. Further inspection shows that the long relaxation times become up to a few times shorter, when the number of epitaxial graphene layers is nearly halved, which indicates the presence of interlayer interaction. We show below that because of the range dependence of the Coulomb scattering processes, the addition of more LD layers slows their collective electronic cooling via coupling to the HD layers.

Section 2.3.3 Ultrafast IR Pump-Probe Spectroscopy

In this section, to further support the existence of interlayer energy transfer in MEG, we devise another experiment using ultrafast degenerate IR pump-probe spectroscopy [23, 24] in which we selectively photoexcite hot electrons in all layers of MEG except the first HD layer nearest to the SiC substrate. We then observe the cooling of these hot electrons via interlayer Coulomb coupling to the cold electrons in the first HD layer. Our laser system consists again of a Ti:Sapphire oscillator and amplifier followed by an optical parametric amplifier (OPA 9850, Coherent) and produces ultrafast optical pulses with a center wavelength tuned to 1.8 μm. The OPA beam is filtered through a 10 nm bandpass filter centered at 1.8 μm and is split into a pump and a probe beams that are both focused on the MEG sample with an intensity spot size diameter of ~50 μm. The transmitted portion of the probe is detected by using a grating spectrometer and an InGaAs photodetector in conjunction with a conventional lock-in amplifier data acquisition technique. The MEG sample is mounted inside a cryostat (ST-100, Janis) and the substrate temperature is held at 10 K. The experimental error is again estimated not to exceed ~5%.

In this experimental approach, both the pump and the probe photon energies ($\hbar\omega \approx$ 690 meV) are chosen to be slightly smaller than twice the Fermi level of the first HD layer ($E_F \approx$ 360 meV), but larger than twice the Fermi levels of all other layers in MEG [23, 24]. Thus, the pump selectively injects hot electrons in all layers of MEG *except* the first HD layer, in which interband absorption is Pauli blocked as illustrated schematically in the inset of Figure 2.3.4. The probe differential transmission due to photoexcitation has a *positive* contribution from the hot electrons in all layers of MEG except the first HD layer.

The first HD layer gives no contribution, when the carriers in that layer remain unexcited. However, interlayer Coulombic energy transfer can heat this layer, which results in a distinct *negative* contribution to the differential transmission.

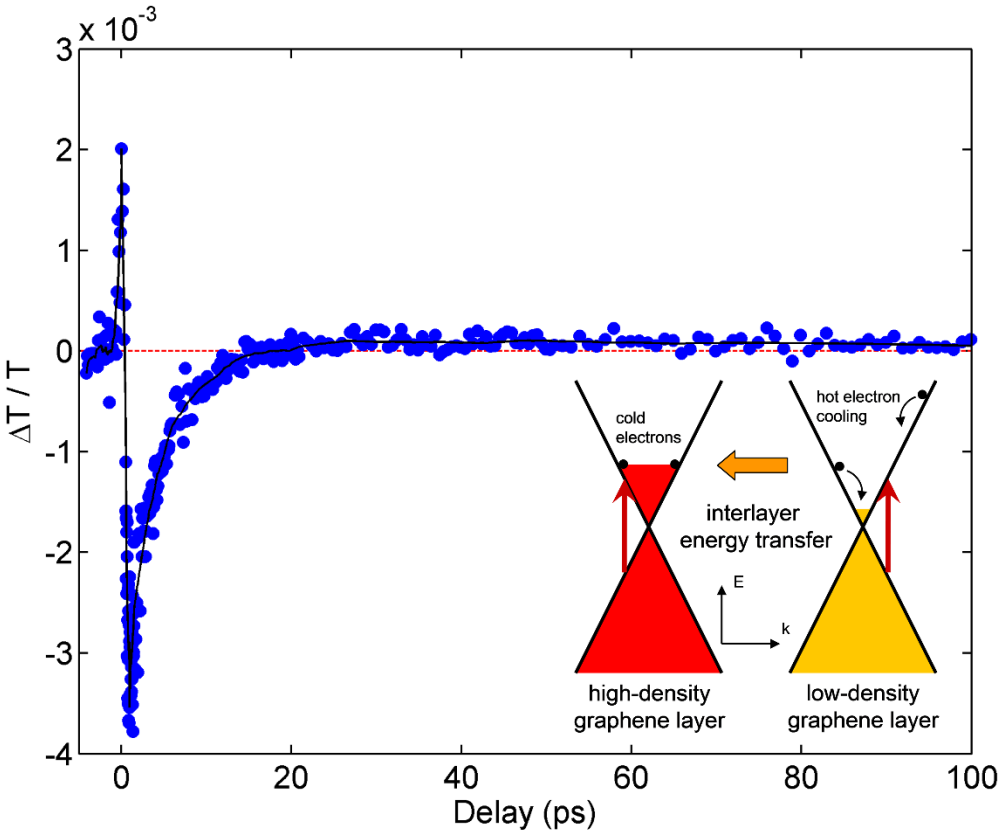

Figure 2.3.4 – Differential transmission in ultrafast degenerate 1.8 μm IR pump-probe spectroscopy at a pump fluence of 80 μJ/cm^2 and a substrate temperature of 10 K for an MEG sample with ~63 layers. (Inset: Schematic diagram of interlayer Coulombic energy transfer from a hot LD to a cold HD layer in MEG. The pump selectively injects hot electrons in all layers of MEG *except* the first HD layer, in which interband absorption is Pauli blocked.)

Figure 2.3.4 shows the probe differential transmission normalized to the probe transmission without photoexcitation, $\Delta T/T$, as a function of pump-probe delay for the MEG sample with ~63 layers. We observe that immediately after photoexcitation the differential transmission is positive, arising from the hot electrons that are directly injected in the top layers. Shortly after that, the differential transmission becomes negative and reaches its minimum value within ~1 ps. This sign change demonstrates the existence of an efficient interlayer energy transfer, in which the cold electrons in the first HD layer act as a heat sink for the hot electrons in the top layers. The rapidly rising electron temperature

in the first HD layer has a dominant negative contribution to the differential transmission. As delay time increases, the electrons in the first HD layer cool down much faster than the electrons in the top layers due to the sharply increasing rate of acoustic phonon emission with carrier density. This results in a second sign change in the differential transmission at ~20 ps, when the electron temperature in the first HD layer approaches the equilibrium lattice temperature. By comparing to the THz carrier dynamics in Figure 2.2.4(b) in Section 2.2, we note that it takes slightly longer for the HD layer to cool down due to the extra heat from the top LD layers. At that point, the optical and acoustic phonon cooling rate in the first HD layer balances the interlayer energy transfer rate from the top layers. Electronic cooling in the top layers of MEG via the interlayer Coulomb coupling survives on a timescale exceeding a hundred picoseconds (limited by the experimental signal-to-noise ratio), which is consistent with that observed in the THz carrier dynamics in Figure 2.3.2.

Section 2.3.4 Interlayer Energy Transfer Theory

In this section, we turn our attention to a detailed presentation of the theory of hot-carrier equilibration based on interlayer energy transfer via screened Coulomb interactions in MEG.

Non-equilibrium electrons in graphene have been shown to thermalize within a layer on an ultrafast timescale on the order of tens of femtoseconds [30, 37, 54]. We assume that this property holds also in MEG, and that it leads to pseudo-equilibrium electronic states with well-defined temperatures T_i in layer i, but we allow for the possibility of differences in temperature between layers that survive to longer timescales. The multilayer temperature dynamics are described by a set of coupled non-linear first order differential equations:

$$\partial_t T_i = \left(Q_i^{ph}(T_i) + \sum_{j\neq i} Q_{ij}^{el}\left(T_i, T_j\right)\right) / C_i, \tag{2.3.2}$$

where $C_i = \partial_T E_i$ is the heat capacity and E_i is the energy density of electrons in the i-th layer. The rate of change of energy density in layer i is determined by the sum of two processes: energy loss to the lattice via electron-phonon scattering at rate Q_i^{ph}, and energy transfer from other layers j to i via interlayer electron-electron scattering at rate Q_{ij}^{el}. Both of these mechanisms depend strongly on the carrier density. The four most highly doped

layers in the 63-layer MEG sample have Fermi energies measured to be 360, 218, 140, and 93 meV, respectively [23, 24]. A simple Thomas-Fermi model [71] is able to account semi-quantitatively for the monotonic decrease in carrier density with separation from the substrate in multilayered graphene systems. Electronic transport and magneto-optical spectroscopy measurements [10, 11] of top LD layers suggest local carrier density fluctuations in these LD layers that satisfy of $n_{LD} \leq 10^{10}$ cm^{-2}.

Recent ultrafast optical spectroscopy experiments [23] have found that hot carriers in the HD layers of MEG quickly relax to the lattice temperature with equilibration times on the order of a few picoseconds. Theoretical calculations neglecting interlayer thermal coupling ($Q_{ij}^{el} \to 0$) have obtained order of magnitude agreement with these measurements [50]. On the other hand, the same approximation applied to LD layers erroneously predicts a thermal equilibration time on the order of several nanoseconds, in disagreement with the experiments reported here. This was the initial impetus for our examination of the Coulombic interlayer energy transfer mechanism. According to Ref. [50] the acoustic phonon cooling power is proportional to the square of the carrier density, n^2. Allowing for disorder-assisted electron-phonon (supercollision) scattering changes this dependence to n [52]. In the HD layers, optical and acoustic phonon emission is likely to provide the dominant cooling pathway for hot carriers [23]. In the LD layers, however, we suggest that it plays a more subsidiary role by keeping the electron temperature in the HD layers pinned to the lattice temperature ($T_{HD} = T_L$), while they act as a Coulomb-coupled heat sink for the LD layers.

Although the true electron density profile across the many layers of MEG is expected to decrease smoothly, it is convenient to make a sharp distinction between highly doped (HD) and lightly doped (LD) layers. We predict that the asymptotic temperature dynamics of LD layers in MEG are effectively governed by Equation 2.3.2 with $Q_{LD}^{ph} \to 0$. In our theoretical analysis, we will denote the four most highly doped layers near the substrate, as HD layers. Quantitatively, this cut-off is suggested from the disorder-free theory of acoustic phonon cooling [50], which implies that the hot-electron distribution in layers $i > 4$ transfers energy via the interlayer Coulomb interaction to the j HD layers ($j < i$) faster than it loses energy to the lattice via acoustic phonon emission. More precisely,

we find that $Q_i^{ph}/\left(\sum_{j<i} Q_{ij}^{el}\right) \leq 1$, for temperatures $T_i \geq 50$ K. In all calculations described below, we use the values $E_{F,1-4}$ = 360, 218, 140, and 93 meV for the Fermi levels of the first four HD layers. These have been measured explicitly for the 63-layer MEG sample and are expected to be good estimates for the 35-layer MEG sample.

The rate of Coulombic energy transfer between two layers is given by a Fermi golden-rule expression:

$$Q_{ij}^{el} = -\frac{2\pi}{\hbar}\sum_{\boldsymbol{k}_i,\boldsymbol{k}_i'}\sum_{\boldsymbol{k}_j,\boldsymbol{k}_j'}\left(\varepsilon_{\boldsymbol{k}_j'} - \varepsilon_{\boldsymbol{k}_j}\right)|W_{int}|^2$$

$$\times\, \delta_{\boldsymbol{k}_i'+\boldsymbol{k}_j',\boldsymbol{k}_i+\boldsymbol{k}_j}\delta\left(\varepsilon_{\boldsymbol{k}_j'} + \varepsilon_{\boldsymbol{k}_i'} - \varepsilon_{\boldsymbol{k}_j} - \varepsilon_{\boldsymbol{k}_i}\right)$$

$$\times\left(f_{\boldsymbol{k}_j}\left(1 - f_{\boldsymbol{k}_j'}\right)f_{\boldsymbol{k}_i}\left(1 - f_{\boldsymbol{k}_i'}\right) - f_{\boldsymbol{k}_j'}\left(1 - f_{\boldsymbol{k}_j}\right)f_{\boldsymbol{k}_i'}\left(1 - f_{\boldsymbol{k}_i}\right)\right), \qquad (2.3.3)$$

where (i, j) are layer indices, and $\boldsymbol{k}$ is a collective index which implies, in addition to wavevector, the spin, the valley, and the band index labels required to specify single electron states in graphene's low-energy Dirac model [72]. As mentioned above, *intra*-layer electron thermalization [30, 37, 54] is much faster than *inter*-layer energy transfer, and this allows us to describe electronic state occupations with a quasi-equilibrium Fermi distribution $f_{\boldsymbol{k}} = f(\varepsilon_{\boldsymbol{k}}, \mu, T)$. In the random phase approximation (RPA):

$$W_{int} = \left(\frac{1+\alpha_i\beta_i e^{i\left(\theta_{\boldsymbol{k}_i-\boldsymbol{q}}-\theta_{\boldsymbol{k}_i}\right)}}{2}\right)\left(\frac{1+\alpha_j\beta_j e^{i\left(\theta_{\boldsymbol{k}_j+\boldsymbol{q}}-\theta_{\boldsymbol{k}_j}\right)}}{2}\right)\times v_{ij}^{sc}(q,\omega)\delta_{\sigma_i,\sigma_i'}\delta_{\sigma_j,\sigma_j'}\delta_{\tau_i,\tau_i'}\delta_{\tau_j,\tau_j'}, \qquad (2.3.4)$$

where $q = \left|\boldsymbol{k}_j' - \boldsymbol{k}_j\right|$, $\epsilon = \varepsilon_{\boldsymbol{k}_j'} - \varepsilon_{\boldsymbol{k}_j}$, and $v_{ij}^{sc}(q,\epsilon)$ is the screened electron-electron interaction between layers i and j (see below). When screening is neglected, $v_{ij}^{sc}(q,\epsilon) \rightarrow v_{ij}(q) = 2\pi e^2 exp\left(-qd_{ij}\right)/\kappa q$ is the two-dimensional Fourier transform of the bare Coulomb interaction between two electrons with interlayer separation d_{ij} and $\kappa = 5.5$ to account for the presence of MEG at the surface of the SiC substrate. The factors in parenthesis are the well-known form factors that account for the sub-lattice spinor dependence of graphene π-band plane-wave matrix elements. The indices α and β are

equal to 1 and -1 for conduction and valence band states, respectively. The Kronecker delta's in Equation 2.3.4 explicitly exhibit the property that continuum model interactions are independent of spin (σ) and valley (τ). Using Equation 2.3.4 and comparing with the expression for graphene's non-interacting density-density response function, $\chi(q,\omega,T)$, we finally obtain the following compact expression which is suitable for numerical evaluation:

$$Q_{ij}^{el} = \frac{\hbar}{\pi}\int_{-\infty}^{\infty} d\omega\, \omega \sum_q \left|v_{ij}^{sc}\right|^2 \times \left[n_B(\hbar\omega/T_i) - n_B\left(\hbar\omega/T_j\right)\right]$$

$$\times\, Im(\chi_i(q,\omega,T_i))Im\left(\chi_j(q,\omega,T_j)\right), \qquad (2.3.5)$$

where $n_B(x) = 1/(exp(x) - 1)$ and $k_B = 1$ throughout. We use this expression below to calculate interlayer energy transfer rates. A central quantity in the theoretical formulation of the many-body effects of Dirac fermions is the dynamical polarizability tensor $\chi_i(q,\omega,T_i)$ for the i-th layer at temperature T_i. This is defined through the one-body non-interacting Green's functions [73]. The density-density response function of the doped two-dimensional Dirac electron model was first considered by Shung [74] at zero-temperature as a step toward a theory of collective excitations in graphite. The Dirac electron $\chi_i(q,\omega,T_i)$ expression at finite temperature has been recently considered [75, 76, 77]. Before proceeding with the rate calculations, however, we must first discuss the approximation we use for the screened interlayer Coulomb interaction.

In the RPA, the bare interlayer Coulomb interaction is screened [78] by the potential produced by self-consistently readjusted charge density. For a general multilayer system this implies that [79]:

$$\boldsymbol{v}_{ij}^{sc} = \left(\boldsymbol{v}^{-1} - \delta_{ij}\chi_i(q,\omega,T_i)\right)_{ij}^{-1}, \qquad (2.3.6)$$

where $\boldsymbol{v}$ and $\boldsymbol{v}^{sc}$ are matrices which describe bare and screened potentials in one layer (i) to an external charge in another layer (j). Screening complicates energy cooling dynamics, because it causes the energy transfer rate between a particular pair of layers to depend, through $\chi(q,\omega,T)$, on the temperatures in all layers. However, the low carrier densities in the layers far from the substrate [10, 11] motivate a simplifying approximation in which their contributions to screening are neglected. By comparing this approximation with the

full expression, we find that this simplification is justified in the regions of phase space (q, ω) important for low temperature energy transfer.

The relative ability of intraband excitations in LD and HD layers to screen the interaction can be established by examining the ratios of their density response functions in the static limit: $\chi_{HD}(q)/\chi_{LD}(q) = \sqrt{n_{HD}/n_{LD}}$. In our MEG samples this ratio varies from ~8-31 in the important regions, and suggests that the leading order charge polarization responsible for screening the MEG interlayer Coulomb interaction can be approximated without including the contribution from the LD layers. We note that the Bose factors in Equation 2.3.5 limit transfer energies to $\hbar\omega \leq k_B T$. We also note that the factor $exp(-qd_{ij})$ in the interlayer Coulomb interaction limits the important wavevector transfers to $q < 1/d_{ij}$. The conditions (setting $\hbar$ and $k_B \rightarrow 1$):

$$q \leq 1/d_{ij} \qquad \omega \leq T, \tag{2.3.7}$$

apply equally well to Coulomb-mediated interlayer energy and momentum transfer in any type of multilayer two-dimensional electron system.

Setting $\chi_j(q, \omega, T_j)$ to zero for all but the four HD layers nearest the substrate, and letting the separation distance between the four HD layers also go to zero (relative to the generally much larger spacing between HD and LD layers in MEG), we obtain the following approximate expression:

$$v_{ij}^{sc}(q, \omega) \rightarrow v_{ij}(q)/\epsilon^{MEG}(q, \omega), \tag{2.3.8}$$

where

$$\epsilon^{MEG}(q, \omega) = 1 - \frac{2\pi e^2}{\kappa q} \sum_{j \in HD} \chi_j(q, \omega, T_j). \tag{2.3.9}$$

In the calculations reported on below j was summed over the four HD layers.

Although Coulomb-coupling between LD layers is very strong [80], by temporarily forcing $Q_{LD,LD'}^{el} \rightarrow 0$ we can gain insight into the distance dependence of the energy transfer rate. The temperature dynamics of each individual LD layer coupled to the HD layers are then independent and obey:

$$\partial_t T_{LD} = \left(\sum_{j\in HD} Q^{el}_{LD,j}\left(T_{HD} = T_L, T_{LD}, d_{LD,j}\right)\right) / C_{LD}. \qquad (2.3.10)$$

If we also approximate the heat capacity in the LD layers by the neutral graphene formula $C_{LD} = 18\zeta(3)T_{LD}^2/(\pi v_F^2)$, we obtain the results shown in Figure 2.3.5(a) and (b), where we have used this formula to evaluate $T_{LD}(t)$ for several different values of $d_{HD,LD}$. All of these curves are calculated for the typical carrier density of the LD layers in MEG, measured in experiment, of n_{LD} = 10^{10} cm^{-2}. The slowest ($d_{HD,LD}$ = 60 layers) and fastest ($d_{HD,LD}$ = 1 layer) temperature relaxation curves provide upper and lower bounds, respectively, on the true relaxation time of *all* LD layers, when energy transfer between pairs of LD layers is no longer neglected, i.e. $Q^{el}_{LD,LD'} \neq 0$.

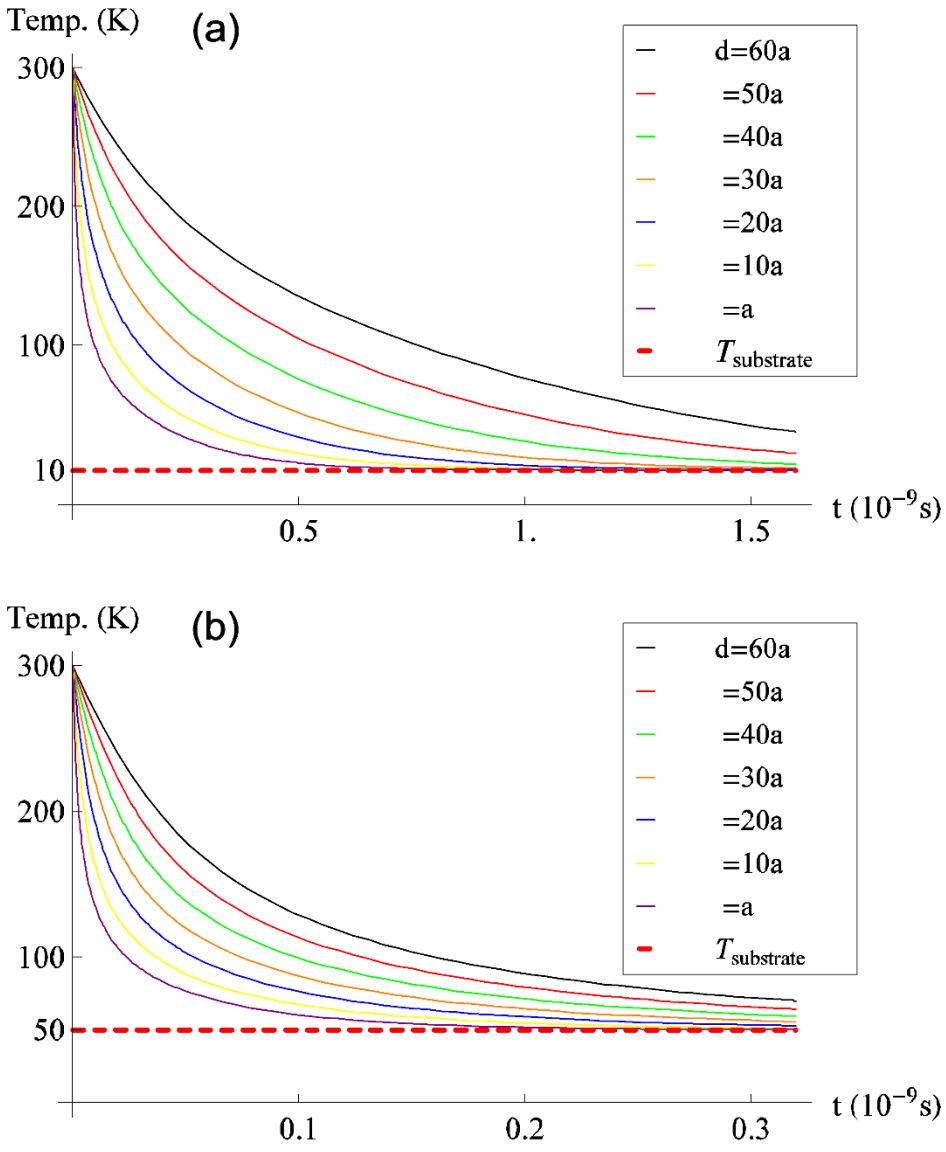

Figure 2.3.5 – Carrier temperature dynamics of a single LD layer in MEG, resulting from cooling via interlayer Coulombic energy transfer to the HD layers near the SiC substrate, when energy transfer between all LD layers is ignored, at a substrate temperature of (a) 10 K and (b) 50 K for a few different HD-LD layer separations.

Since cooling powers between LD layers are typically 1 to 2 orders of magnitude larger than between LD and HD layers ($Q^{el}_{LD,LD'} \gg Q^{el}_{LD,HD}$) [80], energy transfer between pairs of LD layers cannot be ignored in the calculations. Poles in the screened interaction described by Equation 2.3.6 at plasmon frequencies greatly enhance the interlayer quasi-particle scattering rate. This effect does not contribute to energy transfer between HD and

LD layers, because the plasmon modes then lie at higher frequencies than can be excited in low temperature HD layers; the plasmon poles reside above the *intra*-band particle-hole continuum of HD layers, i.e. $\omega_{pl}(q) > v_F q$. However, at temperatures comparable to the Fermi temperature, *inter*-band particle-hole excitations are no longer Pauli blocked at any frequency, and these excitations can take advantage of the plasmon poles in the screened interaction [81, 82]. It is the small Fermi temperatures ($T_F \propto \sqrt{n}$) of the LD layers that dramatically increases the Coulomb-coupling amongst the group of LD layers.

As LD layers closer to the substrate cool, they absorb energy from and cool more distant LD layers. This effect results in a *collective cooling* state in which the electron temperatures of all the LD layers relax to the equilibrium lattice temperature nearly uniformly, and motivates an approximation with a single collective LD layer temperature, $T_c(t)$. In employing this approximation our goal is to establish that Coulomb scattering is a relevant energy transfer process up to quite high temperatures. A more detailed calculation in which the temperature of each low density layer is allowed to vary independently would be warranted if the charge density profile in the multilayer system was accurately known. Such a calculation might in any event not achieve greater accuracy since the calculations of electron-electron scattering amplitudes can only be performed approximately. The collective cooling state model we employ has the advantage that it requires fewer computationally burdensome finite-temperature dynamic polarizability calculations. The collective cooling dynamics model of the collective temperature is given by:

$$\partial_t T_c = \left(\sum_{i\in LD}\sum_{j\in HD} Q_{ij}^{el}\left(T_{HD} = T_L, T_{LD} \to T_c, d_{ij}\right)\right) / NC_{LD}, \qquad (2.3.11)$$

where N is the total number of LD layers. We have summed over the energy transfer rate between all LD-HD pairs of layers, appealing to strong electron-phonon coupling to keep the HD layer temperature at T_L and to strong $Q_{LD,LD}^{el}$, to keep the LD layers at a common temperature $T_c(t)$. Figure 2.3.6(a) and (b) compare the calculated collective thermal relaxation dynamics $T_c(t)$ in 30-layer and 60-layer MEG samples for lattice temperature of 10 K and 50 K, respectively. For both lattice temperatures, thicker MEG samples cool more slowly. This trend can be understood by noting that each additional LD layer

contributes an equal amount to the combined LD layer heat capacity, whereas the energy transfer rate to the HD layers falls off upon moving further away from the substrate (see Figure 2.3.5(a) and (b)).

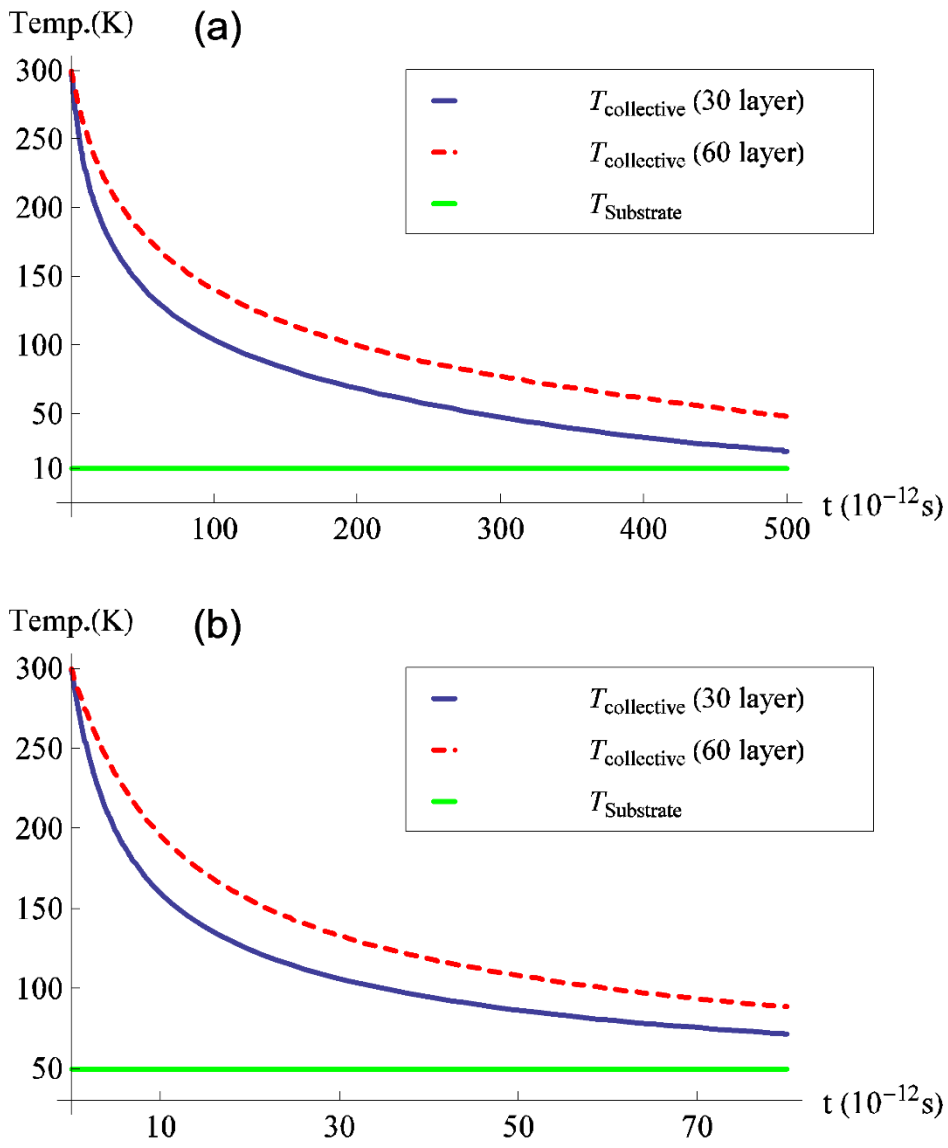

Figure 2.3.6 – Collective carrier temperature dynamics of the LD layers in MEG with 30 and 60 layers, resulting from cooling via interlayer Coulombic energy transfer to the HD layers near the SiC substrate, at a substrate temperature of (a) 10 K and (b) 50 K.

If we linearize the collective temperature of the LD layers about the equilibrium lattice temperature, $\delta T \equiv T_c(t) - T_L$, we find that the interlayer energy transfer rate can be written as:

$$Q_{ij}^{el} = \frac{\hbar}{\pi}\int_{-\infty}^{\infty} d\omega\ \omega \sum_q \left|v_{ij}^{sc}\right|^2 \times \frac{\hbar\omega}{4T_L^2} \times \frac{\delta T}{\sinh^2(\hbar\omega/2T_L)}$$

$$\times\, Im(\chi_i(q,\omega,T_L))Im\big(\chi_j(q,\omega,T_L)\big). \qquad (2.3.12)$$

This equation can be used to define collective electronic cooling times, which are easier to compare to the experimental carrier relaxation times extracted from the phenomenological fits. Figure 2.3.7 compares the theoretical and the experimental relaxation times over a lattice temperature range of T_L = 10-160 K. From this figure we see that, within our approximations, the theory reproduces the experimental trends versus both the lattice temperature and the number of epitaxial graphene layers; more specifically, both relaxation times increase with decreasing the lattice temperature and increasing the number of layers. We note that since our theoretical relaxation times are obtained by linearizing the interlayer energy transfer rate equations, they underestimate interlayer coupling except when $T_{LD} - T_{HD} \ll T_{HD}$. Thus, we expect (and observe) the theoretical relaxation times to be longer than those obtained by fitting the experimental data over a broader temperature range.

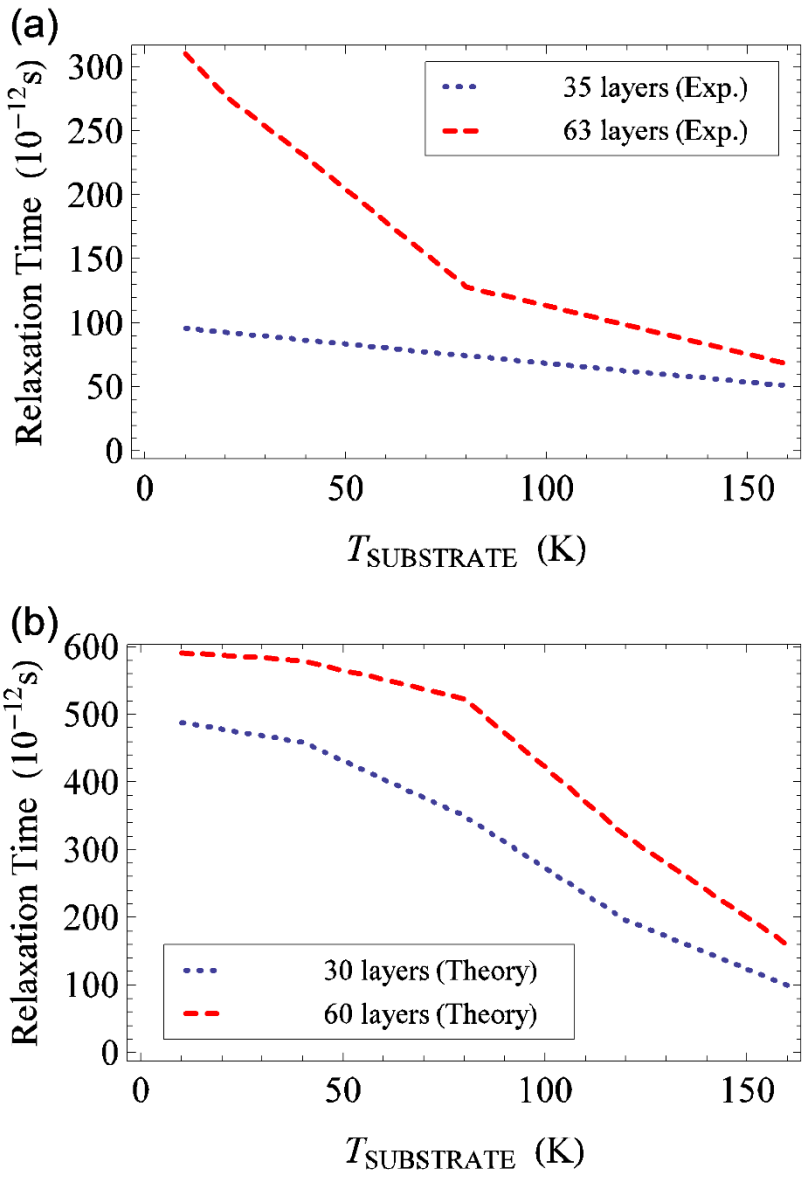

Figure 2.3.7 – (a) Experimental long carrier relaxation times as a function of substrate temperature for MEG samples with ~63 and ~35 layers. (b) Theoretical carrier relaxation times as a function of substrate temperature for MEG samples with 60 and 30 layers.

We can identify the microscopic origins of the relaxation times' dependence on lattice temperature using an analytic formula for the Coulombic energy transfer rate between a single LD layer and a single HD layer in MEG. Here, we show only the result of summing over the rates between all HD-LD pairs of layers. In the multilayer case, we obtain the following net energy loss rate (per area) for N LD layers in MEG:

$$\frac{1}{L^2} \times Q^{el}_{HD,LD} = \gamma(T_{LD} - T_{HD}) \left(\frac{N\nu_{LD}}{\sum_j \nu_{HD}}\right) T^3_{HD} ln\left(\frac{T_{F,LD}}{T_{HD}}\right), \quad (2.3.13)$$

where $\gamma = (8\pi^2/30)(k_B^4/\hbar^3 v_F^2)$ and the density of states in the HD and LD layers are denoted by ν_{HD} and ν_{LD}. The sum over index j runs over all HD layers in the MEG sample. We find that the Coulombic energy transfer rate exhibits a temperature dependence of $T^3 ln(T)$ [83]. This result is related to the familiar result [78] for electron-electron scattering rates τ^{-1} in Fermi liquids which are proportional to $T^2 ln(T)$. These power laws appear, because the Fermi distribution limits the initial-final state pair energies which can partake in scattering to an energy window of width $\hbar\omega \sim k_B T$ about the Fermi energy, which qualitatively explains the additional factor of T; the additional factor of T appears, because scattering events are weighted by the transferred energy in the cooling power case. On the other hand, the heat capacity of nearly neutral graphene increases linearly with T (or as T^2 if $T \ll T_F$). The final result is that the electronic cooling time defined above becomes shorter with increasing lattice temperature, consistent with the experimental trends as shown in Figure 2.3.7. Precise agreement is not expected outside of the degenerate temperature regime ($T_L \ll T_{F,LD}$ ~ 135 K), within which Equation 2.3.13 becomes exact.

Section 2.4 Buckled Epitaxial Graphene

In this section, we discuss the dynamic THz response of buckled epitaxial graphene. This special form of graphene is grown epitaxially on nitrogen-seeded single-crystal silicon carbide (SiC$(000\bar{1})$) substrates by thermal decomposition of Si atoms. The pre-deposited interfacial nitrogen atoms pin the first graphene layer to the SiC substrate and cause it and subsequent graphene layers to buckle into nanoscale folds, which opens an energy bandgap of up to ~0.7 eV. We observe a remarkable increase of up to two orders of magnitude in the decay of the THz carrier dynamics in this semiconducting form of epitaxial graphene relative to pristine epitaxial graphene, which we attribute to a relaxation of the phase space constraints near the Dirac point accompanied with a large enhancement of the optical-phonon-mediated carrier cooling due to the finite bandgap. Our results suggest that the introduced bandgap is spatially non-homogenous, with local values below the optical phonon energy of ~200 meV, which allows the conduction and the valence band to be bridged by optical phonon emission. We also demonstrate that carrier relaxation times can

be modified by orders of magnitude by careful bandgap engineering, which could find application in novel graphene-based devices that incorporate both metallic and semiconducting forms of graphene.

Since its successful isolation, graphene has been considered by many as a likely candidate to succeed silicon as the channel material in electronics [84, 85, 86]. Graphene boasts remarkable electronic and optical properties including incredibly high electron mobility, excellent thermal conductivity, and strong intraband and interband optical absorption, but the lack of an energy bandgap has long presented itself as possibly the largest challenge for the rapid development of graphene-based electronics and optoelectronics. A sizable and well-defined bandgap is essential for the realization of practical graphene-based devices such as field-effect transistors, photodetectors, solar cells and saturable absorbers. To overcome this deficiency, a range of techniques have been proposed and/or demonstrated to engineer a bandgap in graphene including electrostatic gating [87], substrate interaction [22], chemical functionalization [88, 89], electron confinement in nanostructures [90, 91], and strain engineering [92].

Pristine epitaxial graphene (EG), grown on the C-face or Si-face of single-crystal silicon carbide (SiC$(000\bar{1})$) substrates by thermal decomposition of Si atoms, has been extensively characterized and shown to possess electronic structure and properties approaching an idealized disorder-free graphene down to within a few meV of the Dirac point [10, 11]. Consequently, EG shares the drawback of an ideal graphene that it is a gapless semi-metal. Recently, a wide bandgap semiconducting epitaxial graphene with very high quality from nitrogen-seeded SiC has been demonstrated over a large area [92]. In this approach, the first graphene layer grows bound to pre-deposited interfacial nitrogen atoms causing it to buckle into folds with ~1-2 nm radii of curvature. Even though the nitrogen remains at the SiC interface, the multilayer epitaxial graphene grown on this surface remains buckled as illustrated schematically in Figure 2.4.1(a) [92]. Buckled epitaxial graphene (BEG) grown this way has a bandgap of up to ~0.7 eV as determined from high resolution angle-resolved photoemission spectroscopy (ARPES) measurements. Figure 2.4.1(b) and (c) [92] show representative ARPES scans on two BEG samples with ~3 and ~8 layers, which have estimated average bandgaps of ~0.7 and ~0.45 eV,

respectively. While the origin of the bandgap is not well understood, it is thought to be associated with either a quasi-periodic strain or electron localization in the highly buckled topography.

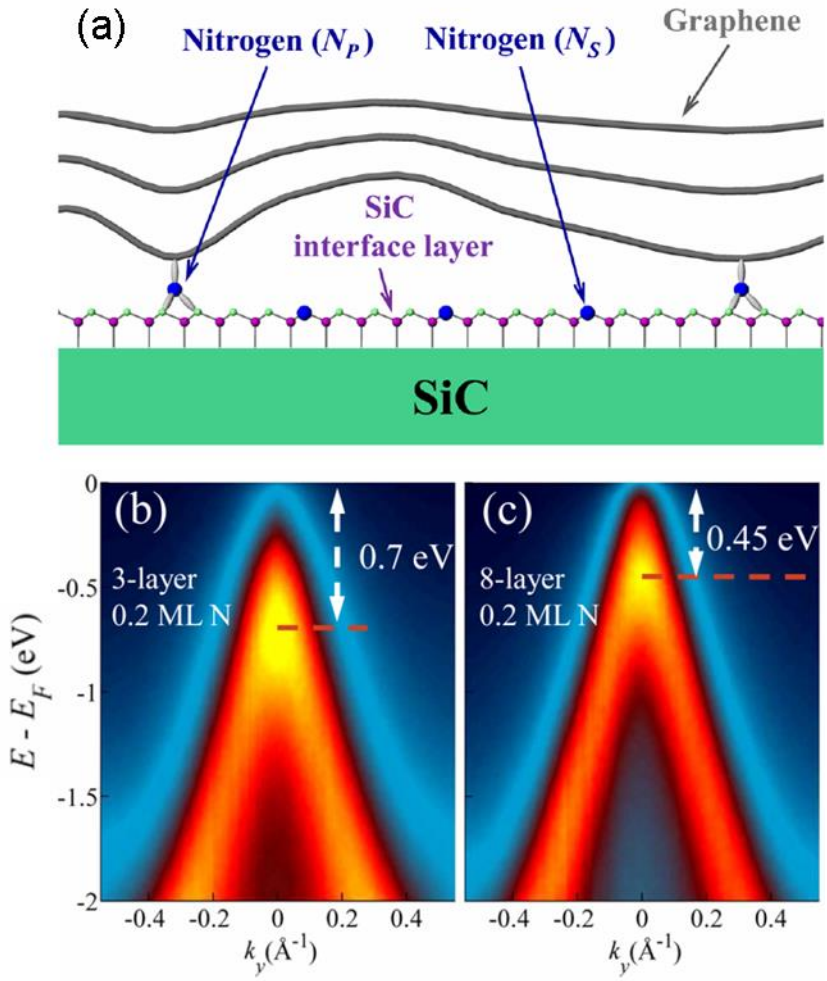

Figure 2.4.1 – (a) Schematic diagram of BEG on nitrogen-seeded SiC. High-resolution angle-resolved photoemission spectroscopy (ARPES) measurement of BEG with (b) ~3 and (c) ~8 layers. (Adapted from Ref. [92].)

In this section, we investigate how the introduced bandgap modifies the hot-carrier relaxation and cooling dynamics of BEG using ultrafast time-resolved THz spectroscopy. Surprisingly, we discover that the THz carrier dynamics of BEG speeds up by over two orders of magnitude relative to pristine EG. We attribute this large difference to be due to the finite bandgap. In this model, the separation of photoexcited electrons in the conduction band and holes in the valence band strongly enhances carrier cooling and recombination via optical phonon emission due to the relaxation of the phase space constraints near the

Dirac point. Our conclusions are consistent with the experimental results and the microscopic theory calculations on the wide variety of graphene samples, including epitaxial and chemical-vapor-deposited (CVD), which we discussed in Section 2.2. Furthermore, these observations suggest that the bandgap introduced in BEG is spatially non-homogenous across a layer likely due to varying levels of strain or electron localization in the buckled folds, and at some locations it is lower than the optical phonon energy of ~200 meV that allows the conduction and valence bands to be bridged by optical phonon emission. Here, we assume that there are no large distortions of the graphene band structure far from the Dirac point in BEG, which is strongly supported by ARPES measurements. Our results have implications not only for gaining physical insight into the hot-carrier relaxation and cooling dynamics of gapped graphene, but also for the design of graphene-based devices and for the manipulation of carrier relaxation times that set limits on the device operating speed. We envisage that the carrier relaxation times can be switched by orders of magnitude by properly engineering the size of the graphene bandgap. This can be potentially utilized in the development of novel graphene-based devices which incorporate both metallic and semiconducting graphene films with various bandgaps.

The BEG samples studied here are prepared following the fabrication process described in detail in Ref. [92]. First, nitrogen is pre-deposited onto the C-face of single-crystal SiC($000\bar{1}$) substrates. After that, graphene is grown epitaxially on the nitrogen-seeded SiC by thermal decomposition of Si atoms. The graphene attaches to interfacial nitrogen atoms causing the first graphene layer and all the layers above it to buckle into folds with ~1-2 nm radii of curvature. The BEG has a bandgap that is due to either a quasi-periodic strain or electron localization. The buckling amplitude decreases in BEG layers farther away from the SiC interface, which relieves the strain and reduces the bandgap size as confirmed by high resolution ARPES measurements (see Figure 2.4.1). The buckled topography of the otherwise continuous graphene film also modifies the interaction with the underlying SiC substrate, which causes all BEG layers to have quasi-neutral doping density. In this work, we prepared two BEG samples with ~8 and ~4 layers and with estimated average bandgaps of ~0.45 and ~0.65 eV, respectively.

A simple physical model governing the hot-carrier dynamics following photoexcitation in BEG is illustrated schematically in Figure 2.4.2(a). The buckling of the otherwise continuous graphene film introduces a finite bandgap whose size decreases with layer number as the curvature of the ripples flattens and the strain is relieved. In addition, it modifies the interaction with the underlying SiC substrate, which results in a very low doping density in all BEG layers, so that the Fermi level lies within the bandgap (step I). Initially, the optical pump injects hot nonequillibrium electrons and holes in the conduction and the valence band, respectively (step II). It is well established that in pristine graphene and graphite, exceptionally efficient intraband and interband carrier-carrier scattering leads to ultrafast hot-carrier relaxation and thermalization within a few tens of femtoseconds [30, 37, 54]. We assume that the same holds true in BEG, which is supported by ARPES measurements that show little distortion of the linear band structure far from the band edges [92]. Unlike pristine graphene, however, the finite bandgap in BEG prevents (or slows down) the merging of the electron and the hole quasi-Fermi levels similar to a semiconductor (step III). For bandgaps close to the optical phonon energy of ~200 meV, this leads to a strong enhancement of the available phase space for optical phonon emission that efficiently bridges the nonequillibrium electron and hole populations as further explained below. Figure 2.4.2(b) illustrates these processes in pristine undoped graphene as a comparison. Here, scattering with optical and acoustic phonons is strongly suppressed due to the vanishing density of states near the Dirac point as we discussed in Section 2.2.

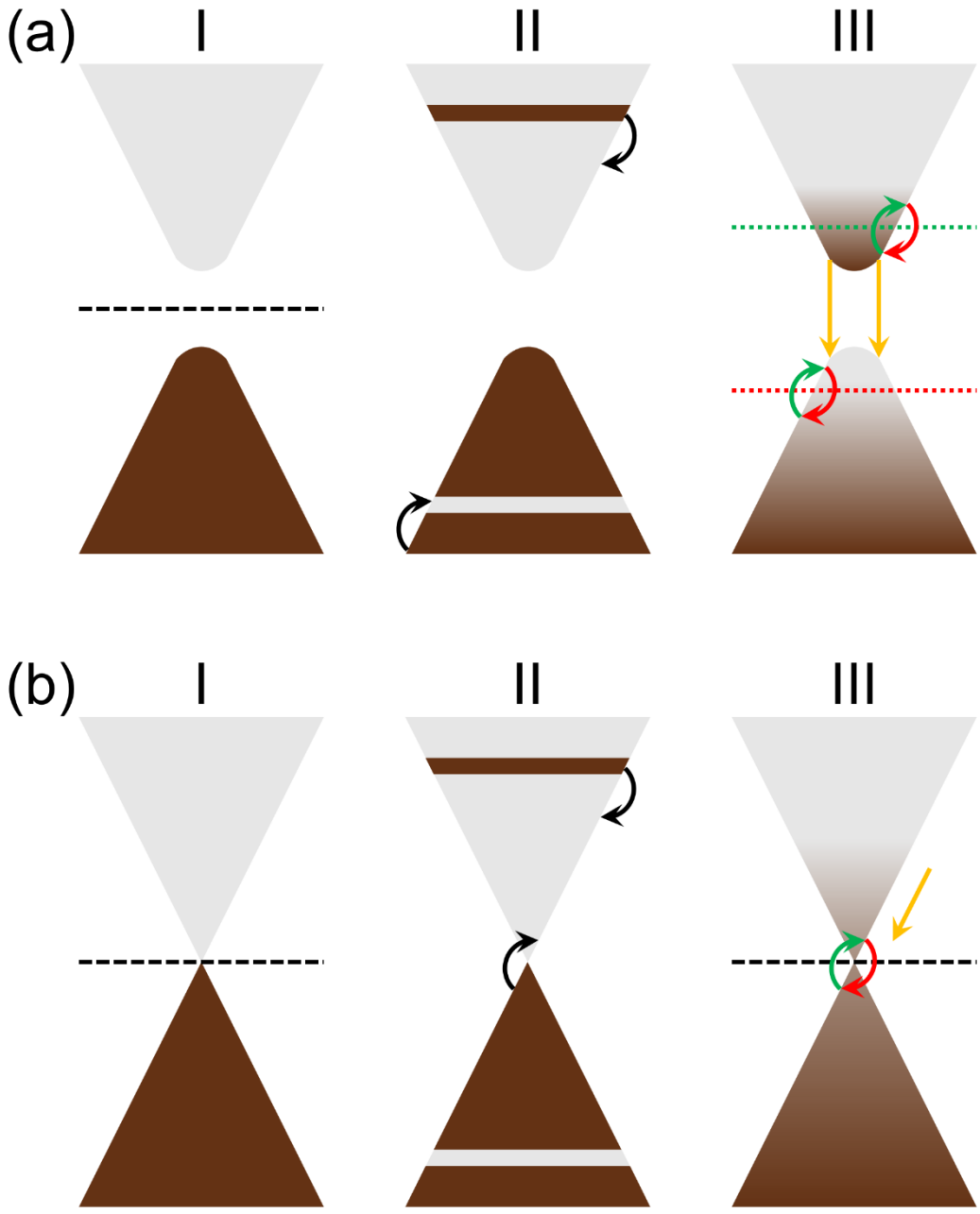

Figure 2.4.2 – Hot-carrier relaxation and cooling dynamics following ultrafast photoexcitation in (a) undoped BEG and (b) undoped pristine graphene.

We perform ultrafast time-resolved THz spectroscopy measurements on BEG to test our physical picture. In doing so, it is instructive to draw a comparison with the previous experimental and theoretical results on pristine EG in Sections 2.2 and 2.3. Figure 2.4.3 shows the differential THz transmission at the peak of the THz probe pulse

normalized to the THz transmission without photoexcitation, $\Delta t/t$, as a function of pump-probe delay, recorded at a substrate temperature of 300 K for variable pump fluence (corresponding to different initial carrier temperature) for the BEG sample with ~8 layers. There are two important observations that can be drawn from Figure 2.4.3. First, we note that the differential THz transmission is negative that corresponds to a pump-induced decrease of the THz transmission or equivalently an increase of the THz absorption. This is consistent with similar experiments on lightly doped EG. In both lightly doped EG and BEG the optical pump injects hot carriers that enhance the THz absorption. Second, we observe that the THz carrier dynamics in BEG relaxes on the order of a few picoseconds. This is about one order of magnitude faster than in lightly doped EG, in which the THz carrier dynamics relaxes on the order of a few tens of picoseconds under identical experimental conditions. This strong enhancement in the decay of the THz carrier dynamics can be explained by the opening of a finite bandgap in BEG that relaxes the phase space constraints near the Dirac point for carrier cooling and recombination via optical phonon emission.

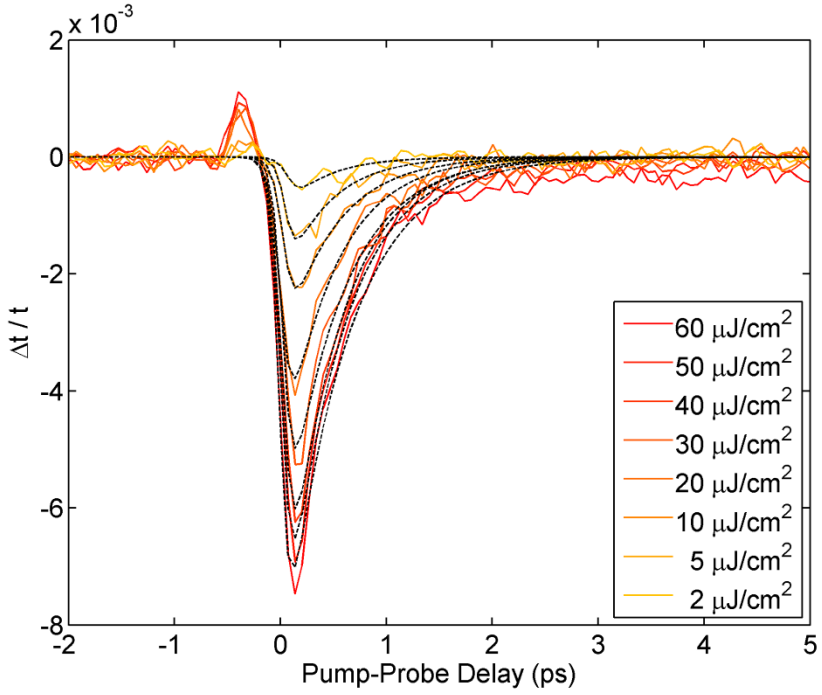

Figure 2.4.3 – Differential THz transmission at a substrate temperature of 300 K for a few different pump fluences for a BEG sample with ~8 layers.

To obtain quantitative estimates of the THz carrier dynamics of BEG, we perform phenomenological fits to the data in Figure 2.4.3 and discover that the differential THz transmission follows closely a mono-exponential relaxation form. A summary of the extracted carrier relaxation times as a function of pump fluence at a substrate temperature of 300 K for the two BEG samples with ~8 and ~4 layers is presented in Figure 2.4.4(a). The relaxation times of BEG are in the range of ~0.3-0.6 ps, which is again about one order of magnitude shorter than these of lightly doped EG, which are in the range of ~4-7 ps under identical experimental conditions. In addition, we observe that the relaxation times of BEG decrease with decreasing the number of layers. Since the average bandgap decreases with layer number, the decreasing relaxation time is consistent with a larger fraction of the hot carriers emitting an optical phonon.

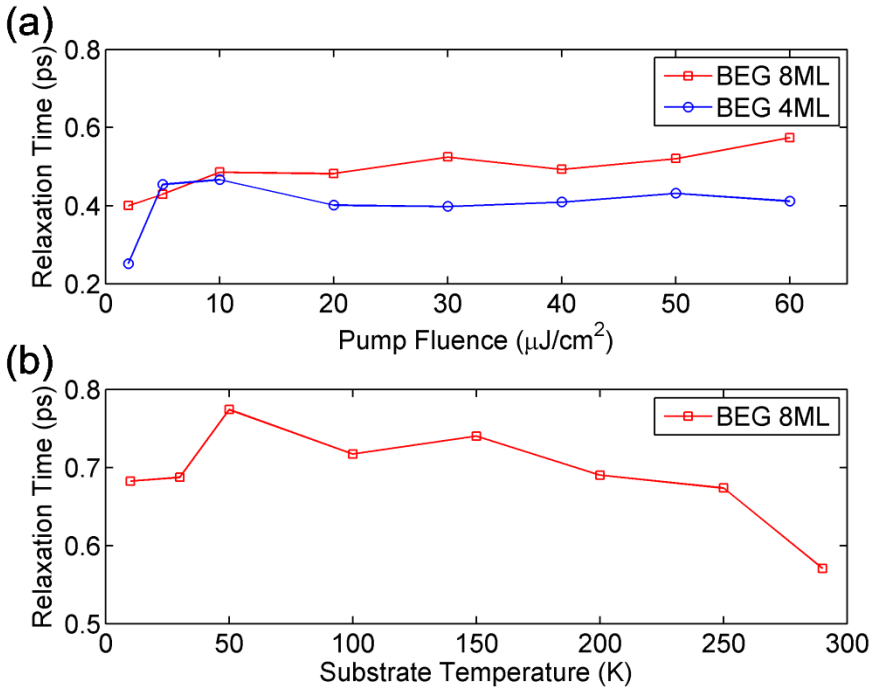

Figure 2.4.4 – Carrier relaxation times as a function of (a) pump fluence at a substrate temperature of 300 K and (b) substrate temperature at a pump fluence of 60.0 μJ/cm^2 for BEG samples with ~8 and ~4 layers.

To further underscore the profound influence of the finite bandgap on the THz carrier dynamics of BEG, we repeat the ultrafast time-resolved THz spectroscopy measurements by varying the substrate temperature. Figure 2.4.4(b) shows the extracted carrier relaxation times as a function of substrate temperature at a pump fluence of 60

$\mu J/cm^2$ for the BEG sample with ~8 layers. We note that the relaxation times of BEG remain completely independent of the substrate temperature around ~0.7 ± 0.05 ps, which is consistent with carrier cooling and recombination via optical phonon emission. In very sharp contrast, the relaxation times of lightly doped EG are strongly dependent on the substrate temperature and extend up to a few hundreds of picoseconds at cryogenic temperatures due to the severe phase space restrictions for carrier scattering near the Dirac point. The introduced bandgap in BEG relaxes these constraints, which allows for very efficient optical phonon emission and speeds up the THz carrier dynamics by over two orders of magnitude at cryogenic temperatures relative to pristine lightly doped EG. It is also worth mentioning that the fast and temperature-independent THz carrier dynamics in BEG resembles qualitatively the similarly fast and temperature-independent THz carrier dynamics in highly doped epitaxial and CVD graphene, which is governed by the coupling of extremely efficient carrier-carrier scattering (arising from the large phase space far from the Dirac point) and optical phonon emission. Rigorous first-principles microscopic theory of the full carrier and phonon dynamics in the BEG system that accounts quantitatively for the experimental results is beyond our scope here.

The fact that the opening of a finite bandgap in graphene dramatically speeds up the hot-carrier relaxation and cooling dynamics following photoexcitation is somewhat surprising, especially since the estimated average value of the bandgap, based on ARPES measurements, is larger than the optical phonon energy of ~200 meV for the studied BEG samples. In addition, the THz carrier dynamics becomes faster as the number of BEG layers is decreased or the average bandgap over all layers is increased. These observations strongly suggest that the bandgap is spatially non-homogenous across a layer likely due to varying levels of strain or electron localization in the buckled folds. Locations with flatter curvature and hence lower levels of strain or electron localization lead to the opening of smaller local bandgaps. We propose that the photoexcited electrons and holes recombine via the emission of optical phonons precisely at these places, where the energy gap is lower than the optical phonon energy of ~200 meV. We estimate that for buckled ripples with a separation of ~4 nm and an effective carrier velocity of ~0.8×10^6 m/s [92], the ballistic carrier transport time is only ~5 fs, which is much shorter than the carrier thermalization time of a few tens of femtoseconds [30, 37, 54]. Thus, the THz carrier dynamics in BEG is

the result of the intricate interplay between extremely efficient carrier-carrier scattering, which continuously rethermalizes the electron and the hole distribution in the conduction and the valence band, respectively, and optical phonon emission, which removes the deposited energy from the electron liquid. In principle, the emission of multiple optical phonons can act as a parallel carrier recombination channel, but we expect that its contribution is negligible on the sub-picosecond timescale observed for our BEG samples.

Another possible pathway for carrier recombination in BEG is via mid-gap defect states. Although carrier trapping due to disorder cannot be completely ruled out, it is not supported by either the scanning tunneling microscopy (STM), the angle-resolved photoemission spectroscopy (ARPES) or the ultrafast time-resolved THz spectroscopy measurements performed on a number of BEG samples [92]. The THz carrier dynamics recovers mono-exponentially to its pre-photoexcitation level and no long-lived component is visible within the experimental signal-to-noise ratio, which could be potentially attributed to slow carrier trapping by defect states. Using the graphene interband optical absorption of ~2.3% per layer, we estimate that ~6×10^{12} cm^{-2} electron-hole pairs are initially injected at the highest pump fluence of 60 $\mu J/cm^2$. This sets an unrealistically high lower bound to the density of defect states in our high quality continuous BEG. Consequently, we expect that carrier trapping due to disorder is not the dominant carrier recombination mechanism.

Section 2.5 Epitaxial Graphene Nanoribbons

In this section, we discuss the dynamic THz response of epitaxial graphene nanoribbons, in which quantum confinement effects become prominent.

In Section 2.1, we mentioned that graphene can be considered a 2D member of a larger carbon family. When graphene is sliced into very narrow nanoscale strips or ribbons, the electron wavefunction is confined in one more dimension. Hence, graphene nanoribbons can be considered a 1D member of the carbon family. Graphene nanoribbons are very similar to carbon nanotubes and they share many common characteristics. The additional degree of quantum confinement modifies the band structure of pristine graphene and results in the formation of high energy subbands, but the precise details are different for different types of edges. Depending on the type of their edges, graphene nanoribbons

can be broadly classified as zigzag, armchair and chiral (a mixture of zigzag and armchair). The band structure of graphene nanoribbons has been theoretically calculated for different edge terminations including zigzag and armchair [93, 94, 95, 96, 97, 98]. Graphene nanoribbons with zigzag edges always have an edge state at zero energy, and hence are metallic. Graphene nanoribbons with armchair edges can either have intersecting metallic bands and be metallic or have an energy gap and be semiconducting, when their width equals to an odd or even number of carbon atoms, respectively.

The epitaxial graphene nanoribbon (EGNR) samples studied here are prepared following the fabrication process described in detail in Ref. [99]. The process consists of three main steps as illustrated schematically in Figure 2.5.1(a) [99]. First, abrupt steps are etched in the Si-face of single-crystal SiC$(000\bar{1})$ substrates by photolithographic definition of nickel lines, which are transferred by a fluorine-based reactive ion etch (RIE). The RIE process allows for nanometer precision in the etch depth, which ultimately defines the width of the EGNRs. Second, the nickel masks are removed and the patterned SiC substrates are heated up to a high temperature, which induces the abrupt steps to reflow into slopes with $(1\bar{1}0n)$ facets. Finally, EGNRs are grown epitaxially on the patterned slopes in the SiC by thermal decomposition of Si atoms. By carefully tuning the growth recipe, the patterned SiC sidewalls can be selectively graphitized, which results in separate and well-defined EGNRs without any connecting EG on the flat SiC surfaces. Also by carefully selecting the orientation of the sidewalls relative to the SiC substrate, EGNRs with both zigzag and armchair edges can be reliably grown. In addition, the relatively simple photolithographic definition of the nickel masks allows for the controlled fabrication of very large EGNR arrays with well-defined physical dimensions including the width and the length of the individual EGNRs, and the pitch, the area and the areal fill factor of the entire EGNR array.

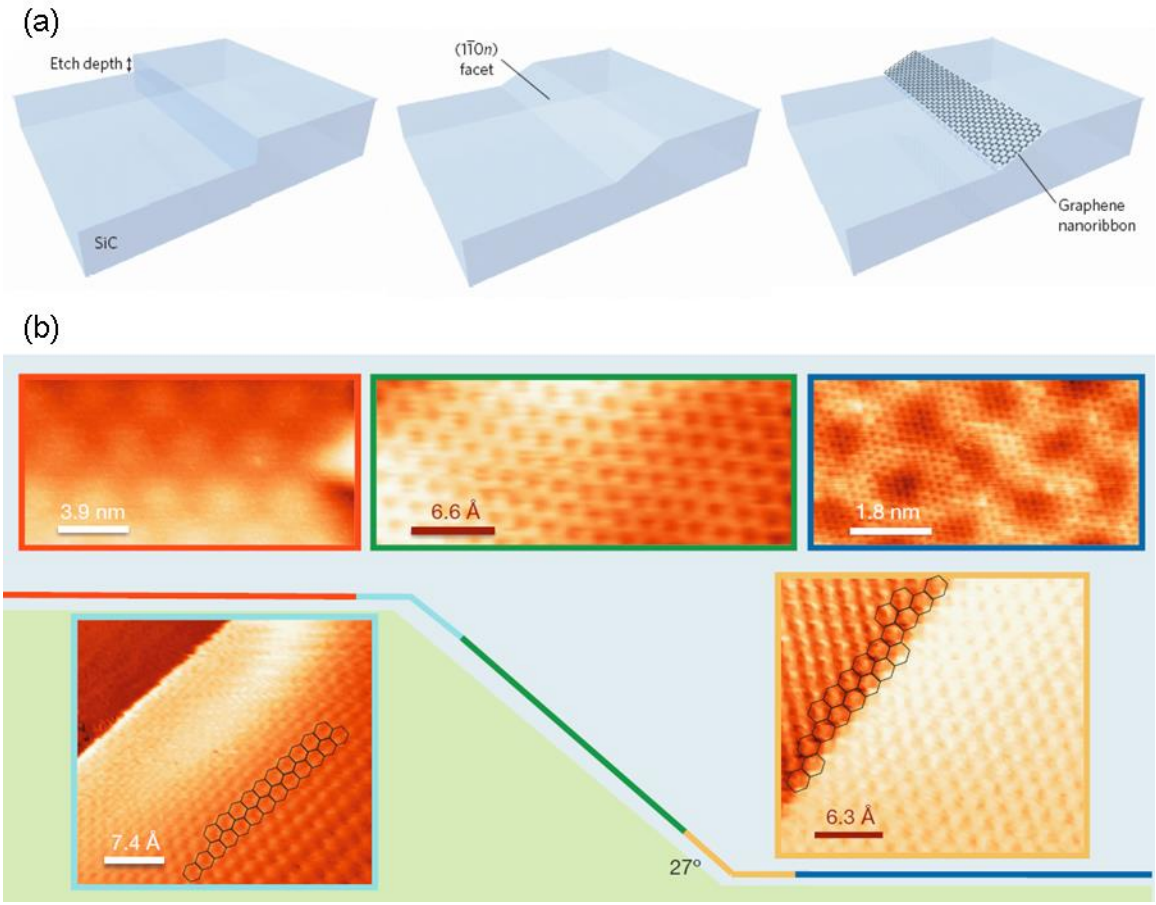

Figure 2.5.1 – (a) Schematic diagram illustrating the fabrication process of an EGNR on SiC. (Adapted from Ref. [99].) (b) High-resolution scanning tunneling microscopy (STM) image of an EGNR and the adjacent flat SiC surfaces. (Adapted from Ref. [18].)

A whole range of characterization techniques including high-resolution transmission electron microscopy (TEM), Raman spectroscopy, atomic force microscopy (AFM), electrostatic force microscopy (EFM), high-resolution angle-resolved photoemission spectroscopy (ARPES), high-resolution scanning tunneling microscopy (STM), scanning tunneling spectroscopy (STS), and electronic transport measurements have been used to confirm the exceptionally high quality of EGNRs, which is characteristic for EG in general [18, 91, 99]. Figure 2.5.1(b) [18] shows high-resolution STM images of an EGNR and the adjacent flat SiC surfaces. We note that both the middle section and the edges of the EGNR are atomically clean and well-defined.

The band structure of a finite graphene nanoribbon with zigzag edges is illustrated schematically in Figure 2.5.2 [18]. We note that the quantum confinement of carriers in the

quasi-0D graphene nanoribbon results in high energy subbands and lifts the degeneracy of the edge state at zero energy. Within a simple quantum mechanical model for a particle in a 2D square potential with infinitely high walls, the energy spectrum of the graphene nanoribbon can be approximated by [18]:

$$E_{n,m} = \pm\hbar v_F \sqrt{\left(\frac{n\pi}{W}\right)^2 + \left(\frac{m\pi}{L}\right)^2}, \tag{2.5.1}$$

where W and L are the width and the length of the graphene nanoribbon, respectively, v_F is the Fermi velocity, and $\{n, m\}$ is the full set of subband quantum numbers. We also note that the inter-subband separation is controlled by W, while the edge state separation is controlled by L, where we assume that $L \gg W$. For example, for W = 500 nm and L ~ 1 mm, the lowest subband energy is $E_{1,0}$ ≈ 4 meV (≈ 48 K ≈ 1 THz). Similarly, for W ~ 50 nm and L = 500 nm, the edge state energy is $E_{0,1}$ ≈ 4 meV (≈ 48 K ≈ 1 THz). Hence, THz spectroscopy could be used to probe the edge state or inter-subband transitions in graphene nanoribbons.

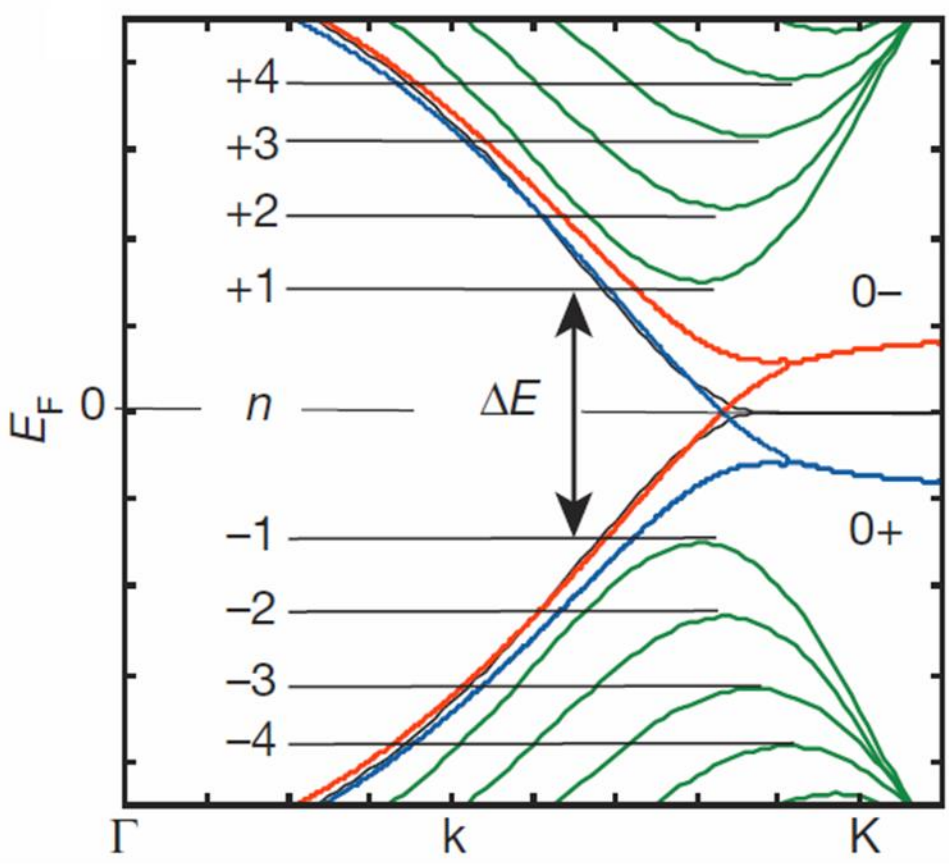

Figure 2.5.2 – Energy band structure of a finite graphene nanoribbon with zigzag edges. (Adapted from Ref. [18].)

In this section, we utilize ultrafast time-resolved THz spectroscopy to investigate the hot carrier relaxation and cooling dynamics of EGNRs. In this work, we prepared an EGNR sample, which contains a large area array of parallel identical EGNRs. The individual EGNRs consist of ~1-2 layers of EG, have nominally zigzag edges and have nominal dimensions of $W \approx 1$ μm and $L \approx 200$ μm. These nominal dimensions correspond to values for the lowest subband energy of $E_{1,0} \approx 2$ meV (≈ 24 K ≈ 0.5 THz) and for the edge state energy of $E_{0,1} \sim 0$ meV (≈ 0 K ≈ 0 THz). Hence, the EGNR sample design places the inter-subband transitions well within the detectable THz bandwidth, while the edge state degeneracy is practically not lifted. However, we note that it is possible that the grown EGNRs are not continuous across the patterned SiC sidewalls with $W \approx 1$ μm, but they buckled into multiple parallel sub-ribbons. This imperfect growth would reduce and randomize the actual width of the individual EGNRs, and correspondingly increase and non-homogeneously broaden the subband energies. In addition, the introduced

intermediate EGNR edges might not be as well-defined and/or chiral. The pitch of the patterned SiC sidewalls is ~2 μm, which gives an estimate of ~50% for the areal fill factor of the EGNR array. We note that a more diverse set of better characterized EGNR samples is further needed and is currently under work.

To underscore the profound influence of the quantum confinement effects in EGNRs, we study the dependence of the THz carrier dynamics of the EGNRs on their orientation with respect to the THz probe polarization. Figure 2.5.3(a) and (b) show the differential THz transmission at the peak of the THz probe pulse normalized to the THz transmission without photoexcitation, $\Delta t/t$, as a function of pump-probe delay for the EGNR sample with nominal $W \approx 1$ μm, for parallel and perpendicular THz polarization, respectively. The data is recorded at a substrate temperature of 300 K for variable pump fluence (corresponding to different initial carrier temperature). The secondary increases or decreases in the differential THz transmission at ~7 and ~14 ps are due to round-trip reflections of the optical pump inside the substrate that photoexcite additional carriers.

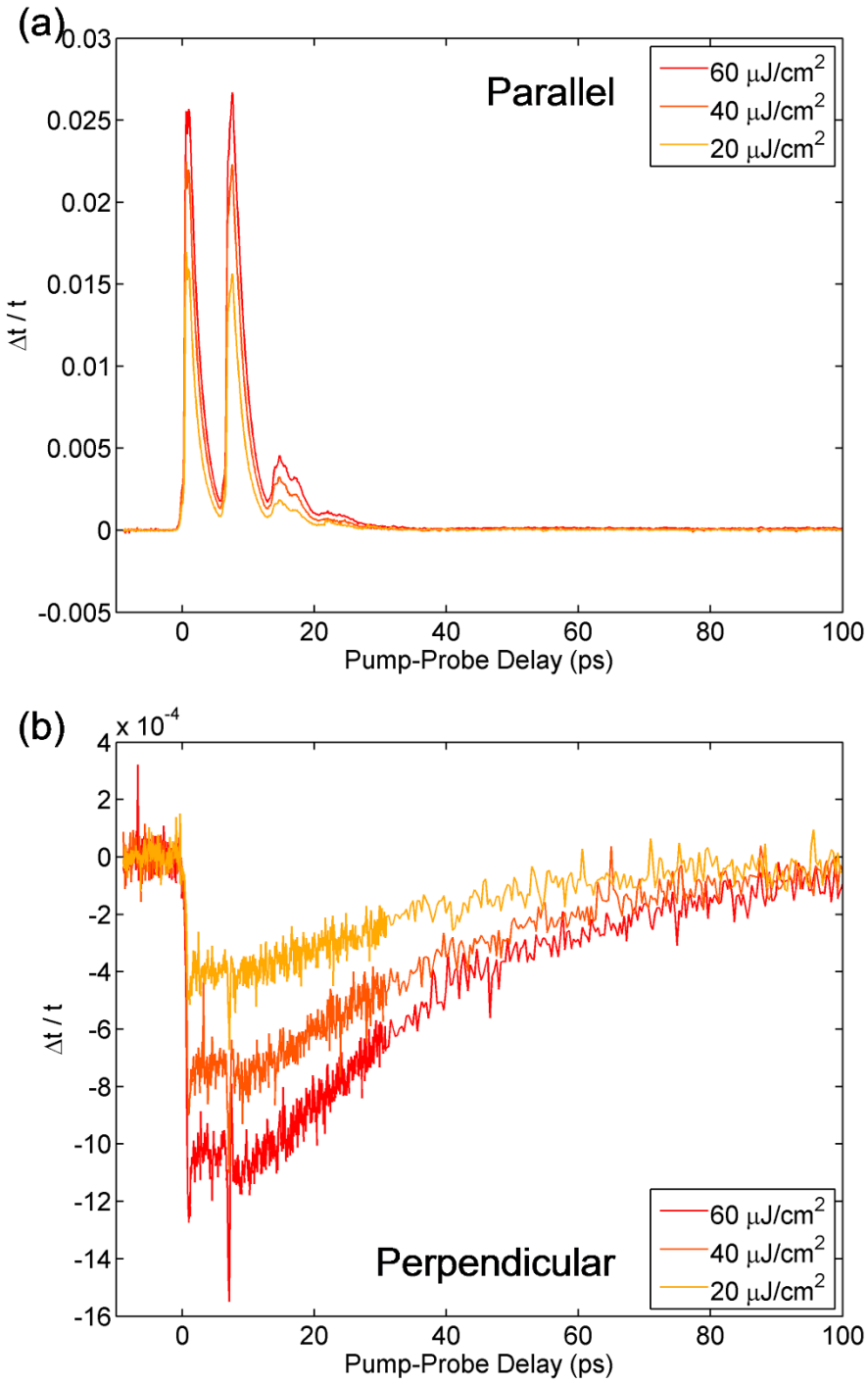

Figure 2.5.3 – Differential THz transmission at a substrate temperature of 300 K for a few different pump fluences for an EGNR sample for (a) parallel and (b) perpendicular THz polarization.

We observe that the THz carrier dynamics of the EGNRs exhibit a pronounced anisotropy with the THz polarization. Interestingly, we note that when the THz polarization is parallel to the EGNR array, we recover the THz response of pristine highly doped

graphene. Both the positive sign and the relaxation timescale of a few picoseconds of the differential THz transmission are completely reproduced. This observation can be intuitively understood that in the parallel orientation the THz probe can drive a microscopic current along the EGNRs similar to pristine graphene. The high doping in the EGNR sample can be attributed to water vapor adsorption from the environment similar to the CVDG samples. In very sharp contrast, when the THz polarization is perpendicular to the EGNR array, the THz response of the EGNRs is strikingly different. Because the EGNR width is ultra-subwavelength compared to the THz wavelength (λ/W on the order of ~300 or more), the THz probe cannot drive a microscopic current in the perpendicular orientation and hence the THz absorption is strongly suppressed. We propose that the optical pump injects hot carriers in the high energy subbands, which induces excited state absorption of the THz probe likely due to inter-subband transitions. We note that this is consistent with the negative sign of the differential THz transmission, which corresponds to enhanced THz absorption upon photoexcitation. Within this physical model, the relaxation of the differential THz transmission is related to the carrier lifetimes in the high energy subbands, which extend up to on the order of a hundred picoseconds. These long carrier lifetimes can be attributed to the exceptionally high quality of the EGNRs.

Section 2.6 Summary for Graphene

In conclusion, we have studied the dynamic THz response and the hot-carrier dynamics of a wide variety of high quality graphene, including epitaxial and chemical-vapor-deposited (CVD), following ultrafast photoexcitation using ultrafast time-resolved THz spectroscopy. First, we discussed the dynamic THz response of pristine epitaxial (EG) and CVD (CVDG) graphene, which is characteristic for a pristine disorder-free graphene layer. We looked at doped and undoped (very lightly doped) graphene and we observed relaxation times which depend critically on the Fermi level, ranging from a few picoseconds for high doping densities to hundreds of picoseconds for very low doping densities. These THz carrier dynamics are quantitatively explained using a microscopic density-matrix theory of carrier-carrier and carrier-phonon interactions, without the need to invoke disorder or any other extrinsic mechanisms, and without the need for any free fitting parameters; the theory accounts explicitly for the time-dependent response of the

hot carriers to the THz probe field. Acoustic phonon interactions are found not to be important on these picoseconds timescales. The hot-carrier relaxation and cooling dynamics are governed by an interplay of carrier-carrier and carrier-optical-phonon scattering. Physically, the high-energy tail of the hot-carrier distribution relaxes via the emission of optical phonons, and the carrier-carrier scattering processes very efficiently and continuously rethermalize the carrier population. A Drude model approximation to the full microscopic theory can provide only a semi-qualitative framework for interpreting the experimental data in doped and undoped graphene at low excitation fluences; however, the full microscopic theory is required to explain the data quantitatively for all excitation levels.

Then, we discussed the dynamic THz response of multilayer epitaxial graphene (MEG), in which interlayer interactions play an important role. We developed a theory of hot-carrier equilibration based on interlayer energy transfer via screened Coulomb interactions between electrons in the many top low-density (LD) layers and in the few high-density (HD) layers close to the underlying SiC substrate in MEG. The theory is complicated by the essential role of dynamic screening of the electron-electron interactions in all MEG layers through the temperature-dependent charge carrier response. To obtain a transparent theory, we made two well-justified simplifications. First, we noted that screening in the relevant temperature, wave vector, and frequency regime is dominated by the first few HD layers close to the substrate, allowing us to neglect the screening by the top LD layers. Second, we noted that energy transfer among the LD layers is much stronger than between LD and HD layers, and we therefore could describe all LD layers by a common electron temperature. We compared the calculated cooling dynamics with the relaxation dynamics measured via ultrafast time-resolved THz spectroscopy. The observed experimental dynamics exhibit the expected timescales, dependence on lattice temperature, and dependence on number of epitaxial graphene layers predicted by the theory, providing strong support for the proposed mechanism, within the approximations necessary in the development of the theory. The theoretical approach developed here may be expected to be applicable to many other types of layered two-dimensional (2D) electron systems. These may include semiconductor heterostructures as well as the wide variety of novel 2D

materials under active development including transition metal dichalcogenides (e.g. MoS_2, $MoSe_2$, WS_2, and WSe_2) and other van der Waals heterostructures.

Then, we discussed the dynamic THz response of buckled epitaxial graphene (BEG), in which an energy gap of up to ~0.7 eV had been carefully engineered. We observed that the THz carrier dynamics of BEG are up to two orders of magnitude faster relative to pristine EG under identical experimental conditions. We attributed this remarkable enhancement to the relaxation of the phase space constraints near the Dirac point due to the presence of a finite bandgap, which allows the conduction and the valence band to be bridged by very efficient optical phonon emission. Our conclusions are consistent with similar experimental results combined with rigorous microscopic theory calculations performed on a wide variety of graphene samples. Furthermore, they suggest that the bandgap introduced in BEG is strongly non-homogenously broadened, with local values below the optical phonon energy of ~200 meV, where carrier recombination occurs. The ability to manipulate carrier relaxation times by orders of magnitude could find application in the design of novel graphene-based devices that incorporate both metallic and semiconducting graphene films with various bandgaps.

Finally, we discussed the dynamic THz response of epitaxial graphene nanoribbons (EGNRs), in which carriers are carefully quantum confined in 2D. We observed that the THz carrier dynamics of the EGNRs exhibit a pronounced anisotropy with the THz polarization, which is a clear manifestation of the quantum confinement effects. In the parallel THz polarization, the dynamic THz response of the EGNRs resembles that of pristine highly doped graphene, because the THz probe can drive an unconstrained microscopic current along the EGNRs. In very sharp contrast, in the perpendicular THz polarization, the dynamic THz response of the EGNRs is strikingly modified, because the microscopic current is largely constrained and hence the THz absorption is strongly suppressed. We proposed that the optical pump injects hot carriers in the high energy subbands, which induces excited state absorption of the THz probe likely due to inter-subband transitions. We also observed long carrier lifetimes in the high energy subbands on the order of a hundred picoseconds attributed to the exceptionally high quality of the EGNRs.

Section 2.7 References

[1] A. K. Geim and K. S. Novoselov, "The rise of graphene," *Nat. Mater.* **6**, 183-191 (2007).

[2] A. H. Castro Neto et al., "The electronic properties of graphene," *Rev. Mod. Phys.* **81**, 109-162 (2009).

[3] R. R. Nair et al., "Fine Structure Constant Defines Visual Transparency of Graphene," *Science* **320**, 1308 (2008).

[4] K. S. Novoselov et al., "Electric Field Effect in Atomically Thin Carbon Films," *Science* **306**, 666-669 (2004).

[5] K. S. Novoselov et al., "Two-dimensional gas of massless Dirac fermions in graphene," *Nature* **438**, 197-200 (2005).

[6] C. Berger et al., "Ultrathin Epitaxial Graphite: 2D Electron Gas Properties and a Route toward Graphene-based Nanoelectronics," *J. Phys. Chem. B* **108**, 19912-19916 (2004).

[7] C. Berger et al., "Electronic confinement and coherence in patterned epitaxial graphene," *Science* **312**, 1191-1196 (2006).

[8] W. A. de Heer et al., "Large area and structured epitaxial graphene produced by confinement controlled sublimation of silicon carbide," *Proc. Natl. Acad. Sci. U.S.A.* **108**, 16900-16905 (2011).

[9] X. Li et al., "Large-Area Synthesis of High-Quality and Uniform Graphene Films on Copper Foils," *Science* **324**, 1312-1314 (2009).

[10] W. A. de Heer et al., "Epitaxial graphene," *Solid State Commun.* **143**, 92-100 (2007).

[11] W. A. de Heer et al., "Epitaxial graphene electronic structure and transport," *J. Phys. D: Appl. Phys.* **43**, 374007 (2010).

[12] W. A. de Heer, "Epitaxial graphene: A new electronic material for the 21st century," *MRS Bulletin* **36**, 632-639 (2011).

[13] J. Hass et al., "Why multilayer graphene on 4H-SiC(0001) behaves like a single sheet of graphene," *Phys. Rev. Lett.* **100**, 125504 (2008).

[14] C. Faugeras et al., "Few-layer graphene on SiC, pyrolitic graphite, and graphene: a Raman scattering study," *Appl. Phys. Lett.* **92**, 011914 (2008).

[15] M. Sprinkle et al., "First direct observation of a nearly ideal graphene band structure," *Phys. Rev. Lett.* **103**, 226803 (2009).

[16] Y. Hao et al., "The role of surface oxygen in the growth of large single-crystal graphene on copper," *Science* **342**, 720-723 (2013).

[17] S. Lee et al., "Wafer scale homogeneous bilayer graphene films by chemical vapor deposition," *Nano Lett.* **10**, 4702-4707 (2010).

[18] J. Baringhaus et al., "Exceptional ballistic transport in epitaxial graphene nanoribbons," *Nature* **506**, 349-354 (2014).

[19] J. Martin et al., "Observations of electron-hole puddles in graphene using a scanning single-electron transistor," *Nat. Phys.* **4**, 144-148 (2008).

[20] Y. B. Zhang et al., "Origin of spatial charge inhomogeneity in graphene," *Nat. Phys.* **5**, 722-726 (2009).

[21] S. Y. Jung et al., "Evolution of microscopic localization in graphene in a magnetic field from scattering resonances to quantum dots," *Nat. Phys.* **7**, 245-251 (2011).

[22] S. Y. Zhou et al., "Substrate-induced bandgap opening in epitaxial graphene," *Nat. Mater.* **6**, 770-775 (2007).

[23] D. Sun et al., "Ultrafast relaxation of excited Dirac fermions in epitaxial graphene using optical differential transmission spectroscopy," *Phys. Rev. Lett.* **101**, 157402 (2008).

[24] D. Sun et al., "Spectroscopic measurements of interlayer screening in multilayer epitaxial graphene," *Phys. Rev. Lett.* **104**, 136802 (2010).

[25] Y.-C. Chang et al., "Extracting the complex optical conductivity of mono- and bilayer graphene by ellipsometry," *Appl. Phys. Lett.* **104**, 261909 (2014).

[26] Y.-W. Tan et al., "Measurement of scattering rate and minimum conductivity in graphene," *Phys. Rev. Lett.* **99**, 246803 (2007).

[27] J.-H. Chen et al., "Charged-impurity scattering in graphene," *Nat. Phys.* **4**, 377-381 (2008).

[28] C. R. Dean et al., "Boron nitride substrates for high-quality graphene electronics," *Nat. Nanotech.* **5**, 722-726 (2010).
[29] X. Du et al., "Approaching ballistic transport in suspended graphene," *Nat. Nanotech.* **3**, 491-495 (2008).
[30] M. Breusing et al., "Ultrafast nonequilibrium carrier dynamics in a single graphene layer," *Phys. Rev. B* **83**, 153410 (2011).
[31] S. Winnerl et al., "Carrier Relaxation in Epitaxial Graphene Photoexcited Near the Dirac Point," *Phys. Rev. Lett.* **107**, 237401 (2011).
[32] E. Malic et al., "Microscopic theory of absorption and ultrafast many-particle kinetics in graphene," *Phys. Rev. B* **84**, 205406 (2011).
[33] E. Malic et al., "Efficient orientational carrier relaxation in optically excited graphene," *App. Phys. Lett.* **101**, 213110 (2012).
[34] M. Mittendorff et al., "Anisotropy of Excitation and Relaxation of Photogenerated Charge Carriers in Graphene," *Nano Lett.* **14**, 1504-1507 (2014).
[35] T. Winzer et al., "Carrier Multiplication in Graphene," *Nano Lett.* **10**, 4839-4843 (2010).
[36] T. Winzer et al., "Microscopic mechanism for transient population inversion and optical gain in graphene," *Phys. Rev. B* **87**, 165413 (2013).
[37] D. Brida et al., "Ultrafast collinear scattering and carrier multiplication in graphene," *Nat. Comm.* **4**, 1987 (2013).
[38] J. C. W. Song et al., "Photoexcited carrier dynamics and impact-excitation cascade in graphene," *Phys. Rev. B* **87**, 155429 (2013).
[39] T. Li et al., "Femtosecond Population Inversion and Stimulated Emission of Dense Dirac Fermions in Graphene," *Phys. Rev. Lett.* **108**, 167401 (2012).
[40] T. Plötzing et al., "Experimental Verification of Carrier Multiplication in Graphene," *Nano Lett.* **14**, 5371-5375 (2014).
[41] P. A. George et al., "Ultrafast optical-pump terahertz-probe spectroscopy of the carrier relaxation and recombination dynamics in epitaxial graphene," *Nano Lett.* **8**, 4248-4251 (2008).
[42] J. H. Strait et al., "Very slow cooling dynamics of photoexcited carriers in graphene observed by optical-pump terahertz-probe spectroscopy," *Nano Lett.* **11**, 4902-4906 (2011).
[43] C. J. Docherty et al., "Extreme sensitivity of graphene photoconductivity to environmental gases," *Nat. Commun.* **3**, 1228 (2012).
[44] G. Jnawali et al., "Observation of a transient decrease in terahertz conductivity of single-layer graphene induced by ultrafast optical excitation," *Nano Lett.* **13**, 524-530 (2013).
[45] S.-F. Shi et al., "Controlling graphene ultrafast hot carrier response from metal-like to semiconductor-like by electrostatic gating," *Nano Lett.* **14**, 1578-1582 (2014).
[46] A. J. Frenzel et al., "Observation of suppressed terahertz absorption in photoexcited graphene," *Appl. Phys. Lett.* **102**, 113111 (2013).
[47] K. J. Tielrooij et al., "Photoexcitation cascade and multiple hot-carrier generation in graphene," *Nat. Phys.* **9**, 248-252 (2013).
[48] S. A. Jensen et al., "Competing ultrafast energy relaxation pathways in photoexcited graphene," *Nano Lett.* **14**, 5839-5845 (2014).
[49] A. J. Frenzel et al., "Semiconducting-to-metallic photoconductivity crossover and temperature-dependent Drude weight in graphene," *Phys. Rev. Lett.* **113**, 056602 (2014).
[50] R. Bistritzer and A. H. MacDonald, "Electronic cooling in graphene," *Phys. Rev. Lett.* **102**, 206410 (2009).
[51] W.-K. Tse and S. Das Sarma, "Energy relaxation of hot Dirac fermions in graphene," *Phys. Rev. B* **79**, 235406 (2009).
[52] J. C. W. Song et al., "Disorder-assisted electron-phonon scattering and cooling pathways in graphene," *Phys. Rev. Lett.* **109**, 106602 (2012).
[53] E. Malic et al., "Graphene and Carbon Nanotubes: Ultrafast Optics and Relaxation Dynamics," Wiley-VCH, Weinheim (2013).
[54] I. Gierz et al., "Snapshots of non-equilibrium Dirac carrier distributions in graphene," *Nat. Mater.* **12**, 1119-1124 (2013).
[55] M. W. Graham et al., "Photocurrent measurements of supercollision cooling in graphene," *Nat. Phys.* **9**, 103-108 (2013).
[56] A. C. Betz et al., "Supercollision cooling in undoped graphene," *Nat. Phys.* **9**, 109-112 (2013).

[57] M. Tinkham, "Energy gap interpretation of experiments on infrared transmission through superconducting films," *Phys. Rev.* **104**, 845-846 (1956).
[58] M. Orlita e al., "Carrier scattering from dynamical magnetoconductivity in quasineutral epitaxial graphene," *Phys. Rev. Lett.* **107**, 216603 (2011).
[59] S. Xu et al., "Energy dependence of electron lifetime in graphite observed with femtosecond photoemission spectroscopy," *Phys. Rev. Lett.* **76**, 483 (1996).
[60] J. González et al., "Unconventional quasiparticle lifetime in graphite," *Phys. Rev. Lett.* **77**, 3589 (1996).
[61] T. Ando, "Screening effect and impurity scattering in monolayer graphene," *J. Phys. Soc. Jpn.* **75**, 074716 (2006).
[62] S. Das Sarma et al., "Electronic transport in two-dimensional graphene," *Rev. Mod. Phys.* **83**, 407 (2011).
[63] A. K. Geim and I. V. Grigorieva, "Van der Waals heterostructures," *Nature* **499**, 419-425 (2013).
[64] L. Britnell et al., "Strong light-matter interactions in heterostructures of atomically thin films," *Science* **340**, 1311-1314 (2013).
[65] Q. H. Wang et al., "Electronics and optoelectronics of two-dimensional transition metal dichalcogenides," *Nat. Nanotech.* **7**, 699-712 (2012).
[66] C.-H. Liu et al., "Graphene photodetectors with ultra-broadband and high responsivity at room temperature," *Nat. Nanotech.* **9**, 273-278 (2014).
[67] D. Sun et al., "Hot carrier cooling by acoustic phonons in epitaxial graphene by ultrafast pump-probe spectroscopy," *Phys. Status Solidi C* **8** (4), 1194-1197 (2011).
[68] J. K. Gamble et al., "Cooling of cryogenic electron bilayers via the Coulomb interaction," *Phys. Rev. B* **84**, 125321 (2011).
[69] M. Prunnila and S. J. Laakso, "Interlayer heat transfer in bilayer carrier systems," *New J. Phys.* **15**, 033043 (2013).
[70] H. Min et al., "Landau levels and band bending in few-layer epitaxial graphene," *Phys. Rev. B* **83**, 155430 (2011).
[71] S. S. Datta et al., "Surface potentials and layer charge distributions in few-layer graphene films," *Nano. Lett.* **9**, 7-11 (2009).
[72] G. W. Semenoff, "Condensed-matter simulation of a three-dimensional anomaly," *Phys. Rev. Lett.* **53**, 1194-1197 (1984).
[73] J. González et al., "Non-Fermi liquid behavior of electrons in the half-filled honeycomb lattice (A renormalization group approach)," *Nucl. Phys. B* **424**, 595-618 (1994).
[74] K. W.-K. Shung, "Dielectric function and plasmon structure of stage-1 intercalated graphite," *Phys. Rev. B* **34**, 979 (1986).
[75] M. R. Ramezanali et al., "Finite-temperature screening and the specific heat of doped graphene," *J. Phys. A: Math. Theor.* **42**, 214015 (2009).
[76] A. Faridi et al., "Temperature dependence of the paramagnetic spin susceptibility of doped graphene," *Phys. Rev. B* **85**, 214015 (2012).
[77] A. Tomadin et al., "Non-equilibrium dynamics of photo-excited electrons in graphene: collinear scattering, Auger processes, and the impact of screening," *Phys. Rev. B* **88**, 035430 (2013).
[78] G. F. Giuliani and G. Vignale, "Theory of the Electron Liquid," Cambridge University Press, Cambridge (2005).
[79] R. E. V. Profumo et al., "Electron-electron interactions in decoupled graphene layers," *Phys. Rev. B* **82**, 085443 (2010).
[80] O. Ilic et al., "Near-field thermal radiation transfer controlled by plasmons in graphene," *Phys. Rev. B* **85**, 155422 (2012).
[81] N. P. R. Hill et al., "Correlation effects on the coupled plasmon modes of a double quantum well," *Phys. Rev. Lett.* **78**, 2204-2207 (1997).
[82] K. Flensberg and B. Y.-K. Hu, "Coulomb drag as a probe of coupled plasmon modes in parallel quantum wells," *Phys. Rev. Lett.* **73**, 3572-3575 (1994).
[83] J. C. W. Song and L. S. Levitov, "Energy-driven drag at charge neutrality in graphene," *Phys. Rev. Lett.* **109**, 236602 (2012).
[84] Y.-M. Lin et al., "100-GHz transistors from wafer-scale epitaxial graphene," *Science* **327**, 662 (2010).
[85] F. Schwierz, "Graphene transistors," *Nat. Nanotech.* **5**, 487-496 (2010).

[86] K. S. Novoselov et al., "A roadmap for graphene," *Nature* **490**, 192-200 (2012).
[87] Y. Zhang et al., "Direct observation of a widely tunable bandgap in bilayer graphene," *Nature* **459**, 820-823 (2009).
[88] S. Niyogi et al., "Spectroscopy of covalently functionalized graphene," *Nano Lett.* **10**, 4061-4066 (2010).
[89] S. Sarkar et al., "Covalent chemistry in graphene electronics," *Mater. Today* **15** (6), 276-285 (2012).
[90] M. Y. Han et al., "Energy band-gap engineering of graphene nanoribbons," *Phys. Rev. Lett.* **98**, 206805 (2007).
[91] J. Hicks et al., "A wide-bandgap metal-semiconductor-metal nanostructure made entirely from graphene," *Nat. Phys.* **9**, 49-54 (2013).
[92] F. Wang et al., "Wide-gap semiconducting graphene from nitrogen-seeded SiC," *Nano Lett.* **13**, 4827-4832 (2013).
[93] K. Nakada et al., "Edge state in graphene ribbons: Nanometer size effect and edge shape dependence," *Phys. Rev. B* **54**, 17954-17961 (1996).
[94] Y.-W. Son et al., "Energy Gaps in Graphene Nanoribbons," *Phys. Rev. Lett.* **97**, 216803 (2006).
[95] K. S. Yi et al., "Low-energy electronic states and heat capacities in graphene strips," *Phys. Rev. B* **76**, 115410 (2007).
[96] L. Brey and H. A. Fertig, "Electronic States of Graphene Nanoribbons," *arXiv:cond-mat/0603107 [cond-mat.mes-hall]*, (2008).
[97] K. Wakabayashi et al., "Edge effect on electronic transport properties of graphene nanoribbons and presence of perfectly conducting channel," *Carbon* **47**, 124-137 (2009).
[98] K. Wakabayashi et al., "Edge States and Flat Bands of Graphene Nanoribbons with Edge Modification," *J. Phys. Soc. Jpn.* **79**, 034706 (2010).
[99] M. Sprinkle et al., "Scalable templated growth of graphene nanoribbons on SiC," *Nat. Nanotech.* **5**, 727-731 (2010).

Chapter 3

Ultrafast THz Response of Semiconductor Nanowires

In Chapter 3, we discuss the dynamic THz response and the hot-carrier dynamics of semiconductor nanowires following ultrafast photoexcitation. We look specifically at high quality single-crystal germanium (Ge) and germanium/silicon (Ge/Si) core/shell nanowires (NWs). In Section 3.1, we first introduce the studied Ge and Ge/Si core/shell NWs. In Section 3.2, we discuss the THz carrier dynamics of the NWs. In Section 3.3, we discuss the full dynamic THz response of the NWs. In Section 3.4, we finally present a brief summary of the results in Chapter 3.

Section 3.1 Germanium and Germanium/Silicon Core/Shell Nanowires

In this section, we introduce the studied Ge and Ge/Si core/shell NWs including synthesis, fabrication and characterization.

The Ge/Si NWs are grown on oxidized Si wafers in a quartz tube furnace using a two-step chemical vapor deposition (CVD) process [1, 2]. First, a single-crystal Ge core is grown in the [111] crystallographic direction using Au nanoparticles (Ted Pella) as catalysts for nucleation. Second, an epitaxial Si shell is grown on top to encapsulate the Ge core. A schematic cross-sectional diagram, a schematic energy band alignment diagram and a representative high-resolution transmission electron microscopy (TEM) image of a high-quality Ge/Si NW is presented in Figure 3.1.1 [1]. We note the exceptional degree of crystallinity and the very clean, epitaxial heterostructure interface of the Ge/Si NW. The strain arising from the lattice mismatch of ~4% between the Ge core and the Si shell is elastically relaxed along the radial direction, which yields a type II staggered band alignment as shown in Figure 3.1.1 [1]. The valence band offset of ~500 meV at the heterostructure interface creates a confinement potential in which free holes accumulate.

Electrical transport measurements show that this quasi-one-dimensional (1D) quantum well leads to a larger carrier density and a reduced surface scattering, which enhance the DC conductivity and the DC mobility of the Ge/Si NWs compared to the plain Ge NWs [1, 2].

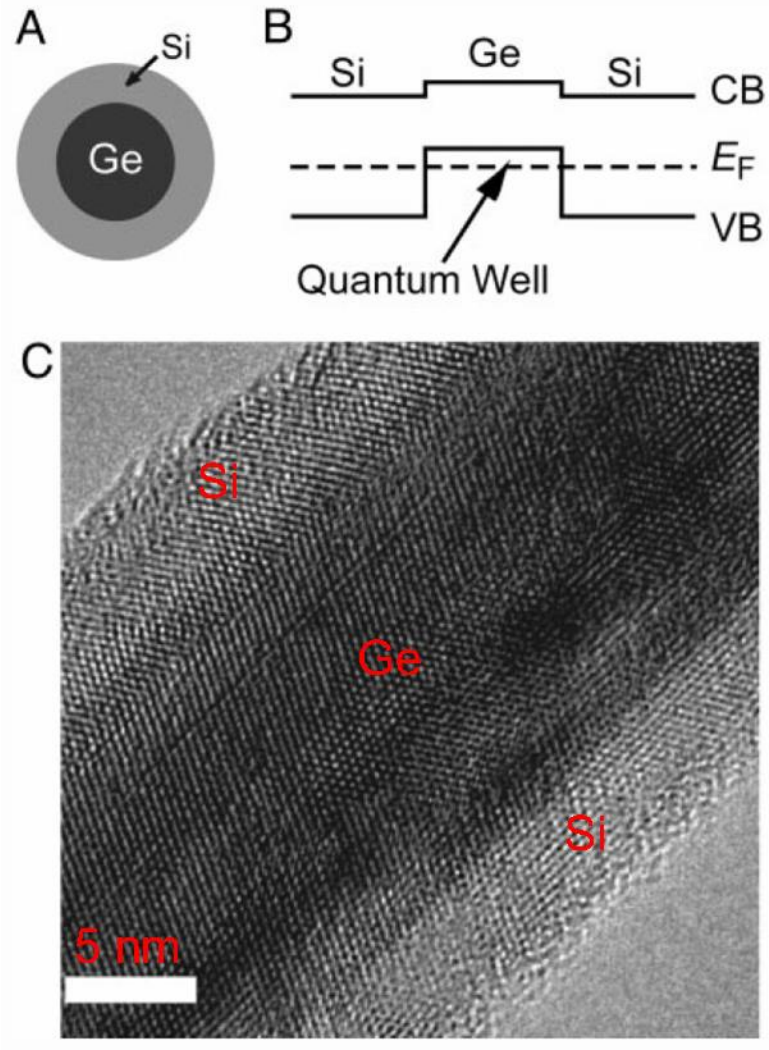

Figure 3.1.1 – (a) Schematic cross-sectional diagram, (b) schematic energy band alignment diagram and (c) high-resolution transmission electron microscopy (TEM) image of a high-quality Ge/Si NW. (Adapted from Ref. [1].)

For the work in this chapter, we grow a series of Ge/Si NWs with Ge core diameters of ~10, ~20 and ~40 nm (which we call Ge-10/Si-2, Ge-20/Si-2 and Ge-40/Si-2, respectively) by varying the size of the Au catalyst nanoparticles. The Si shell has an average thickness of ~2 nm for all three types of NWs. In addition, we grow a series of Ge NWs similarly with Ge core diameters of ~10, ~20 and ~40 nm (which we call Ge-10, Ge-

20 and Ge-40) by skipping the Si shell deposition step, but otherwise using the same recipe. All NWs have similar lengths on the order of a few tens of microns, which gives NW aspect ratios (length/width) on the order of ~1,000. All NWs are intrinsic with an estimated unintentional p-type doping density of ~10^{15}-10^{16} cm^{-3}. Schematic cross-sectional diagrams of the complete set of Ge and Ge/Si NWs is presented in Figure 3.1.2.

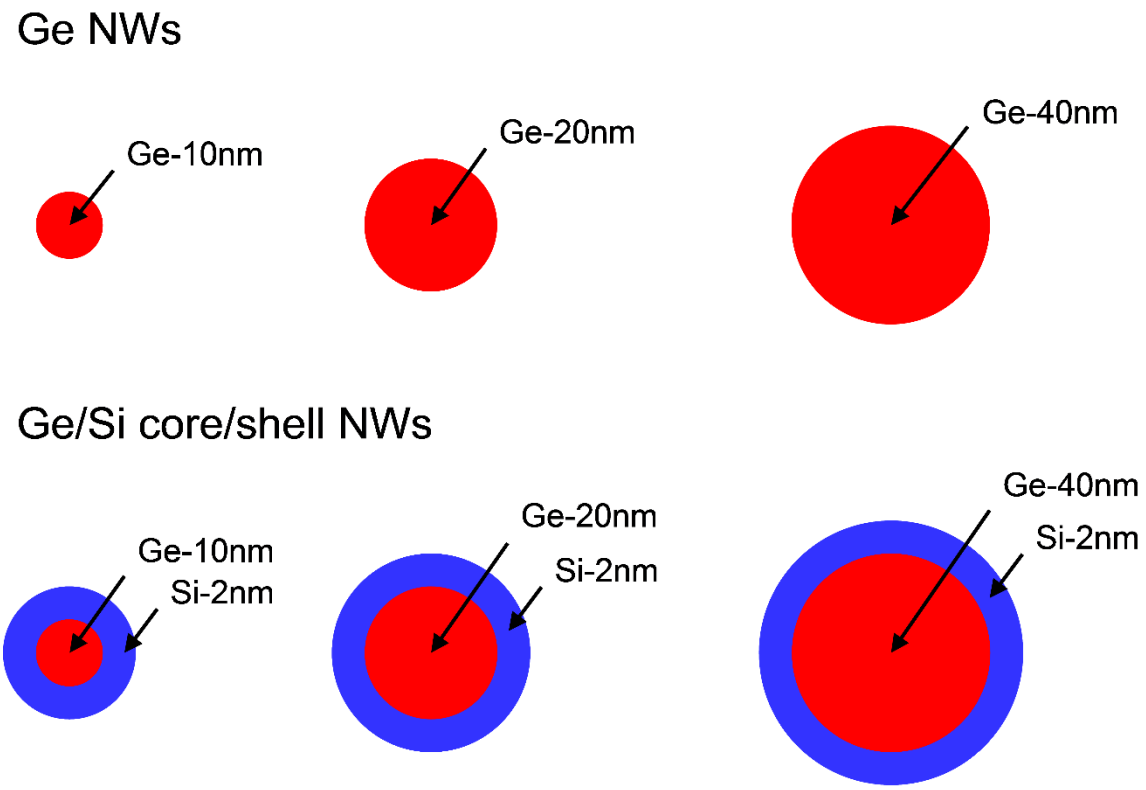

Figure 3.1.2 – Schematic cross-sectional diagrams of Ge and Ge/Si NWs.

After growth, the NWs are transferred to C-cut single-crystal sapphire substrates (Alfa Aesar) using a simple mechanical contact printing method [3], which orients the NWs. A representative scanning electron microscopy (SEM) image of an oriented NW sample is shown in Figure 3.1.3. We observe that due to the simplicity of the sample fabrication technique, the NWs are not perfectly aligned, with some NWs breaking up, bending, meandering, or bunching together. However, the NW array is roughly oriented in a general direction, which is completely sufficient for measuring the dynamic THz response. A much more sophisticated technique such as lithographic processing will be necessary to achieve a better alignment of the NW array, which can be a topic of further studies.

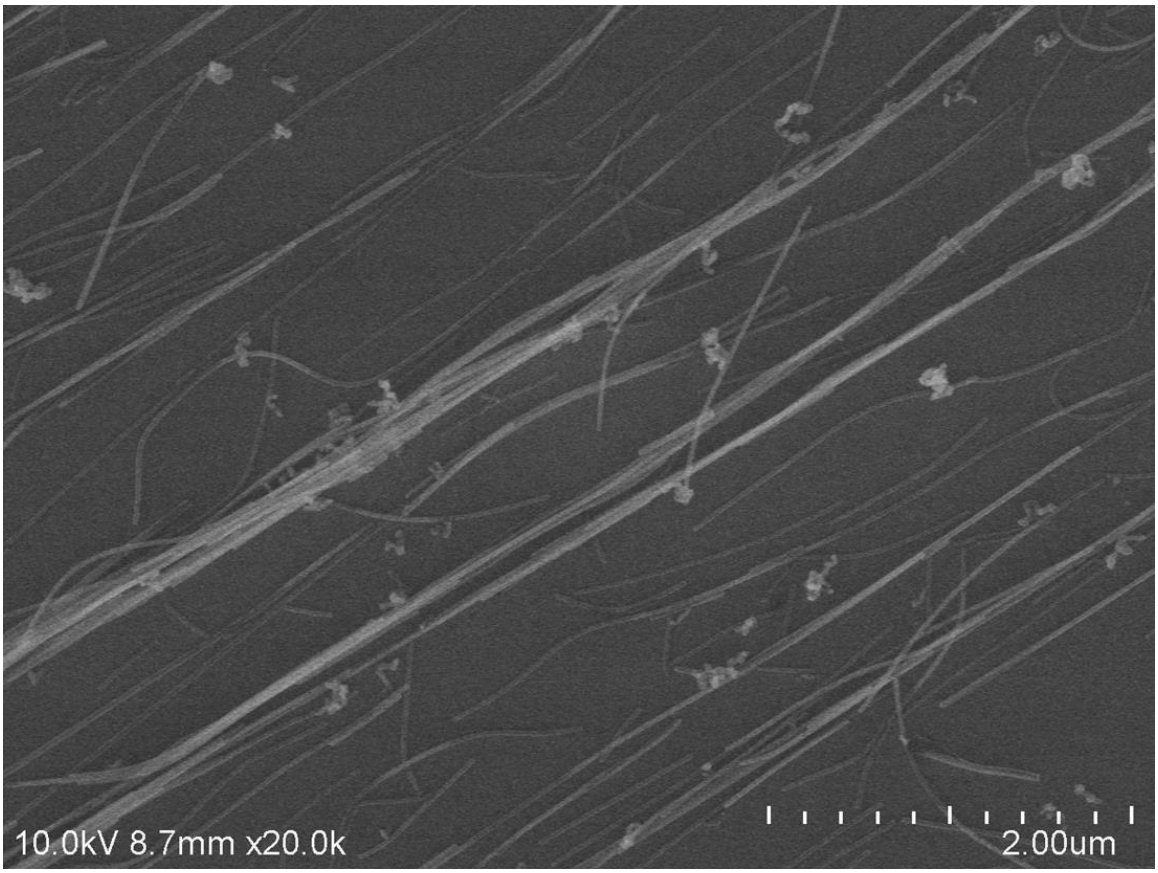

Figure 3.1.3 – Scanning electron microscopy (SEM) image of an oriented NW sample.

Section 3.2 THz Carrier Dynamics

In this section, we discuss the transient THz carrier dynamics of the NWs following ultrafast photoexcitation.

Using the ultrafast time-resolved THz spectroscopy technique, we measure the full time-domain differential change in the THz probe pulse transmission through the NW samples due to photoexcitation by the optical pump pulse, which we then normalize to the THz transmission in the absence of photoexcitation, $\Delta t/t$. From the measured time-domain differential THz electric field, $\Delta t/t$, we can obtain the frequency-domain differential THz spectrum, $\Delta t(\omega)/t(\omega)$, by straightforward numerical Fourier transformation. Then, using purely electromagnetic analysis, by solving the Maxwell's equations with the proper boundary conditions for the incident and transmitted THz radiation, this experimental quantity can be related through the Tinkham formula [4] to the photoinduced change in the complex bulk conductivity of the NWs, $\Delta\sigma_b(\omega)$, via:

$$\Delta\sigma_b(\omega) \approx -\frac{n_{sub}+n_{air}}{\eta_0 d_{eff}} \times \frac{\Delta t(\omega)}{t(\omega)}, \tag{3.2.1}$$

where n_{sub} and n_{air} are the THz refractive indices of the substrate and the environment, respectively, η_0 is the impedance of free space, and $d_{eff} = df$ is the effective thickness of the NW array, which includes both the physical thickness d of the NW array and the fraction f of sample surface covered with NWs. This direct linear relationship holds true for small differential THz transmission signals and for samples that are much thinner than the wavelength of the THz radiation as is the case for the NW arrays, which allows us to use the effective medium approximation for the THz response of the NWs. The precise determination of the effective thickness d_{eff} is complicated by the irregular structure of the NW array and the variations in the structure from sample to sample and from position to position on the same sample. To correct for these irregularities and variations, we can define a photoinduced change in the complex sheet conductivity of the NWs, $\Delta\sigma_s(\omega)$, by dividing out the effective thickness d_{eff} to obtain:

$$\Delta\sigma_s(\omega) \approx -\frac{n_{sub}+n_{air}}{\eta_0} \times \frac{\Delta t(\omega)}{t(\omega)}. \tag{3.2.2}$$

Thus, we can directly obtain the dynamic THz response of the NWs, which we can then match to a physical model for the photoinduced THz conductivity to extract relevant material parameters. We will postpone the discussion of the full dynamic THz response of the NWs until Section 3.3.

In this section, as a first experimental approach, we probe the intraband and interband THz carrier dynamics of the NWs by measuring the differential THz transmission at the peak of the THz probe pulse normalized to the THz transmission without photoexcitation $\Delta t/t$ as a function of pump-probe delay. By doing so, we lose the frequency information, but we gain experimental convenience and enhance the signal-to-noise ratio (SNR) of the measurements. We also develop a simple physical model (which we call photoexcited carrier density model), in which we assume that the normalized differential THz transmission $\Delta t/t$ and the photoinduced THz conductivity $\Delta\sigma$ are directly proportional to the number of photoexcited carriers, Δn, which absorb the THz probe:

$$\Delta\sigma \sim \Delta n \sim -\frac{\Delta t}{t}. \tag{3.2.3}$$

Figure 3.2.1 [5] shows the band structure of bulk single-crystal germanium and the process of carrier photoexcitation by the optical pump (photon energy $h\nu \approx 1.55$ eV), which we will use to illustrate our discussion. We consider the absorption of the optical pump and the THz probe only in the single-crystal Ge core, because the Si shell is comparatively much smaller. To gain physical insight we vary a large set of parameters including the NW orientation, the pump fluence, the substrate temperature, the NW core diameter and the NW composition with or without a shell.

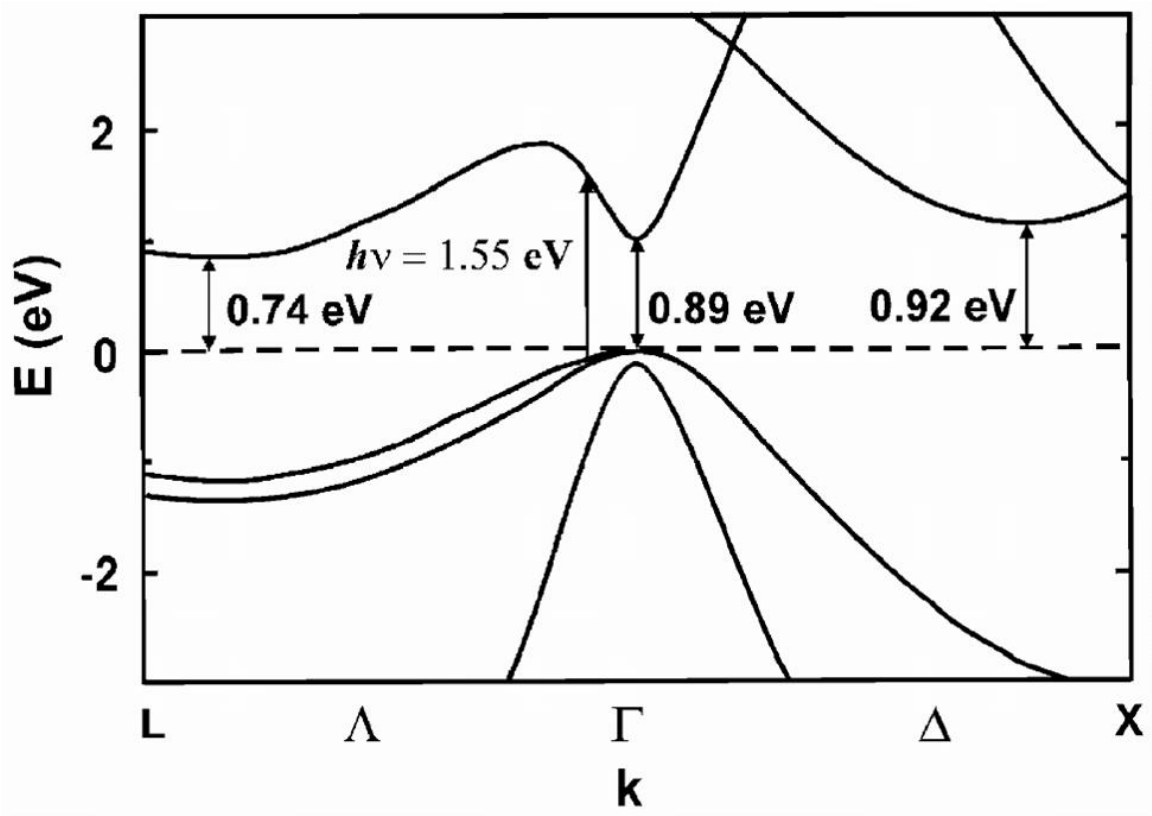

Figure 3.2.1 – Energy band structure of bulk single-crystal germanium. (Adapted from Ref. [5].)

First, we study the dependence of the THz carrier dynamics of the NWs on the NW orientation with respect to the optical pump and the THz probe polarizations. The optical pump and the THz probe are both linearly polarized, and we orient them to be co-polarized in the vertical direction as illustrated schematically in the inset of Figure 3.2.2(a). The NW array is also roughly oriented in a general direction, which we call the NW orientation. Then, we mechanically rotate the NW sample to change the orientation angle defined as the angle between the optical pump/THz probe polarization and the NW orientation. Figure

3.2.2(a) shows the normalized differential THz transmission at the peak of the THz probe pulse $\Delta t/t$ as a function of pump-probe delay for variable orientation angle at a fixed pump fluence of 60 μJ/cm^2, measured for NW sample Ge-20, which is representative for all NW samples. We observe that the THz carrier dynamics of the NWs exhibit a pronounced anisotropy with the NW orientation relative to the optical pump/THz probe polarization, which we attribute to the very large NW aspect ratio. The absolute value of the differential THz transmission is largest when the NWs are parallel to the polarization direction and decreases monotonically to almost zero when the NWs are perpendicular. Because the NW diameters are ultra-subwavelength compared to both the optical and the THz wavelength (λ/d on the order of ~10 and ~10,000, respectively), the optical pump and the THz probe absorption is strongly suppressed in the perpendicular orientation. To obtain more quantitative results, we plot the maximum absolute value of the normalized differential THz transmission as a function of the orientation angle in Figure 3.2.2(b). We note that the maximum differential THz transmission signal can be fit very well by a cosine cube function with the orientation angle, $max\{|\Delta t/t|\} \sim \cos^3(\theta)$. This dependence is predicted theoretically, because the optical pump intensity absorption contributes a cosine square factor and the THz probe field absorption contributes another cosine factor. In all subsequent experiments, we orient the NW arrays paralleled to the optical pump/THz probe polarization to maximize the detected THz response.

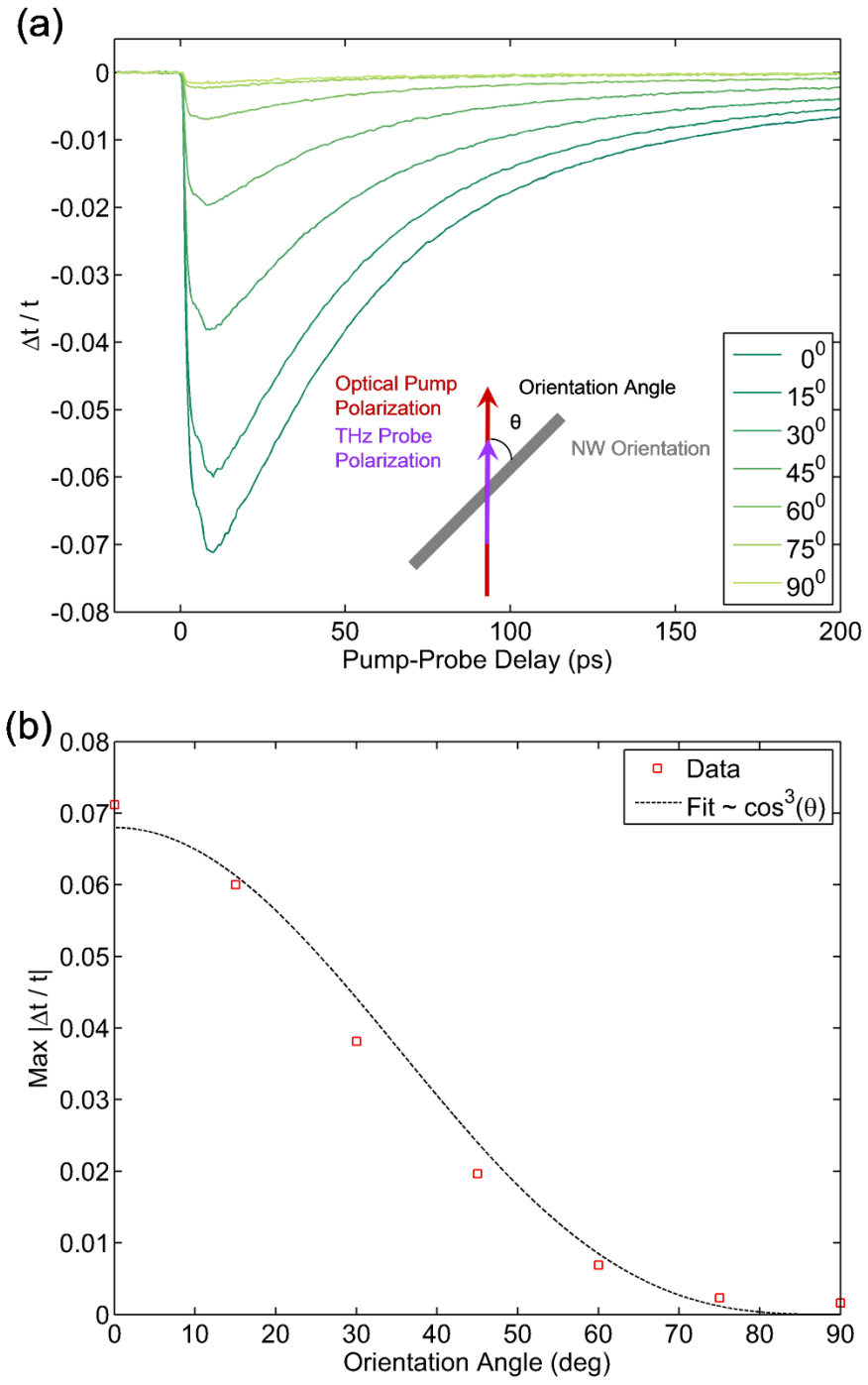

Figure 3.2.2 – (a) Differential THz transmission for variable NW orientation relative to the optical pump/THz probe polarization for NW sample Ge-20. (Inset: Schematic diagram of the NW orientation and the optical pump/THz probe polarization, which form the orientation angle.) (b) Maximum absolute value of differential THz transmission as a function of the orientation angle for NW sample Ge-20.

Next, we study the dependence of the THz carrier dynamics of the NWs on the pump fluence (or the photoexcited carrier density). Figure 3.2.3 shows the normalized

differential THz transmission at the peak of the THz probe pulse $\Delta t/t$ as a function of pump-probe delay for variable pump fluence measured for NW sample Ge-10. The differential THz transmission decreases gradually in the first ~10 ps after photoexcitation and then it recovers within ~600 ps in an exponential-like fashion. The small dip in the dynamics around ~5 ps is a result of a secondary photoexcitation from the first Fabry-Perot etalon reflection of the pump pulse inside the sapphire substrate. The observed photoexcited carrier dynamics can be qualitatively explained as a combination of both faster intraband relaxation and slower interband recombination processes [6, 7]. Initially, the incident optical pump pulse creates electron-hole pairs near the direct bandgap in the Γ valley of the germanium band structure (see Figure 3.2.1). The hot electrons in the Γ valley relax first mainly to the X valley within a couple hundred femtoseconds and eventually to the indirect bandgap in the L valley within a picosecond due to strong intervalley phonon scattering [8, 9, 10, 11]. Electron thermalization and cooling also occur on a picosecond timescale due to intervalley and intravalley phonon scattering [8, 9, 10, 11]. Simultaneously, the hot holes in the light-hole and the split-off bands relax to the heavy-hole band within a couple hundred femtoseconds due to intraband phonon scattering. There, the holes thermalize and subsequently cool down to the valence band edge via carrier-carrier scattering and optical phonon emission, respectively, within a picosecond [11, 12, 13, 14].

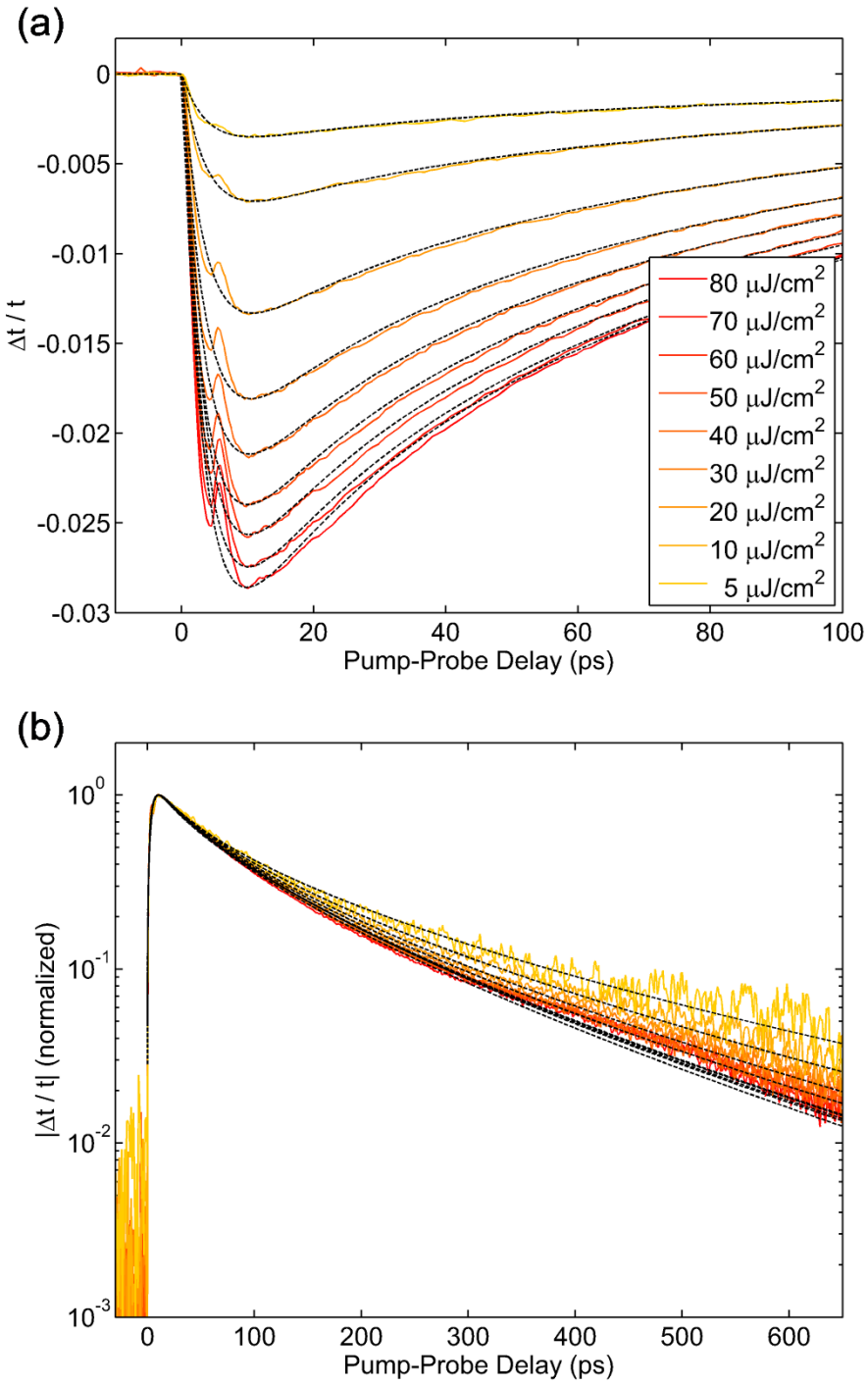

Figure 3.2.3 – Differential THz transmission for variable pump fluence for NW sample Ge-10 fitted with the photoexcited carrier density model.

The presence of excess free carriers, which can be treated as positive photoinduced THz conductivity, increases the THz absorption as manifested in the decreased THz transmission. As the excess electrons and holes recombine on a much slower, but again

very similar [6] timescale, the THz transmission recovers to its pre-excitation level. We propose that the photoexcited carriers migrate from the inside to the surface of the NWs, where they recombine via surface defect states, as explained in detail below. Bulk recombination times in intrinsic or low-doped single crystal germanium have been reported to approach or even exceed microsecond timescales [15], which are much longer than the sub-nanosecond dynamics observed in our experiments. The faster mechanism of Auger recombination becomes important only at higher doping densities of above 10^{18} cm^{-3} [15] than the ones we estimate for our NWs based on previous electrical measurements [1, 2]. Consequently, we conclude that the vast majority of photoexcited carriers recombine via surface defects in agreement with previous optical measurements [6, 7]. In sharp contrast to these studies, however, we see clear indications of ballistic rather than diffusive carrier transport. More evidence to support these claims is presented later.

In this physical model, we assume that only the relaxed electrons in the L valley and holes in the Γ valley contribute a positive photoinduced THz conductivity change proportional to their combined instantaneous density. This also explains why when the pump pulse reflection re-excites some of these carriers back to high energies, the THz transmission slightly increases until they relax again. Since both the intraband and interband dynamics of electrons and holes are expected to evolve on a very similar timescale, we model only the total carrier density. In this three energy level picture, the total transient photoexcited carrier densities at high, $\Delta n^{(h)}(t)$, and low, $\Delta n^{(l)}(t)$, energies are given by the following two coupled decay equations:

$$\Delta n^{(h)}(t) = \Delta n_0^{(h)}(t) \times \exp\left(-\frac{t}{\tau_\alpha}\right), \tag{3.2.4}$$

$$\Delta n^{(l)}(t) = -\Delta n_0^{(l)}(t) \times \exp\left(-\frac{t}{\tau_\alpha}\right) + \Delta n_0^{(l)}(t) \times \exp\left(-\left(\frac{t}{\tau_\beta}\right)^{1/h}\right), \tag{3.2.5}$$

where τ_α is the intraband relaxation time, τ_β is the characteristic interband recombination time and h ($h \geq 1$) is the heterogeneity parameter quantifying local NW diameter and surface defect density variations both along a single NW and among different NWs. The stretched exponential dynamics in Equation 3.2.5 represents the existence of a continuous distribution of interband recombination times resulting from these variations [16, 17, 18,

19, 20]. The mean value of the distribution, $\langle\tau_\beta\rangle$, is a physically more meaningful quantity given by $\langle\tau_\beta\rangle = \tau_\beta h\Gamma(h)$, where $\Gamma(\cdot)$ is the gamma function.

We perform identical measurements and analysis on NW sample Ge-10/Si-2, which are shown in Figure 3.2.4. When constructing the fits this time, we ignore a section of the data around ~5 ps to prevent the unwanted secondary photoexcitation from skewing the results. We observe again excellent agreement between the experiment and the model. We note that both the intraband relaxation and the interband recombination dynamics speed up significantly due to the Si shell, the reasons for which are explained in detail below. Figure 3.2.5 shows the maximum absolute value of the normalized differential THz transmission $max\{|\Delta t/t|\}$ as a function of pump fluence for NW samples Ge-10 and Ge-10/Si-2. We observe that the THz response of both NW samples shows very similar saturation with the pump fluence.

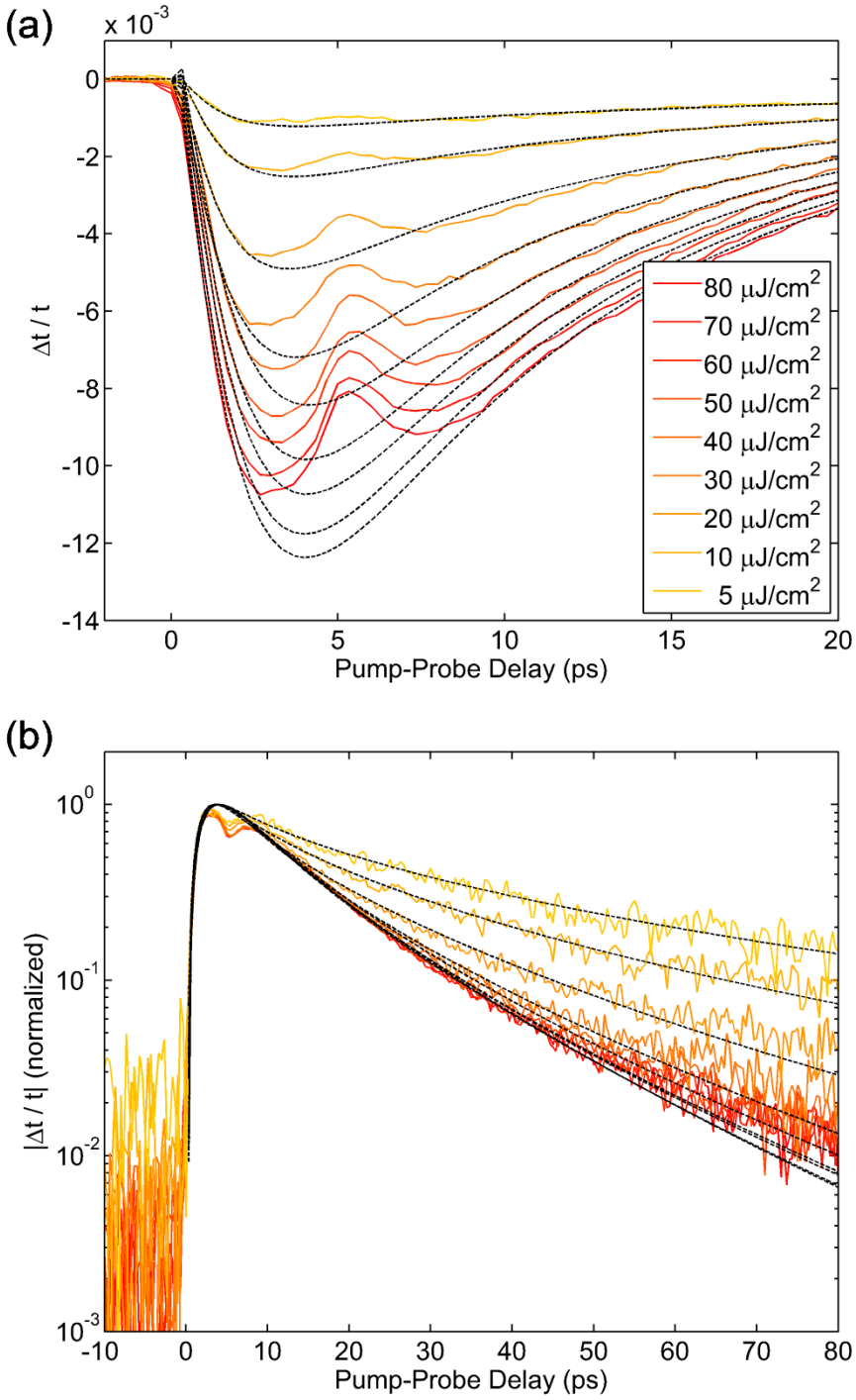

Figure 3.2.4 – Differential THz transmission for variable pump fluence for NW sample Ge-10/Si-2 fitted with the photoexcited carrier density model.

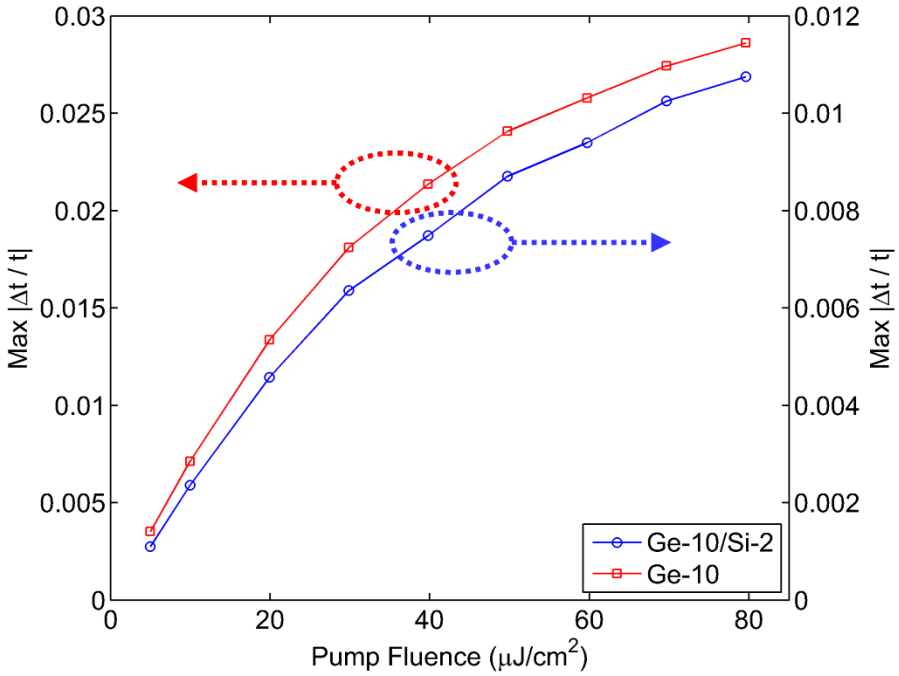

Figure 3.2.5 – Maximum absolute value of differential THz transmission as a function of the pump fluence for NW samples Ge-10 and Ge-10/Si-2.

The values of the intraband relaxation time τ_α, the mean interband recombination time $\langle\tau_\beta\rangle$ and the heterogeneity parameter h, extracted from the fits, as a function of pump fluence for NW samples Ge-10 and Ge-10/Si-2 are summarized in Figure 3.2.6. We observe that the intraband relaxation time is completely independent of the pump fluence for both NW samples. In addition, τ_α is shorter for the NWs with a Si shell, which we attribute to elastic strain relaxation of the Ge core. On the other hand, both the mean interband recombination time and the heterogeneity parameter exhibit a slight, but pronounced monotonic decrease with the pump fluence, F, which is well described by an exponential function of the form $a \times exp(-bF) + c$, where a, b and c are constants. It has been reported in previous studies [6, 21, 22] that the surface defect states, which lie inside the Ge bandgap, are filled with electrons and that creates a negative electric field bending the bands upwards. This causes free holes to accumulate near the surface to maintain charge neutrality, while free electrons have to surmount a potential barrier and remain near the center of the NWs. At low photoexcited carrier density, the electrons and the holes are spatially separated, which results in longer mean interband recombination times. As the photoexcited carrier density increases with the pump fluence, the electrons begin to screen

the negative surface field and have a higher probability to reach the surface, where recombination occurs. This space-charge field effect is weak, so that $\langle \tau_\beta \rangle$ rapidly saturates with the pump fluence. We note that this is also consistent with surface recombination, but not Shockley-Reed-Hall or Auger recombination. The photoexcited carrier density dependence of h can similarly be explained by the increasing carrier screening of the surface defects that diminishes the effects of their local variations and in essence makes the NWs appear more uniform as h approaches unity.

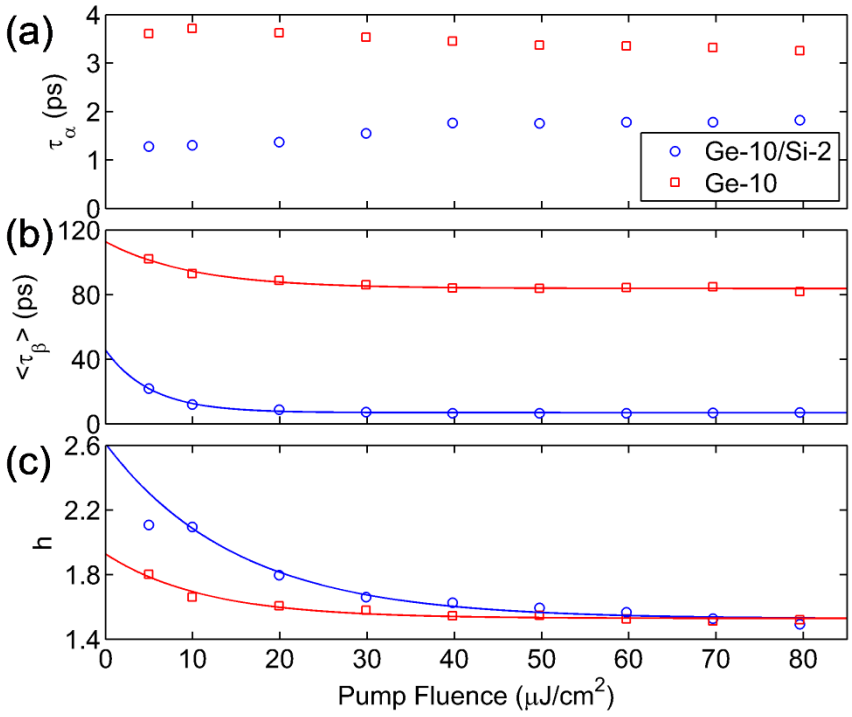

Figure 3.2.6 – (a) Intraband relaxation time, (b) mean interband recombination time and (c) heterogeneity parameter extracted from the photoexcited carrier density model fits as a function of the pump fluence for NW samples Ge-10 and Ge-10/Si-2.

Next, we study the dependence of the THz carrier dynamics of the NWs on the NW core diameter (or the NW volume-to-surface-area ratio). We measure the normalized differential THz transmission at the peak of the THz probe pulse $\Delta t/t$ as a function of pump-probe delay for NW samples with Ge core diameters of ~10, ~20 and ~40 nm both with and without a Si shell at a fixed pump fluence of 60 μJ/cm^2. The experimental data together with the photoexcited carrier density model fits is shown in Figure 3.2.7.

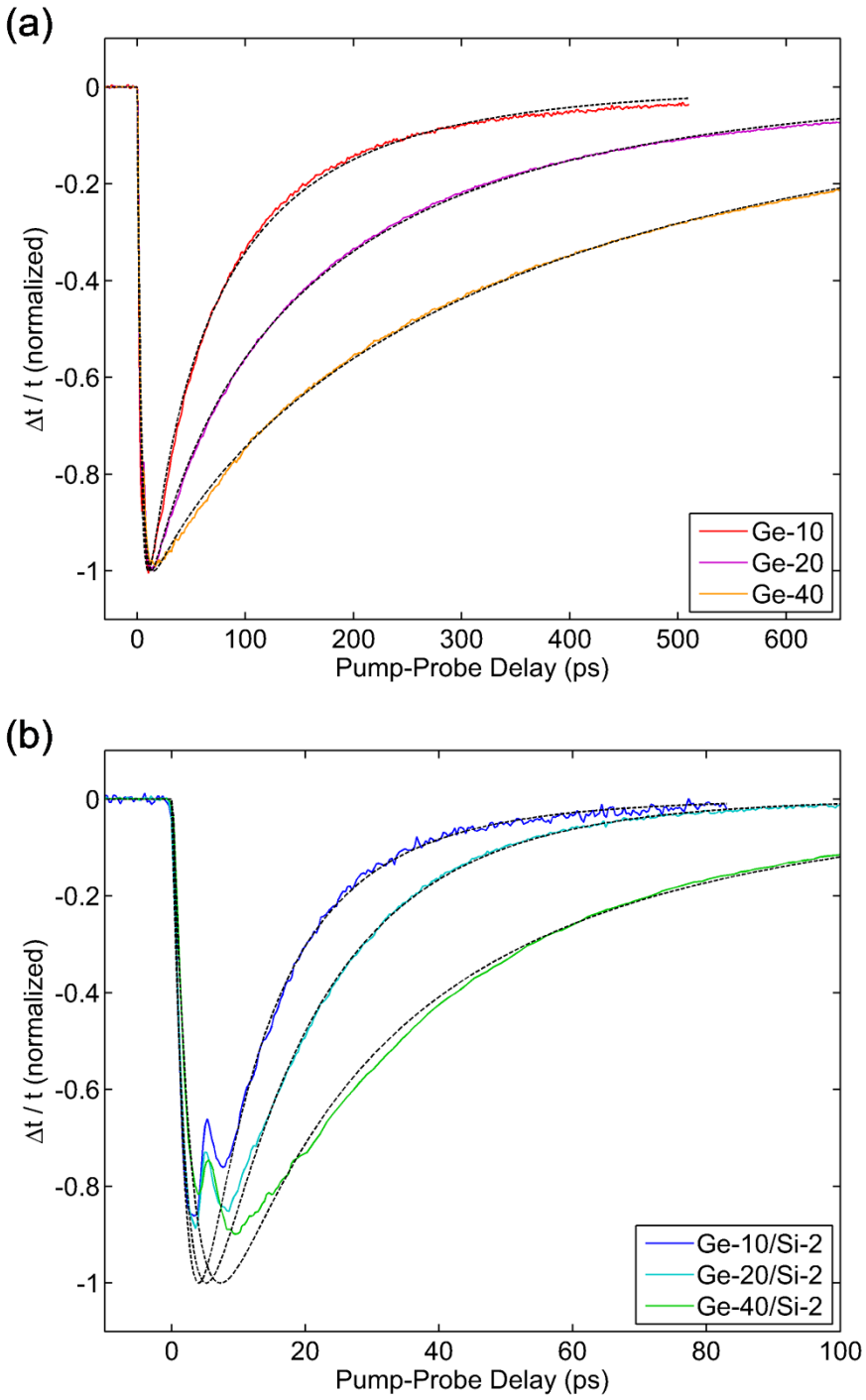

Figure 3.2.7 – Differential THz transmission for variable NW core diameter for (a) Ge and (b) Ge/Si NWs fitted with the photoexcited carrier density model.

The values of the extracted parameters for all NW samples are summarized in Figure 3.2.8. We observe that the intraband relaxation time for the Ge NWs is independent of the core diameter as it can be anticipated, since the various intraband phonon scattering

rates should not vary with core diameter. For the Ge/Si NWs, however, the intraband relaxation time is lower than that for the Ge NWs at the same core diameter and the difference increases monotonically with the decrease of the core diameter. This is attributed to an increasing elastic strain relaxation of the Ge core due to the epitaxial Si shell as the mass of the core and the shell become comparable. The interband recombination time increases with the core diameter for both Ge and Ge/Si NWs that again supports our assumption for the dominance of surface over bulk recombination. Hence, we express the interband recombination time as the sum of a diffusion, τ_{diff}, and a surface recombination, τ_{sr}, component:

$$\langle \tau_\beta \rangle = \tau_{diff} + \tau_{sr} = \frac{r_{eff}^2}{\pi^2 D} + \frac{r_{eff}}{s}, \tag{3.2.6}$$

where D is the diffusion coefficient, s is the surface recombination velocity and r_{eff} is the effective core radius. As it will be confirmed later in Section 3.3, the diffusion time is much smaller than the surface recombination time for the measured core diameters and it can be neglected. By fitting a straight line to each of the two data sets, we obtain an estimate for the surface recombination velocity of $s = 5.4 \times 10^3$ cm/s and $s = 7.1 \times 10^4$ cm/s for the Ge and the Ge/Si NWs, respectively. We note that these values are consistent with previously reported values [6]. We conclude that the shorter photoexcited carrier lifetimes for the Ge/Si NWs result from a higher surface defect density at the Ge/Si interface corresponding to a larger surface recombination velocity. We also suspect that for the Ge NWs oxidation can act to passivate dangling bonds and reduce surface defect density, while for the Ge/Si NWs the native oxide on the Si shell can prevent the oxidation of the Ge/Si interface, where recombination occurs. The effect of the Ge core oxidation is further supported by the observation that the lifetimes of the Ge NWs increased gradually and eventually saturated as the NW samples aged over time. In sharp contrast, the lifetimes of the Ge/Si NWs remained completely unchanged over time. In addition, the linear relationship between the photoexcited carrier lifetime and the core diameter suggests predominantly ballistic rather than diffusive carrier transport in agreement with previous electrical transport measurements [1, 2]. The photoexcited carriers bounce many times against the NW walls before they are captured by a surface defect state and recombine. The heterogeneity

parameter does not follow an apparent trend, but it still falls within a relatively narrow range for all NW samples that indicates comparable NW uniformity.

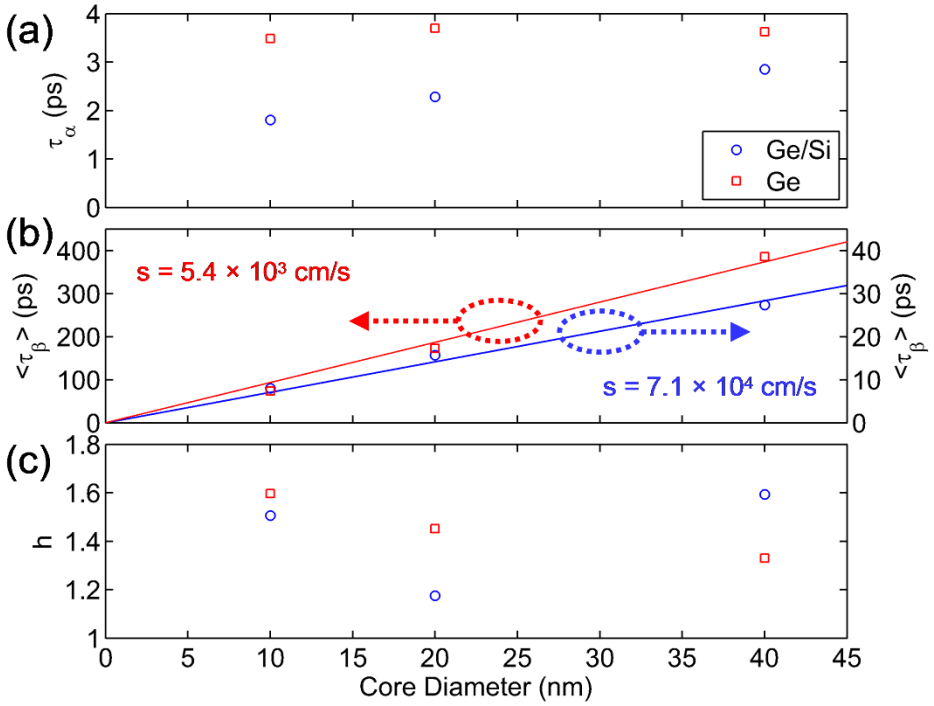

Figure 3.2.8 – (a) Intraband relaxation time, (b) mean interband recombination time and (c) heterogeneity parameter extracted from the photoexcited carrier density model fits as a function of the NW core diameter for Ge and Ge/Si NWs.

Next, we study the dependence of the THz carrier dynamics of the NWs on the substrate temperature. Figure 3.2.9(a) shows the normalized differential THz transmission at the peak of the THz probe pulse $\Delta t/t$ as a function of pump-probe delay for variable substrate temperature at a fixed pump fluence of 60 μJ/cm^2, measured for NW sample Ge-20. The experimental data is again fit very well with the photoexcited carrier density model. Figure 3.2.9(b) shows the maximum absolute value of the normalized differential THz transmission $max\{|\Delta t/t|\}$ as a function of substrate temperature. We observe that the THz response of the NWs exhibits weak dependence on the substrate temperature in good agreement with previous electrical transport measurements of the DC conductivity of the NWs [1, 2].

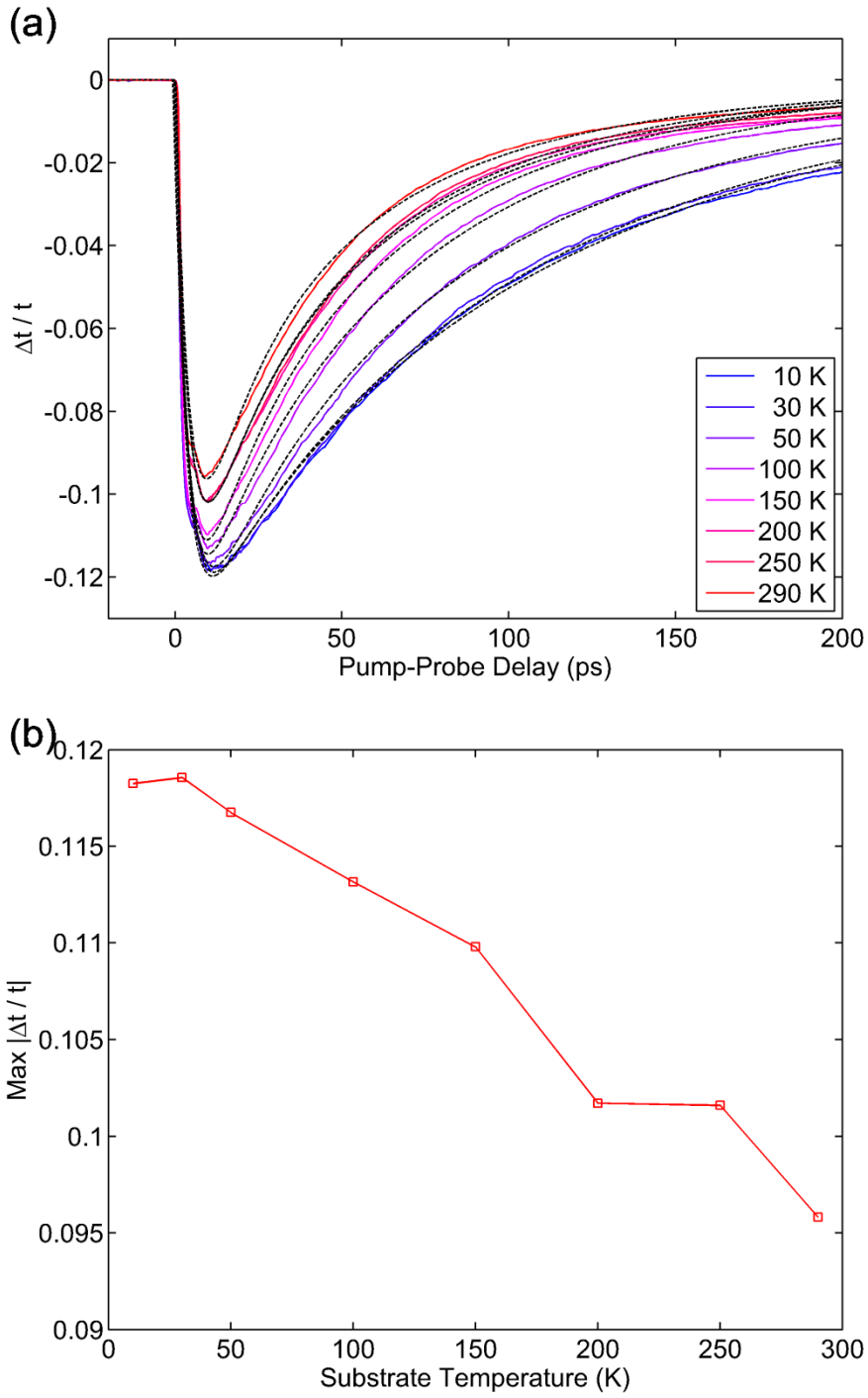

Figure 3.2.9 – (a) Differential THz transmission for variable substrate temperature for NW sample Ge-20 fitted with the photoexcited carrier density model. (b) Maximum absolute value of differential THz transmission as a function of the substrate temperature for NW sample Ge-20.

The values of the extracted parameters as a function of substrate temperature for NW sample Ge-20 are summarized in Figure 3.2.10. We observe that the intraband

relaxation time is completely independent of the substrate temperature [23]. On the other hand, the mean interband recombination time exhibits a slight, but pronounced monotonic decrease with the substrate temperature. We attribute this to partial filling of the surface defect states as the substrate temperature is lowered, which decreases the surface recombination efficiency and enhances the photoexcited carrier lifetimes. At the same time, as the surface defect states are filled, the NWs appear more uniform and the heterogeneity parameter approaches unity.

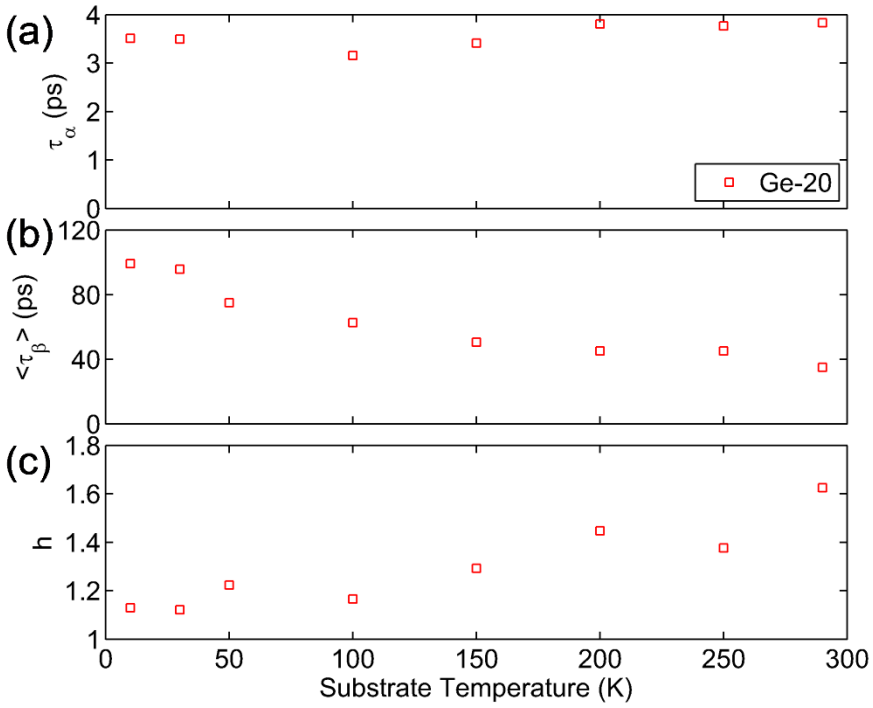

Figure 3.2.10 – (a) Intraband relaxation time, (b) mean interband recombination time and (c) heterogeneity parameter extracted from the photoexcited carrier density model fits as a function of the substrate temperature for NW sample Ge-20.

Section 3.3 Dynamic THz Response

In this section, we discuss the full dynamic THz response of the NWs following ultrafast photoexcitation and its physical origins. We consider three possible contributions including bulk free-carrier response, bulk exciton response and quantum confinement effects.

In Section 3.2, we applied purely electromagnetic analysis to relate the differential THz transmission (an experimental quantity that we can measure) to the photoinduced THz

conductivity of the NWs (a physical quantity that we are interested in). However, the photoinduced THz conductivity is a macroscopic quantity, which is useful from an engineering point of view for the design and development of practical NW-based devices, but it cannot by itself explain the microscopic origins of the dynamic THz response of the NWs. To answer this question, we need a physical model for the photoinduced THz conductivity (or THz absorption).

In this section, as a second experimental approach, we try to determine the true physics governing the dynamic THz response of the NWs by measuring the full time-domain differential change in the THz probe pulse transmission through the NW samples due to photoexcitation by the optical pump pulse, which we then normalize to the THz transmission in the absence of photoexcitation, $\Delta t/t$. To gain physical insight we vary a large set of parameters including the pump fluence, the substrate temperature, the pump-probe delay, the NW core diameter and the NW composition with or without a shell. Figure 3.3.1 shows the full time-domain normalized differential THz transmission $\Delta t/t$ for variable pump fluence measured for NW sample Ge-10/Si-2, which is representative for all NW samples. Just as before, we observe that the differential THz transmission at the peak of the THz probe pulse is negative, which corresponds to an increased THz absorption or an increased THz conductivity upon photoexcitation.

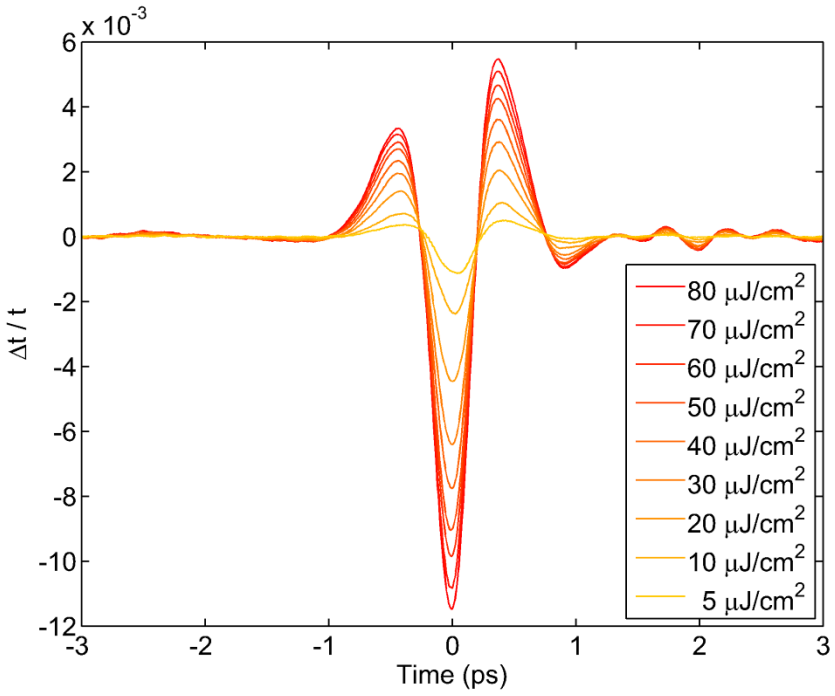

Figure 3.3.1 – Differential THz transmission waveform for variable pump fluence for NW sample Ge-10/Si-2.

From the measured time-domain differential THz electric field, $\Delta t/t$, we can obtain the frequency-domain differential THz spectrum, $\Delta t(\omega)/t(\omega)$, by straightforward numerical Fourier transformation. Then, for the NW arrays, we are justified to use the Tinkham formula [4] to relate the differential THz transmission to the photoinduced THz sheet conductivity of the NWs via:

$$\Delta\sigma(\omega) \approx -\frac{n_{sub}+n_{air}}{\eta_0} \times \frac{\Delta t(\omega)}{t(\omega)}, \tag{3.3.1}$$

where n_{sub} and n_{air} are the THz refractive indices of the substrate and the environment, respectively, and η_0 is the impedance of free space. This is the exact same result we reached in Equation 3.2.2. If we further ignore the frequency dispersion in the THz range of n_{sub}, we obtain even simpler linear relationship:

$$\Delta\sigma(\omega) \sim -\frac{\Delta t(\omega)}{t(\omega)}. \tag{3.3.2}$$

The photoinduced change in the THz conductivity is naturally given by the difference between the THz conductivity with (pump on) and without (pump off) photoexcitation,

$\Delta\sigma(\omega) = \sigma_{on}(\omega) - \sigma_{off}(\omega)$. In some cases, including very small intrinsic conductivities or strong pumping, the photoexcited THz conductivity can be approximated by the THz conductivity with photoexcitation, $\Delta\sigma(\omega) \approx \sigma_{on}(\omega)$. For simplicity of the discussion, we will use the notation with the differential, unless the approximation is not valid.

In the rest of this section, we consider in detail three possible physical origins giving rise to the photoinduced THz conductivity (or THz absorption), including bulk free-carrier response, bulk exciton response and quantum confinement effects.

Section 3.3.1 Bulk Free-Carrier Response

In this section, we consider a bulk free-carrier model for the dynamic THz response of the NWs. The basic argument is that the THz probe is absorbed by free carriers injected by the optical pump. This is the same general idea as in the photoexcited carrier density model from Section 3.2. However, we will expand the photoexcited carrier density model by including the frequency information in the measured differential THz transmission spectrum.

First, we study the dependence of the dynamic THz response of the NWs on the pump fluence (or the photoexcited carrier density). Figure 3.3.2 shows the normalized differential THz transmission spectrum $\Delta t(\omega)/t(\omega)$ for variable pump fluence measured for NW sample Ge-10/Si-2. The result is obtained from the raw data in Figure 3.3.1. Because the Fourier transformation of a real waveform gives a complex frequency spectrum, we consider both the real and the imaginary part as shown in Figure 3.3.2. It is very important to note that the real part peaks at a finite frequency and the imaginary part changes sign close to the same frequency.

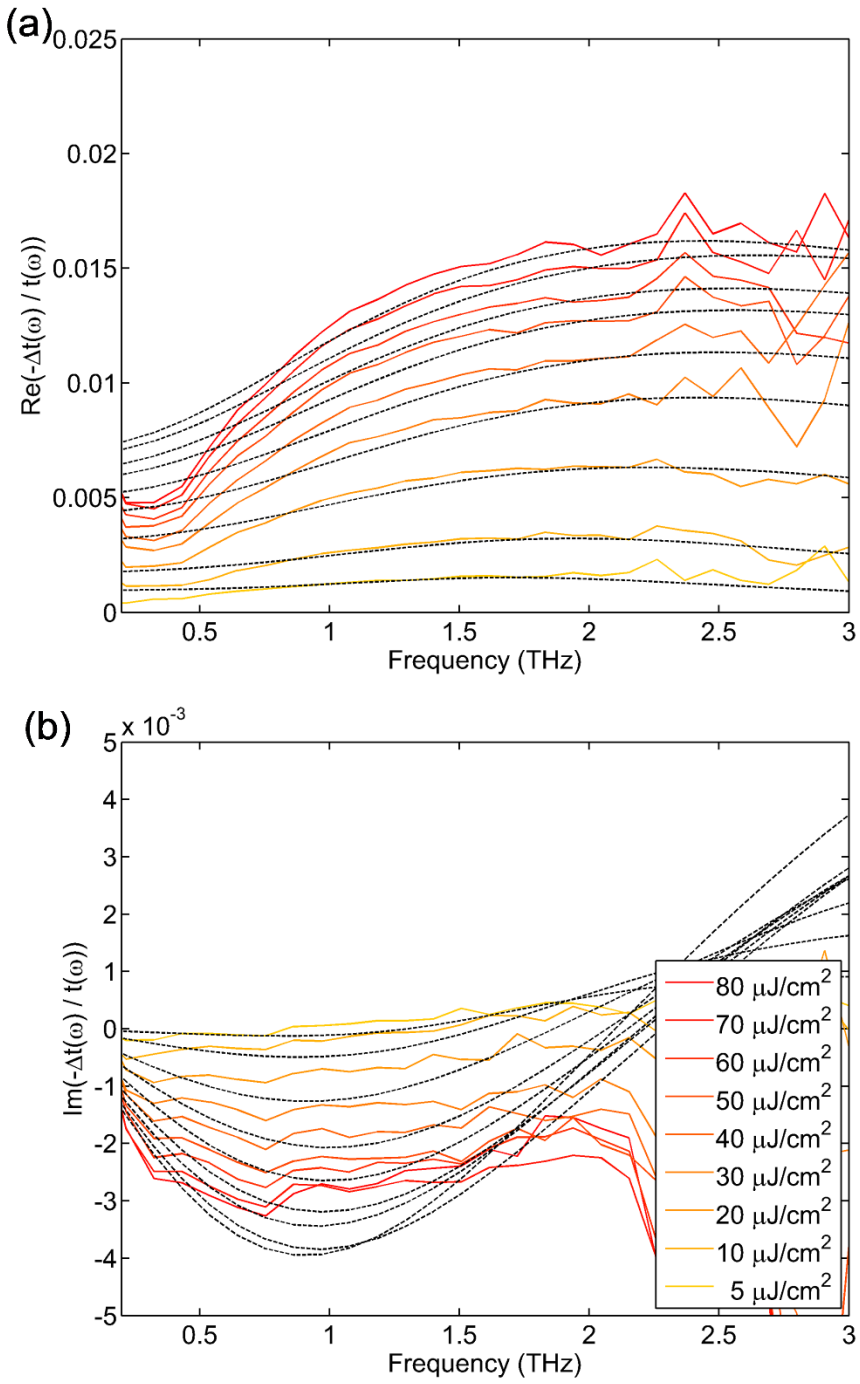

Figure 3.3.2 – (a) Real and (b) imaginary part of differential THz transmission spectrum for variable pump fluence for NW sample Ge-10/Si-2 fitted with the Drude-Plasmon model.

Perhaps, the simplest bulk free-carrier absorption response is the well-known Drude model given by:

$$\Delta\sigma(\omega) = \frac{\Delta\sigma_0}{1-i\omega\tau} = \frac{\Delta n e^2 \tau/m^*}{1-i\omega\tau}, \qquad (3.3.3)$$

where Δn is the photoexcited carrier density, τ is the carrier momentum scattering time, m^* is the effective carrier mass and e is the elementary charge. The Drude model has been found to be consistent with the THz response of many bulk semiconductors, including Ge and Si [24, 25, 26]. In stark contrast to the experiment, the real part of the Drude model peaks at zero frequency and the imaginary part has no sign change, which shows that it does not describe the dynamic THz response of the NWs. A number of empirical extensions to the simple Drude formula have been proposed in the literature to try to explain experimental data on a wide variety of nanostructured semiconductor systems, including nanorods, nanowires, nanoparticles, etc., that does not match the Drude model [27]. Some of the most prominent are summarized in Table 3.3.1 and include the Plasmon (Lorentz oscillator) model [7, 28, 29, 30, 31, 32, 33, 34], the Cole-Cole model [35], the Cole-Davidson model [36, 37], the Generalized Drude model [38] (also known as the Havriliak-Negami expression [39]) and the Drude-Smith model [40, 41, 42, 43, 44, 45, 46]. It is important to realize that all these generalizations of the Drude model are purely phenomenological, although most of them have some physical justifications. We will consider two such models, the Drude-Plasmon and the Drude-Smith, to try to explain the dynamic THz response of the NWs.

Table 3.3.1 – Drude-like THz conductivity models.

Name	Formula
Drude model	$\Delta\sigma(\omega) = \frac{\Delta\sigma_0}{1 - i\omega\tau}$
Plasmon (Lorentz oscillator) model	$\Delta\sigma(\omega) = \frac{\Delta\sigma_0}{1 - i\omega\tau(1 - \omega_0^2/\omega^2)}$
Cole-Cole model	$\Delta\sigma(\omega) = \frac{\Delta\sigma_0}{1 - (i\omega\tau)^{1-\alpha}}$
Cole-Davidson model	$\Delta\sigma(\omega) = \frac{\Delta\sigma_0}{(1 - i\omega\tau)^{\beta}}$
Generalized Drude model	$\Delta\sigma(\omega) = \frac{\Delta\sigma_0}{(1 - (i\omega\tau)^{1-\alpha})^{\beta}}$

Drude-Smith model	$\Delta\sigma(\omega) = \frac{\Delta\sigma_0}{1 - i\omega\tau}\left(1 + \sum_{n=1}^{\infty} \frac{c_n}{(1 - i\omega\tau)^n}\right)$

First, we consider the Drude-Plasmon model. One extension to the Drude model is the Plasmon (Lorentz oscillator) model which is given by:

$$\Delta\sigma(\omega) = \frac{\Delta\sigma_0}{1-i\omega\tau(1-\omega_0^2/\omega^2)} = \frac{\Delta n e^2\tau/m^*}{1-i\omega\tau(1-\omega_0^2/\omega^2)}. \quad (3.3.4)$$

The implicit assumption is that the system under study is much smaller than the wavelength of the radiation, which applies for the NWs. This leads to a plasmon resonance oscillation at a frequency ω_0, which is qualitatively very similar to a Lorentz-like resonance oscillation. In the most common case of a spherical particle the plasmon resonance frequency $\omega_0 = \omega_P/\sqrt{3}$, where $\omega_P = \sqrt{ne^2/\epsilon m^*}$ is the bulk plasma frequency. To describe the dynamic THz response of the NWs, we present the photoinduced THz conductivity as a linear combination of a Drude-like and a surface-plasmon-resonance-like (Plasmon-like) contribution:

$$\Delta\sigma(\omega) = \Delta\sigma_D(\omega) + \Delta\sigma_P(\omega) = \frac{\Delta\sigma_{D0}}{1-i\omega\tau} + \frac{\Delta\sigma_{P0}}{1-i\omega\tau(1-\Omega_P^2/\omega^2)} = \frac{\Delta n_D e^2\tau/m^*}{1-i\omega\tau} + \frac{\Delta n_P e^2\tau/m^*}{1-i\omega\tau(1-\Omega_P^2/\omega^2)}, \quad (3.3.5)$$

where Δn_D and Δn_P are the photoexcited carrier densities in the Drude-like and the Plasmon-like mode, respectively, Ω_P is the surface plasmon resonance frequency, τ is the carrier momentum scattering time (assumed the same for both modes), m^* is the effective carrier mass and e is the elementary charge. The total photoexcited carrier density is $\Delta n = \Delta n_D + \Delta n_P$ and appears in the photoexcited carrier density model in Section 3.2. The surface plasmon resonance frequency Ω_P is related to the bulk plasma frequency ω_P by $\Omega_P = \sqrt{f} \times \omega_P = \sqrt{f n_P e^2/\epsilon m^*}$, where f is a geometrical factor [47] ($f = 1/2$ in the case of a cylinder for our experimental configuration) and ε is the THz electric permittivity of the NWs. Finally, the carrier mobility, μ, which is the NW material parameter of main practical interest, can be calculated using $\mu = e\tau/m^*$.

Using the Drude-Plasmon model, we produce excellent fits to both the real and the imaginary part of the differential THz transmission spectrum for NW sample Ge-10/Si-2, as shown in Figure 3.3.2. The small deviation between the experiment and the model observed for frequencies below ~0.5 THz is attributed to the frequency dependence of the THz probe spot, which becomes comparable to the optical pump spot at lower THz frequencies. It is important to note that neither a pure Drude-like nor a pure Plasmon-like mode alone can yield satisfactory fits. We perform identical measurements and analysis on NW sample Ge-10 (not shown).

The values of the various parameters, extracted from the fits to the Drude-Plasmon model, as a function of pump fluence for NW samples Ge-10 and Ge-10/Si-2 are summarized in Figure 3.3.3. We observe slight pump fluence, F, dependence of the momentum scattering time for both Ge and Ge/Si NWs that can be well described by the same exponential function $a \times exp(-bF) + c$, which was applied to the THz carrier dynamics in Section 3.2. As we argued there, with increasing pump fluence, the electrons more strongly screen the negative surface field and have a higher probability to reach the surface, where the recombination and scattering are enhanced. Thus, carrier screening of surface defects may account for the weak photoexcited carrier density dependence of both carrier recombination and scattering. Because the Ge/Si NWs have a larger surface defect density than the Ge NWs, the momentum scattering time in the former is lower than that in the latter at high pump fluence. The values become comparable at very low pump fluence, when carrier screening is at its minimum and surface scattering is suppressed.

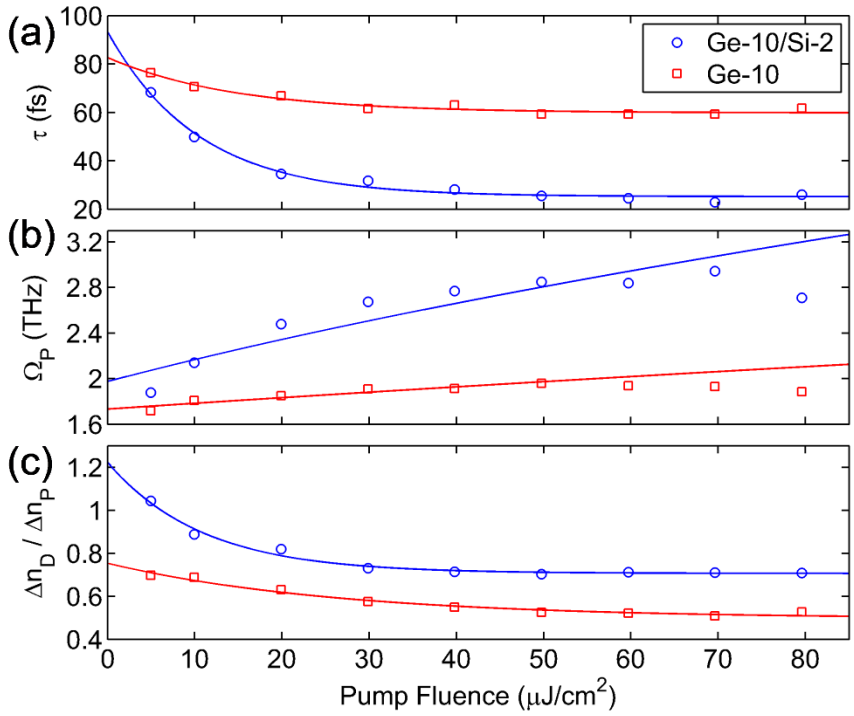

Figure 3.3.3 – (a) Carrier momentum scattering time, (b) surface plasmon resonance frequency and (c) Drude-like to Plasmon-like mode ratio extracted from the Drude-Plasmon model fits as a function of the pump fluence for NW samples Ge-10 and Ge-10/Si-2.

In the Drude-Plasmon model, the existence of a built-in surface field can also be thought of as the physical origin of the two different modes in the photoinduced THz conductivity, Drude-like and Plasmon-like. This is supported by the pump fluence dependence of their relative contribution given by the ratio $\Delta n_D/\Delta n_P$, which also can be well described by the same exponential function $a \times exp(-bF) + c$. As the surface field is more effectively screened at high pump fluence and more photoexcited carriers reach the surface, Δn_P increases relative to Δn_D. Figure 3.3.3 also shows a near square root increase of the surface plasmon resonance frequency with photoexcited carrier density in both NW samples as predicted from theory. Based on the fits to the plasmon frequency and to the ratio $\Delta n_D/\Delta n_P$ near zero pump fluence, we estimate a background carrier density on the order of ~10^{16} cm^{-3} as anticipated for undoped NWs.

Second, we consider the Drude-Smith model. The dynamic THz response of the NWs can also be described by another extension to the Drude model, which was first proposed by Smith [40] and is usually referred to as the Drude-Smith model. The implicit assumption is that in the system under study the carriers undergo strong backscattering,

which again applies for the NWs due to their large surface. In the Drude-Smith framework, the photoinduced THz conductivity is given by:

$$\Delta\sigma(\omega) = \frac{\Delta\sigma_0}{1-i\omega\tau}\left(1 + \sum_{n=1}^{\infty}\frac{c_n}{(1-i\omega\tau)^n}\right) = \frac{\Delta n e^2\tau/m^*}{1-i\omega\tau}\left(1 + \sum_{n=1}^{\infty}\frac{c_n}{(1-i\omega\tau)^n}\right), \quad (3.3.6)$$

where Δn is the photoexcited carrier density, τ is the carrier momentum scattering time, c_n are the coefficients characterizing the carrier persistence of velocity, m^* is the effective carrier mass and e is the elementary charge. Every coefficient c_n represents the fraction of the original carrier velocity which is retained after the nth collision. Under the assumption that the carrier velocity is retained for only one collision, the photoinduced THz conductivity reduces to:

$$\Delta\sigma(\omega) = \frac{\Delta\sigma_0}{1-i\omega\tau}\left(1 + \frac{c}{1-i\omega\tau}\right) = \frac{\Delta n e^2\tau/m^*}{1-i\omega\tau}\left(1 + \frac{c}{1-i\omega\tau}\right). \quad (3.3.7)$$

Negative values for the parameter c $(-1 \leq c < 0)$ indicate a predominance of carrier backscattering. Due to the carrier backscattering, the effective carrier momentum scattering time, which is related to the transport properties of the NWs, is $\tau_c = \tau/(1-c)$. Finally, the carrier mobility, μ, which is the NW material parameter of main practical interest, can be calculated using $\mu = e\tau_c/m^*$.

Using the Drude-Smith model, we produce excellent fits to both the real and the imaginary part of the differential THz transmission spectrum for NW sample Ge-10/Si-2, as shown in Figure 3.3.4. The small deviation between the experiment and the model observed for frequencies below ~0.5 THz is again attributed to the frequency dependence of the THz probe spot, which becomes comparable to the optical pump spot at lower THz frequencies. It is worth mentioning that the shapes of the fits with the Drude-Plasmon and the Drude-Smith model appear very similar. We perform identical analysis on NW sample Ge-10 (not shown).

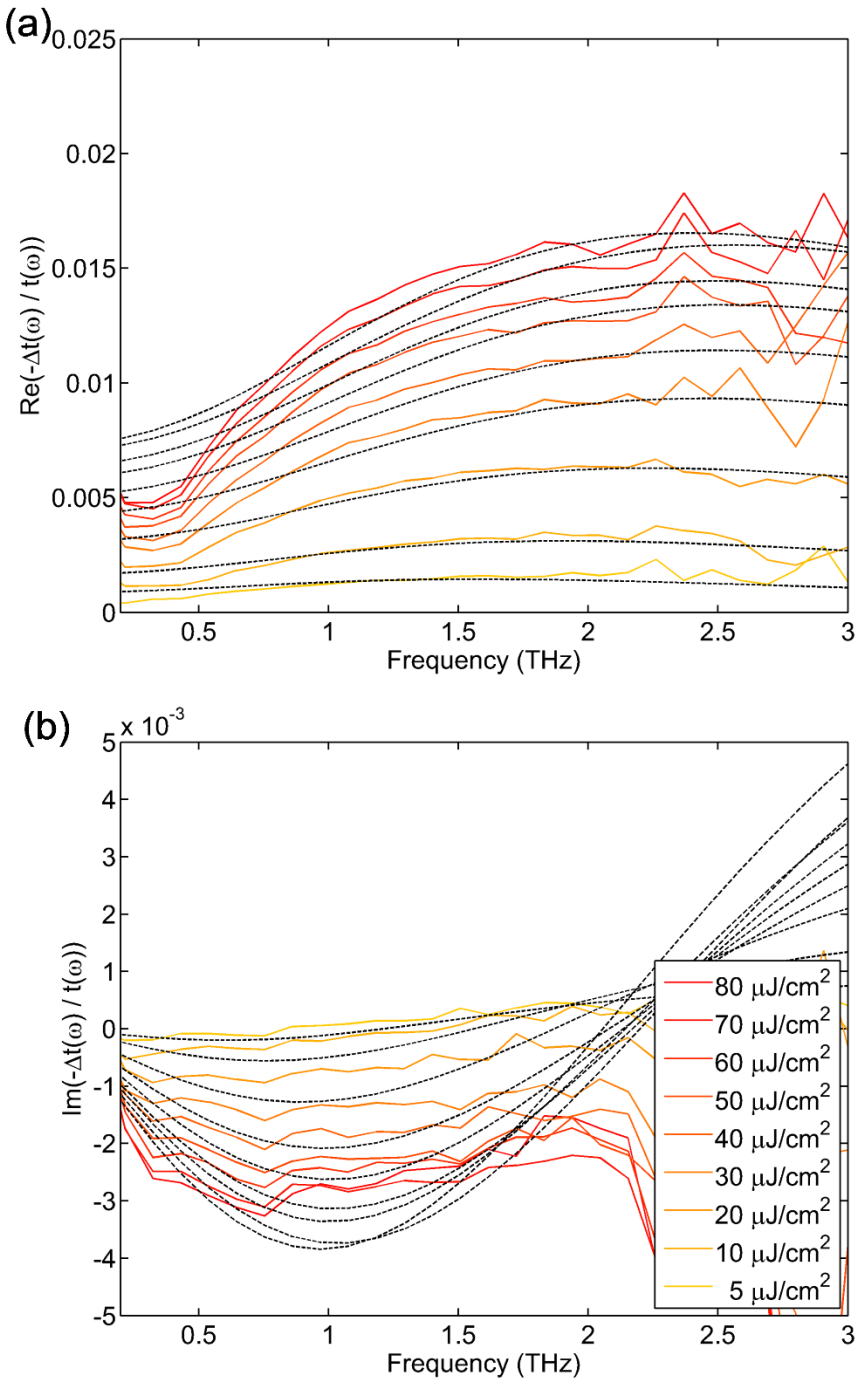

Figure 3.3.4 – (a) Real and (b) imaginary part of differential THz transmission spectrum for variable pump fluence for NW sample Ge-10/Si-2 fitted with the Drude-Smith model.

The values of the various parameters, extracted from the fits to the Drude-Smith model, as a function of pump fluence for NW samples Ge-10 and Ge-10/Si-2 are summarized in Figure 3.3.5. There are some clear similarities between the results for the

Drude-Plasmon and the Drude-Smith model, so that some conclusions are the same for both models. The values of the momentum scattering time for the two models agree to within a factor of ~2. The values of the parameter c are largely negative indicating strong backscattering from the surface defects. In the Drude-Smith model, the pump fluence dependence of both the momentum scattering time and the parameter c can be well described by the same exponential function $a \times exp(-bF) + c$, which was applied in the Drude-Plasmon model. As the surface field is more effectively screened at high pump fluence and more photoexcited carriers reach the surface, τ_c decreases and c becomes more negative, because surface scattering is dominant. In that sense, c in the Drude-Smith model resembles $\Delta n_D/\Delta n_P$ in the Drude-Plasmon. Similarly, because the Ge/Si NWs have a larger surface defect density than the Ge NWs, the momentum scattering time in the former is lower than that in the latter at high pump fluence.

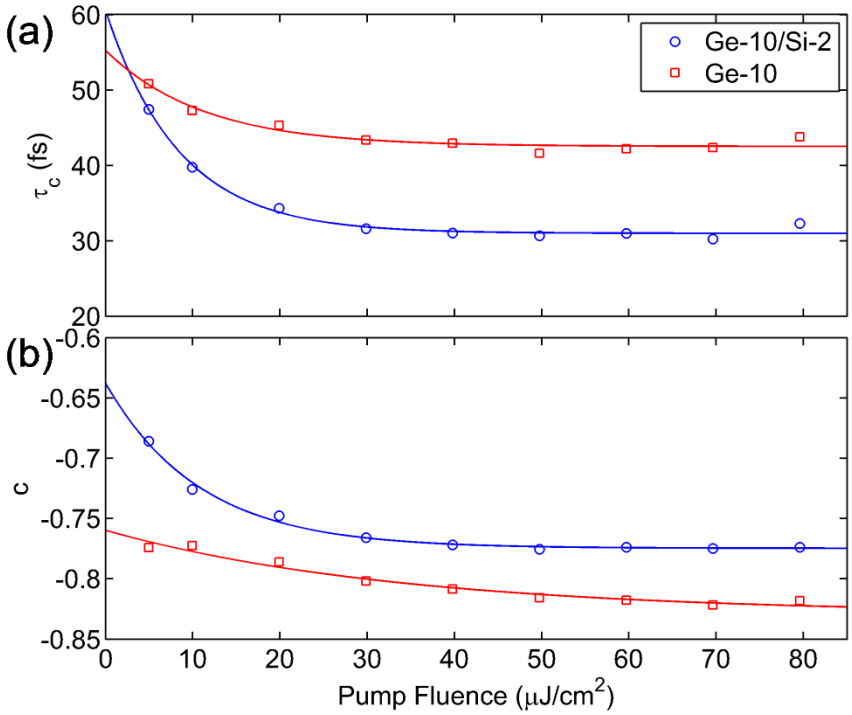

Figure 3.3.5 – (a) Carrier momentum scattering time and (b) carrier persistence of velocity parameter extracted from the Drude-Smith model fits as a function of the pump fluence for NW samples Ge-10 and Ge-10/Si-2.

Next, we study the dependence of the dynamic THz response of the NWs on the NW core diameter (or the NW volume-to-surface-area ratio). We measure the normalized differential THz transmission spectrum $\Delta t(\omega)/t(\omega)$ for NW samples with Ge core

diameters of ~10, ~20 and ~40 nm both with and without a Si shell at a fixed pump fluence of 60 $\mu J/cm^2$. The real and the imaginary part of the experimental data together with both the Drude-Plasmon and the Drude-Smith model fits is shown in Figure 3.3.6. It is again very clear that the shapes of the fits with the two models appear very similar. Purely mathematically, this can be attributed to the fact that the two models have similar functional forms and generate similar family of curves. It is very important to note, however, that the physics behind the Drude-Plasmon and the Drude-Smith model is very different.

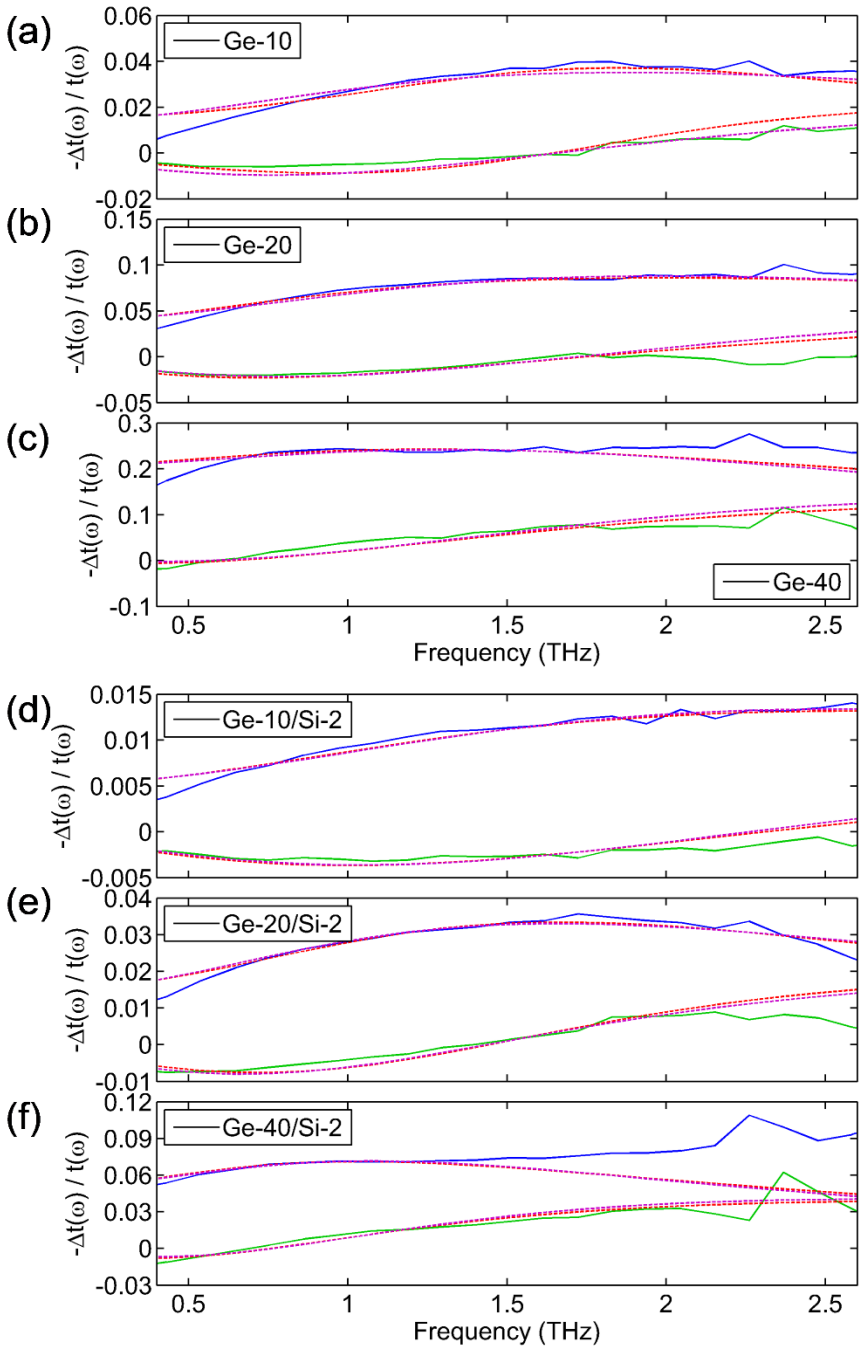

Figure 3.3.6 – Real (blue) and imaginary (green) part of differential THz transmission spectrum for (a-c) Ge and (d-f) Ge/Si NWs fitted with the Drude-Plasmon (red) and the Drude-Smith (magenta) model.

The values of the various parameters, extracted from the fits to the Drude-Plasmon model, for all NW samples are summarized in Figure 3.3.7. We observe that the momentum scattering time for both Ge and Ge/Si NWs (except NW sample Ge-10) increases with the NW core diameter (or the NW volume-to-surface-area ratio), because scattering from

surface defects diminishes. This conclusion is further supported by a similar trend in the ratio $\Delta n_D/\Delta n_P$, which indicates that the Drude-like and Plasmon-like modes dominate in thicker and thinner NWs, respectively. In accord, the plasmon frequency, which is directly proportional to the square root of the carrier density in the Plasmon-like mode decreases with core diameter. We also observe that for NW core diameters of 20 and 40 nm, the Si shell increases the momentum scattering time by ~50-60%, which is attributed to stronger carrier confinement near the center of the Ge core and away from surface defects.

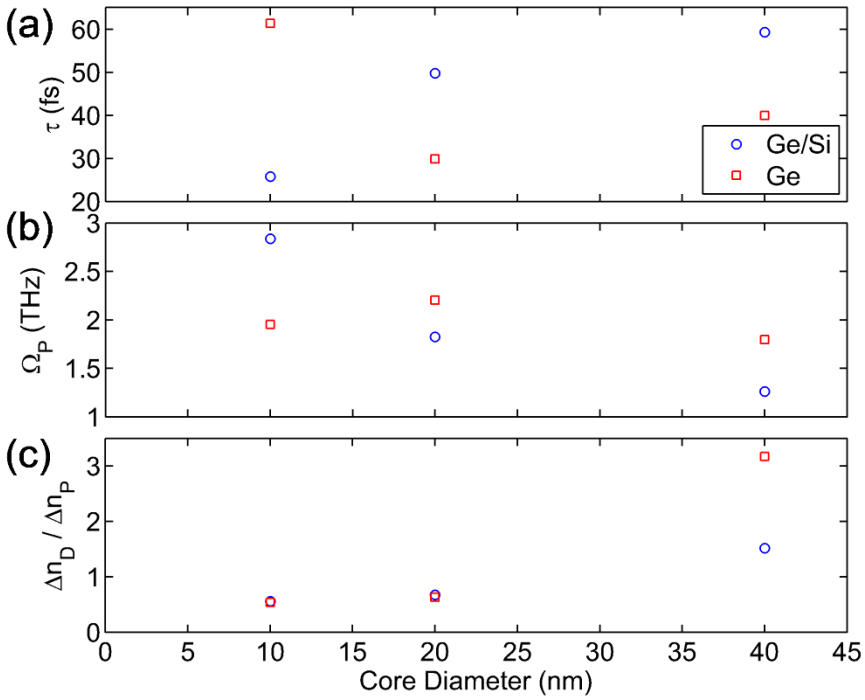

Figure 3.3.7 – (a) Carrier momentum scattering time, (b) surface plasmon resonance frequency and (c) Drude-like to Plasmon-like mode ratio extracted from the Drude-Plasmon model fits as a function of the NW core diameter for Ge and Ge/Si NWs.

NW sample Ge-10 apparently deviates from the rest. We expect that quantum confinement effects become important, when the NW core diameter is reduced to ~10 nm [48, 49, 50, 51] and begin to compete with the carrier confinement effects due to the Si shell. Also, because surface scattering is particularly strong for the smallest NW core diameters and the surface defect density for NW sample Ge-10/Si-2 is significantly larger than that for Ge-10, the former has a lower momentum scattering time. These results suggest that the deposition of a Si shell on Ge NWs can enhance the momentum scattering

times, but the scaling of this effect to NWs thinner than ~10 nm requires further improvement in the Ge/Si core/shell interface quality and/or the Si shell crystallinity.

The values of the various parameters, extracted from the fits to the Drude-Smith model, for all NW samples are summarized in Figure 3.3.8. There are again some clear similarities between the results for the Drude-Plasmon and the Drude-Smith model, so that some conclusions are the same for both models. The values of the momentum scattering time of the different NW samples for the two models agree to within a factor of ~2. The values of the parameter c of all NW samples are largely negative indicating strong backscattering from the surface defects. We observe that for both Ge and Ge/Si NWs (except NW sample Ge-10) the momentum scattering time increases and the parameter c becomes less negative with increasing the NW core diameter (or the NW volume-to-surface-area ratio), because scattering from surface defects diminishes. As we mentioned before, c in the Drude-Smith model resembles $\Delta n_D/\Delta n_P$ in the Drude-Plasmon. Similarly, we observe that for NW core diameters of 20 and 40 nm, the Si shell increases the momentum scattering time by ~50-60%, which is attributed to stronger carrier confinement near the center of the Ge core and away from surface defects. Similarly, NW sample Ge-10 apparently deviates from the rest, because we expect that quantum confinement effects begin to compete with the carrier confinement effects due to the Si shell for NW core diameter of ~10 nm [48, 49, 50, 51], and the Si shell reduces the momentum scattering time due to stronger surface scattering at the rougher Ge/Si interface.

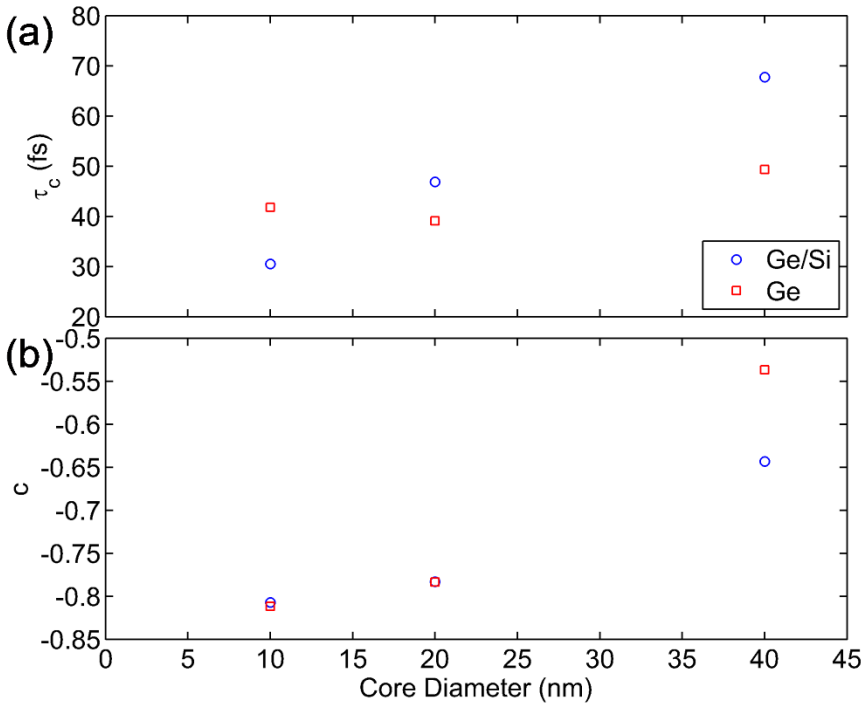

Figure 3.3.8 – (a) Carrier momentum scattering time and (b) carrier persistence of velocity parameter extracted from the Drude-Smith model fits as a function of the NW core diameter for Ge and Ge/Si NWs.

It is also informative and useful to calculate a few other device-relevant NW material parameters and to compare them to the values in bulk Ge. In these calculations, we use the values of the momentum scattering time extracted from fits to the Drude-Plasmon model as an illustration, but the calculations for the Drude-Smith model are analogous. The various calculated parameters for all NW samples are summarized in Table 3.3.2. The carrier mobility μ is obtained from $\mu = e\tau/m^*$ (using an average electron-hole conductivity effective mass of $m^* = 0.153m_0$ [24, 52]). The calculated mobilities for all NW samples are lower than the average of the electron and hole mobilities in bulk Ge of 2900 cm^2/(V·s) [24, 52] due to the additional surface scattering in the NW geometry. The mean free path l is obtained from $l = v_{th}\tau$ (using a thermal velocity of v_{th} = 3 × 10^5 m/s at room temperature). The calculated mean free path is comparable to the NW core diameter, which supports the claim for ballistic carrier transport and indicates that the photoexcited carriers bounce off the NW walls many times before they get trapped at a surface recombination center. The diffusion coefficient D is obtained from the Einstein relation $D/\mu = k_BT/e$. When we substitute the calculated diffusion coefficient into Equation 3.2.6, we confirm our assumption for the THz carrier dynamics that the diffusion

term is much smaller than the surface recombination term. A corresponding longitudinal diffusion length L, which is a measure of carrier diffusion along the NW, is obtained from $L = \sqrt{D\langle\tau_\beta\rangle}$.

Table 3.3.2 – Carrier transport parameters of Ge NWs, Ge/Si NWs and bulk Ge.

Core diameter (nm)	Ge NWs			
	μ (cm^2/(V·s))	D (cm^2/s)	L (nm)	l (nm)
10	706	18	366	18
20	344	9	392	9
40	460	12	678	12

Core diameter (nm)	Ge/Si core/shell NWs			
	μ (cm^2/(V·s))	D (cm^2/s)	L (nm)	l (nm)
10	297	8	79	8
20	573	15	152	15
40	683	18	220	18

Bulk Ge				
Carrier type	μ (cm^2/(V·s))	D (cm^2/s)	L (nm)	l (nm)
electron	3900	100	N/A	100
hole	1900	50	N/A	50

Section 3.3.2 Bulk Exciton Response

In this section, we consider a bulk exciton model for the dynamic THz response of the NWs. The basic argument is that the THz probe is absorbed by electron-hole correlations (or excitons) formed after photoexcitation by the optical pump.

In Section 3.3.1, we discussed how a bulk free-carrier model can account for the dynamic THz response of the NWs. We considered two types of bulk free-carrier response,

given by the Drude-Plasmon and the Drude-Smith models, and how they agree with the measured differential THz transmission spectrum of the NWs. However, it is very important to note that any bulk free-carrier model fails to explain why there exists a finite, instead of quasi-instantaneous (limited only by the temporal resolution of the THz spectroscopy measurement), rise time to the THz absorption of the NWs. It can be expected that as soon as free carriers are injected into the NW system, they can absorb the THz radiation. The assumption that the rise time is related to intraband carrier relaxation is not completely justified. Both electrons and holes are initially photoexcited near the Γ point. Due to efficient intervalley and intravalley phonon scattering, the hot electrons relax to the bottom of the conduction band in the L valley, while the hot holes relax to the top of the valence band in the Γ valley. Because the Γ valley has a much smaller effective electron mass than the lowest L valley, THz absorption by the electrons is expected to be larger in the Γ valley than in the L valley. At the same time, THz absorption by the holes is not expected to change substantially as they relax within the L valley. We note that the experimental data is not consistent with these expectation, which suggests that something is missing in the physical model.

In this section, we consider if the finite rise time to the THz absorption of the NWs is consistent with the built-up of electron-hole correlations (or excitons) after photoexcitation by the optical pump. To test this idea, we study the dependence of the dynamic THz response of the NWs on the substrate temperature. Figure 3.3.9(a) and (b) show the normalized differential THz transmission spectrum $\Delta t(\omega)/t(\omega)$ at a substrate temperature of 300 K and 10 K, respectively, for variable pump-probe delay at a fixed pump fluence of 60 μJ/cm^2 measured for NW sample Ge-20. For clarity, only the real part is presented. We observe that the width of the resonance-like shape, which is observed at a finite frequency in the measured differential THz transmission spectrum for all NW samples, slightly narrows down at cryogenic temperatures. The magnitude of the differential THz transmission decreases with increasing pump-probe delay as the photoexcited carriers recombine, which is qualitatively similar to decreasing the pump fluence (or the initial photoexcited carrier density). We also note that the peak position of the resonance-like shape remains almost constant at the frequency of ~1 THz (≈ 48 K).

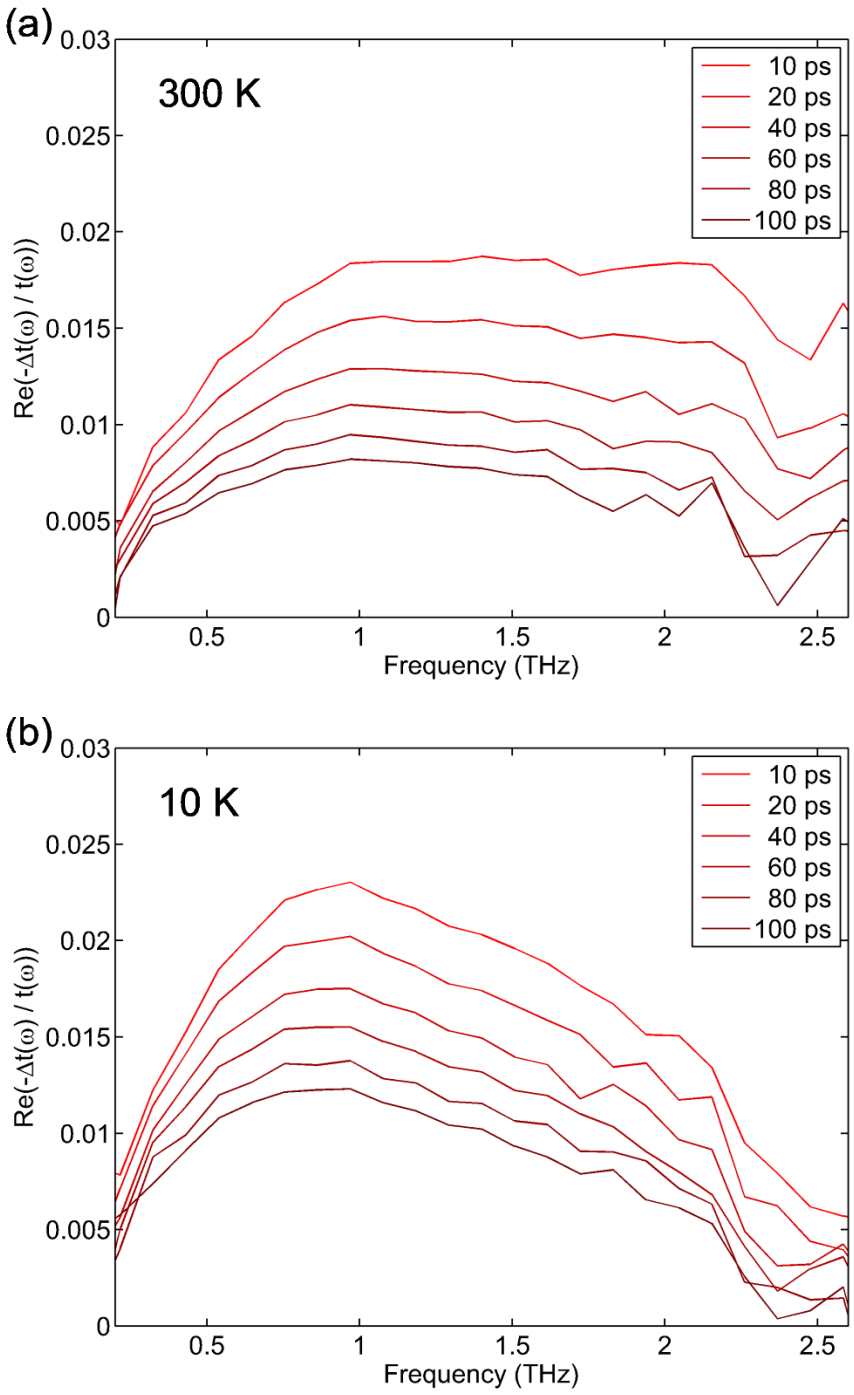

Figure 3.3.9 – Real part of differential THz transmission spectrum for variable pump-probe delay at a substrate temperature of (a) 300 K and (b) 10 K for NW sample Ge-20.

The dynamic THz response arising from electron-hole correlations has been extensively theoretically studied in direct bandgap semiconductors such as GaAs [53, 54, 55]. It has also been experimentally observed at cryogenic temperatures in very high

quality GaAs multi-quantum wells [56, 57], bulk Cu_2O [58] and bulk Si [59]. Very low temperatures are essential for excitons with binding energies in the THz range to prevent them from disassociating into free uncorrelated electrons and holes. The excitonic response is characterized by a narrow non-symmetric resonance-like shape, which peaks at the frequency corresponding to the 1s-to-2p transition energy, E_{1s-2p}, of the exciton. This shape is strikingly similar to the dynamic THz response of the NWs measured at a substrate temperature of 10 K. Both direct and indirect excitons have also been extensively theoretically studied in indirect bandgap semiconductors such as Ge and Si [60, 61, 62, 63, 64]. In bulk Ge, the 1s-to-2p transition energy E_{1s-2p} of the indirect exciton, in which the electron is in the L valley and the hole is in the Γ valley, corresponds to ~1 THz (≈ 48 K), which is again consistent with the measured dynamic THz response of the NWs. Hence, within the exciton model, the dynamic THz response of the NWs is attributed to the indirect excitonic response of bulk Ge. The finite rise time to the THz absorption arises from the gradual formation of electron-hole correlations between the photoexcited electrons as they scatter to the L valley, and the photoexcited holes as they relax in the Γ valley.

To find the exciton wavefunctions and energies, we solve the Wannier equation for an indirect exciton in the zero-density limit, which is given by:

$$E_\lambda \phi_\lambda(\boldsymbol{k}) = \varepsilon_{\boldsymbol{k}} \phi_\lambda(\boldsymbol{k}) - \sum_{\boldsymbol{k}'} V_{\boldsymbol{k}-\boldsymbol{k}'} \phi_\lambda(\boldsymbol{k}'), \tag{3.3.8}$$

where $\lambda = \{n, l, m\}$ is the full set of quantum numbers. The linear THz absorption spectrum of the excitonic transitions follows from the THz-Elliott formula [55]:

$$\alpha(\omega) = Im\left[\sum_{\lambda,\nu} \frac{S^{\lambda,\nu}(\omega)\Delta n_{\lambda,\nu}^{(0)} - \left(S^{\lambda,\nu}(-\omega)\Delta n_{\lambda,\nu}^{(0)}\right)^*}{\epsilon_0 \epsilon_r c\omega\left(\hbar\omega + i\gamma_J\right)}\right]. \tag{3.3.9}$$

The response function is defined by:

$$S^{\lambda,\nu}(\omega) = \sum_\beta \frac{E_\beta - E_\lambda}{E_\beta - E_\lambda - \hbar\omega - i\gamma_J} J_{\lambda,\beta} J_{\beta,\nu}, \tag{3.3.10}$$

where the transition matrix element between two states is given by:

$$J_{\lambda,\nu} = \sum_{\boldsymbol{k}} \psi_\lambda(\boldsymbol{k}) \left(\frac{-e\hbar k\, cos(\vartheta)}{\mu_z}\right) \psi_\nu(\boldsymbol{k}). \tag{3.3.11}$$

We numerically calculate the wavefunctions and energies of the indirect exciton in bulk Ge and its THz response. Figure 3.3.10 shows a comparison between the experimental THz response measured for NW sample Ge-20 at a substrate temperature of 10 K and the theoretical THz response calculated for bulk Ge. We observe that experiment and theory are in very good agreement. The THz frequencies corresponding to the 1s-to-2p transition energy E_{1s-2p} and the exciton binding energy $E_{1s-continuum}$ of the indirect exciton are also indicated. We confirm that both E_{1s-2p} and $E_{1s-continuum}$ are near ~1 THz (≈ 48 K), where the THz response peaks, as expected. However, the bulk exciton model cannot account for the dynamic THz response of the NWs at temperatures close to room temperature of 300 K, because all excitons are expected to be completely dissociated into free uncorrelated electrons and holes.

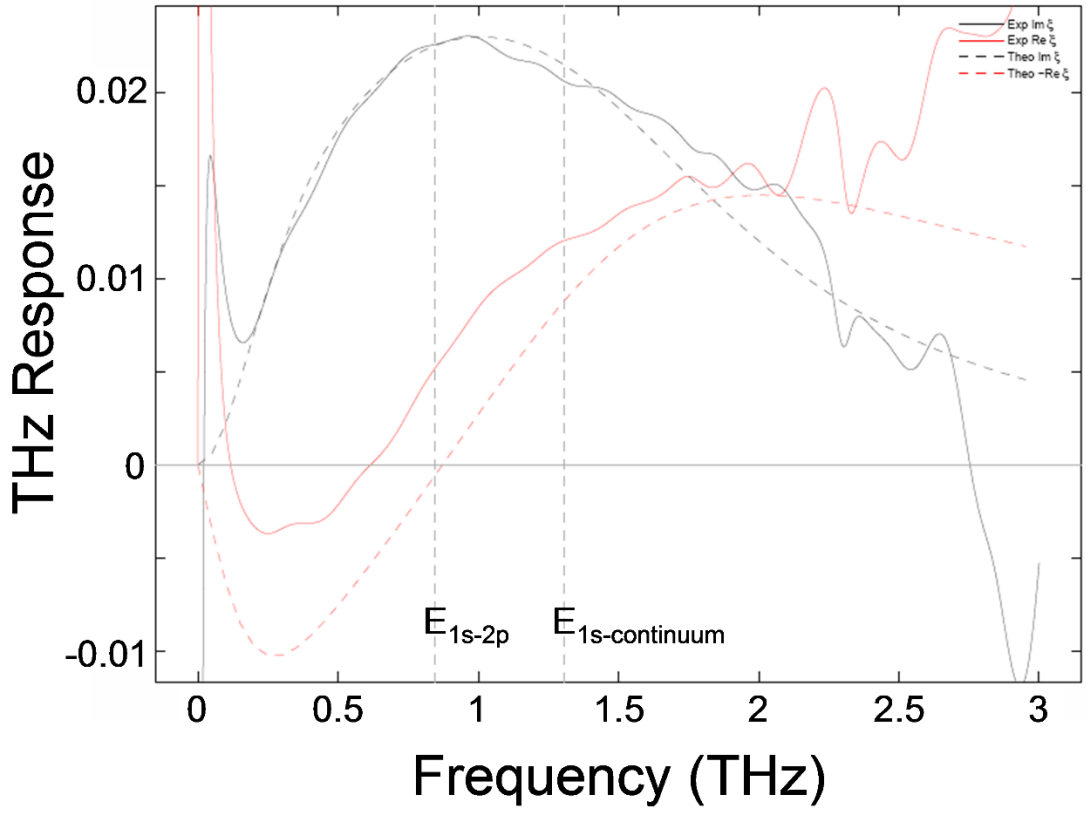

Figure 3.3.10 – Comparison between experimental THz response (solid lines) measured for NW sample Ge-20 at a substrate temperature of 10 K and theoretical THz response (dashed lines) calculated for an indirect excitonic transition in bulk Ge.

Section 3.3.3 Quantum Confinement Effects

In this section, we consider quantum confinement effects on the dynamic THz response of the NWs. The basic argument is that the quantum confinement of carriers in the quasi-one-dimensional (1D) NWs can substantially modify the Coulomb interactions between the carriers and their THz absorption.

In Sections 3.3.1 and 3.3.2, we considered a bulk free-carrier response and a bulk exciton response contribution, respectively, to the dynamic THz response of the NWs. The main assumption in both types of response is that the NW dimensions are large enough to regard the NWs as a bulk semiconductor and ignore any modifications to their THz absorption. However, this assumption is not completely justified for the NW core diameters of a few tens of nanometers, which we study here. We mentioned before that previous electrical transport measurements [1, 2] have shown clear evidence for the existence of a confinement potential for carriers in the NWs, including the observation at low temperatures of well-controlled Coulomb blockade oscillations and conductance quantization, corresponding to ballistic transport through 1D subbands. These quantum confinement effects can substantially modify the Coulomb interactions between carriers, which will affect the dynamic THz response arising from both free carriers and electron-hole correlations (or excitons).

In this section, we consider the effects of quantum confinement on the dynamic THz response of the NWs. First, we determine the degree of quantum confinement of electrons and holes in the NWs. To find the confinement wavefunctions and energies, we solve the Schrödinger equation for a particle in a cylinder defining a potential structure with infinitely high walls, which is given by:

$$\left[-\frac{\hbar^2}{2m^*}\left(\frac{\partial^2}{\partial x^2}+\frac{\partial^2}{\partial y^2}\right)+V(x,y)\right]\xi_{l,m}(x,y)=\varepsilon_{l,m}\xi_{l,m}(x,y), \qquad (3.3.12)$$

where $\{l,m\}$ is the full set of subband quantum numbers. The wavefunctions are proportional to the Bessel functions of the first kind:

$$\xi_{l,m}(\rho,\varphi)=N_m J_m\left(\alpha_{l,m}\frac{\rho}{R}\right)e^{im\varphi}, \qquad (3.3.13)$$

where R is the NW radius and $\alpha_{l,m}$ is the l-th root of the m-th Bessel function. With the boundary conditions that the wavefunctions must vanish at the NW surface, the confinement energies are given by:

$$\varepsilon_{l,m} = \frac{\alpha_{l,m}^2}{R^2}\frac{\hbar^2}{2m^*}. \tag{3.3.14}$$

In Ge, the Γ valley is isotropic in both the conduction and the valence band, so that both the electron and the hole effective mass is the same in all directions. On the other hand, the L valley in the conduction band is highly anisotropic. The heavy electron effective mass, $m_{e,z}$, is parallel to the length of the NW in the [111] crystallographic direction, while the light electron effective mass, $m_{e,xy}$, is transverse, as illustrated schematically in Figure 3.3.11. The incident THz probe is also shown for both parallel and perpendicular polarization relative to the NW orientation, respectively. We note that because the quantum confinement in the NW is only in the transverse direction, the light electron effective mass needs to be used in the calculations for electrons in the L valley. Table 3.3.3 shows the electron and hole confinement energies for a few of the lowest subbands, which are calculated for a Ge NW with R = 10 nm. We observe that the energy spacing between the two lowest subbands for electrons is $\Delta\varepsilon^{e,L} \approx 41.6$ meV in the L valley and $\Delta\varepsilon^{e,\Gamma} \approx 82.7$ meV in the Γ valley, both of which are quantum confined even at room temperature of 300 K (≈ 25.8 meV). The energy spacing between the two lowest subbands for holes is $\Delta\varepsilon^{h,\Gamma} \approx 10.3$ meV in the Γ valley, which is much more weakly quantum confined. The direct and indirect excitons, having exciton binding energies of $E_B^{\Gamma} \approx 1.9$ meV and $E_B^{L} \approx 4.5$ meV, respectively, are also very strongly quantum confined. We note that the precise degree of quantum confinement depends critically on the NW radius, because the confinement energies scale inversely with its square.

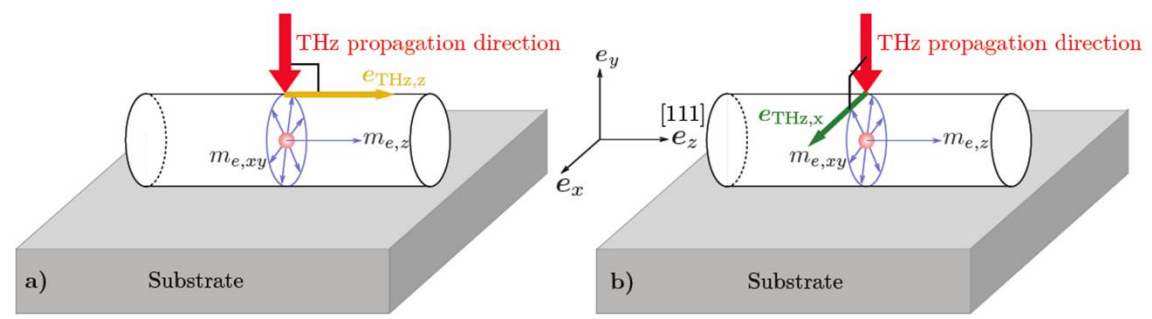

Figure 3.3.11 – Schematic diagram of the incident THz probe for (a) parallel and (b) perpendicular polarization relative to the NW orientation.

Table 3.3.3 – Electron and hole confinement energies calculated for a Ge NW with R = 10 nm.

Confinement energies of symmetric wavefunctions			
Quantum numbers $\{l, m\}$	Electrons in L valley $\varepsilon_{l,m}^{e,L}$ (meV)	Electrons in Γ valley $\varepsilon_{l,m}^{e,\Gamma}$ (meV)	Holes in Γ valley $\varepsilon_{l,m}^{h,\Gamma}$ (meV)
{1,0}	27.04	53.75	6.68
{2,0}	142.44	283.15	35.18

Confinement energies of antisymmetric wavefunctions			
Quantum numbers $\{l, m\}$	Electrons in L valley $\varepsilon_{l,m}^{e,L}$ (meV)	Electrons in Γ valley $\varepsilon_{l,m}^{e,\Gamma}$ (meV)	Holes in Γ valley $\varepsilon_{l,m}^{h,\Gamma}$ (meV)
{1,1}	68.65	136.46	16.95
{2,1}	230.11	457.42	56.83

Next, we investigate how the Coulomb potential of a 1D NW is modified due to its dielectric environment. To obtain the modifications to the Coulomb potential of a test charge q_j at a position $\boldsymbol{r}_j$ due to a dielectric background with a refractive index profile $n(\boldsymbol{r})$, we solve the Poisson equation, which is given by:

$$\nabla \cdot [n^2(\boldsymbol{r})\nabla V(\boldsymbol{r})] = -\frac{q_j}{\epsilon_0}\delta(\boldsymbol{r} - \boldsymbol{r}_j). \tag{3.3.15}$$

In the NW geometry, we have spherical symmetry around the longitudinal growth direction. We therefore define the dielectric background as:

$$\epsilon(\boldsymbol{r}) = n^2(\boldsymbol{r}) = 1 + F_0 e^{-r_{||}^2/\Delta R^2}, \tag{3.3.16}$$

where we decompose $\boldsymbol{r} = (\boldsymbol{r}_{||}, z)$ and introduce the width of the distribution ΔR. An abrupt change in the dielectric constant would lead to numerical difficulties, so we choose a soft wall function. After applying a Fourier transformation of Equation 3.3.15 and the convolution theorem, we obtain:

$$k^2 V_k + \sum_{\boldsymbol{k}'} F_{\boldsymbol{k}-\boldsymbol{k}'} V_{k'} \boldsymbol{k} \cdot \boldsymbol{k}' = \frac{q_j}{\epsilon_0 L^3} e^{-i\boldsymbol{k}\cdot\boldsymbol{r}_j}. \tag{3.3.17}$$

By combining Equations 3.3.15 and 3.3.17, assuming quasi-continuous bands ($\sum \rightarrow \int$) and solving the resulting integrals, we obtain:

$$(k_{||}^2 + k_z^2)V(k) + \frac{\Delta R^2 F_0}{2} \int k'_{||} dk'_{||} V(k'_{||}, k_z) \left[k_z^2 J_0\left(\frac{k_{||}k'_{||}}{2}\Delta R^2\right) + k_{||}k'_{||} J_1\left(\frac{k_{||}k'_{||}}{2}\Delta R^2\right)\right] = \frac{q_j}{\epsilon_0} e^{-i\left(k_{||}r_{j,||} + k_z r_{j,z}\right)}, \tag{3.3.18}$$

in which we used $L^3 V_k \rightarrow V(k)$ and J_n ($n = \{0,1\}$) are the Bessel functions of the first kind.

We can solve Equation 3.3.18 numerically to calculate the modifications to the Coulomb potential of the NWs. We discover that due to the quantum confinement, the relative dielectric constant ϵ_r of a Ge NW with R = 10 nm in the THz range is reduced from the bulk Ge value of $\epsilon_r \approx 16$ to $\epsilon_r \approx 1.5$, which is very close to that of free space. This large reduction of the relative dielectric constant constitutes a very substantial modification to the Coulomb interactions between carriers in the 1D NW geometry, which has a very strong impact on the THz response of both free carriers and electron-hole correlations (or excitons). We calculate that the 1s-to-2p transition energy of the indirect exciton E_{1s-2p} in a Ge NW with R = 10 nm shifts from the bulk Ge value of $E_{1s-2p} \sim 1$ THz to $E_{1s-2p} \sim 10$ THz, which is well beyond the accessible THz bandwidth. This strongly suggests that indirect excitons cannot account for the dynamic THz response of the NWs, when quantum

confinement effects are considered. In addition, the 2D quantum confinement of free carriers in the NWs results in different longitudinal and transversal dielectric functions seen by the incident THz probe for parallel and perpendicular polarization, respectively (see Figure 3.3.11), which is consistent with the observed highly anisotropic dynamic THz response of the NWs.

Section 3.4 Summary for Semiconductor Nanowires

In conclusion, we have studied the dynamic THz response and the hot-carrier dynamics of high quality single-crystal germanium (Ge) and germanium/silicon (Ge/Si) core/shell nanowires (NWs) following ultrafast photoexcitation using ultrafast time-resolved THz spectroscopy. First, we discussed the transient THz carrier dynamics of the NWs within the framework of a photoexcited carrier density model, in which the photoexcited THz conductivity of the NWs is directly proportional to the photoexcited carrier density. We explained the experimental data in the context of intraband carrier relaxation and interband carrier recombination processes. We observed clear evidence for ballistic carrier transport in the NWs. We also identified surface defect states as the dominant carrier recombination and scattering mechanism limiting carrier lifetime and transport in the NWs.

Then, we discussed the full dynamic THz response of the NWs to explain its microscopic origins. We considered three possible contributions including bulk free-carrier response, bulk exciton response and quantum confinement effects. First, by expanding the photoexcited carrier density model, we discussed how a bulk free-carrier model can account for the dynamic THz response of the NWs. We considered two types of bulk free-carrier response, given by the Drude-Plasmon and the Drude-Smith models, and how they agree with the measured differential THz transmission spectrum of the NWs. We discovered that both models can fit the experimental data equally well, while at the same time they entail completely different physical origins of the dynamic THz response of the NWs. The Drude-Plasmon model presumes that the pure Drude-like response observed in bulk semiconductors is modified by the existence of a surface plasmon resonance oscillations in the NW geometry due to the small volume-to-surface-area ratio. The Drude-Smith model presumes that the pure Drude-like response is modified by the strong carrier

backscattering off the NW walls. Both phenomenological models possess a reasonable inherent physical justification and appear consistent to a very similar degree with the experimental data, so that we cannot conclusively distinguish between the two. However, we also noted that any pure bulk free-carrier response cannot account completely for the finite rise time of the THz absorption of the NWs.

Then, we discussed a bulk exciton response contribution to the dynamic THz response of the NWs. Within this model, the finite rise time of the THz absorption is attributed to the built-up of electron-hole correlations (or excitons). We discovered that the indirect exciton in bulk Ge is consistent with the measured differential THz transmission spectrum of the NWs at cryogenic temperatures, but not at room temperature. However, we also noted that the indirect exciton transition energies are shifted to much higher values, when quantum confinement effects are considered, which strongly suggests that they cannot account for the dynamic THz response of the NWs.

Finally, we discussed quantum confinement effects on the dynamic THz response of the NWs. We discovered that the quantum confinement of carriers in the quasi-one-dimensional (1D) NWs can substantially modify the Coulomb interactions between carriers, which affects the dynamic THz response arising from both free carriers and electron-hole correlations (or excitons). The 2D quantum confinement results in different longitudinal and transversal dielectric functions seen by the incident THz probe for parallel and perpendicular polarization, respectively, which is consistent with the observed highly anisotropic dynamic THz response of the NWs. The precise theoretical and numerical details of a quantum confinement model, which can explain completely the true physics behind the dynamic THz response of the NWs, is still under work.

Section 3.5 References

[1] W. Lu et al., "One-dimensional hole gas in germanium/silicon nanowire heterostructures," *Proc. Natl. Acad. Sci. U.S.A.* **102**, 10046-10051 (2005).

[2] W. Lu and C. M. Lieber, "Semiconductor nanowires," *J. Phys. D: Appl. Phys.* **39**, 387-406 (2006).

[3] A. Javey, "Layer-by-Layer Assembly of Nanowires for Three-Dimensional, Multifunctional Electronics," *Nano Lett.* **7**, 773-777 (2007).

[4] M. Tinkham, "Energy gap interpretation of experiments on infrared transmission through superconducting films," *Phys. Rev.* **104**, 845-846 (1956).

[5] A. Urbanowicz et al., "Terahertz emission from photoexcited surfaces of Ge crystals," *Physica B* **367**, 152-157 (2005).

[6] R. P. Prasankumar et al., "Ultrafast Electron and Hole Dynamics in Germanium Nanowires," *Nano Lett.* **8**, 1619-1624 (2008).

[7] J. H. Strait et al., "Measurements of the Carrier Dynamics and Terahertz Response of Oriented Germanium Nanowires using Optical-Pump Terahertz-Probe Spectroscopy," *Nano Lett.* **9**, 2967-2972 (2009).

[8] K. Tanaka et al., "Determination of intervalley scattering time in germanium by subpicosecond time-resolved Raman spectroscopy," *Phys. Rev. Lett.* **71**, 1935-1938 (1993).

[9] G. Mak and H. M. van Driel, "Femtosecond transmission spectroscopy at the direct band-edge of germanium," *Phys. Rev. B* **49**, 16817-16820 (1994).

[10] X. Q. Zhou et al., "Femtosecond kinetics of photoexcited carriers in germanium," *Phys. Rev. B* **50**, 5226-5230 (1994).

[11] D. W. Bailey and C. J. Stanton, "Calculations of femtosecond differential optical transmission in germanium," *J. Appl. Phys.* **77**, 2107-2115 (1995).

[12] S. Zollner et al., "Femtosecond interband hole scattering in Ge studied by pump-probe reflectivity," *Solid State Commun.* **104**, 51-55 (1997).

[13] M. Woerner et al., "Ultrafast thermalization of nonequilibrium holes in p-type germanium studied by femtosecond infrared spectroscopy," *Phys. Rev. B* **49**, 17007-17010 (1994).

[14] K. Tanaka et al., "Subpicosecond hot-hole relaxation in germanium studied by time-resolved inter-valence-band Raman scattering," *Phys. Rev. B* **52**, 10709-10712 (1995).

[15] E. Gaubas et al., "Carrier lifetime studies in Ge using microwave and infrared light techniques," *Mat. Sci. Semicon. Proc.* **9**, 781-787 (2006).

[16] G. Williams and D. C. Watts, "Non-symmetrical dielectric relaxation behaviour arising from a simple empirical decay function," *Trans. Faraday Soc.* **66**, 80-85 (1970).

[17] J. Kakalios et al., "Stretched-exponential relaxation arising from dispersive diffusion of hydrogen in amorphous silicon," *Phys. Rev. Lett.* **59**, 1037-1040 (1987).

[18] K. C. Benny Lee et al., "Application of the Stretched Exponential Function to Fluorescence Lifetime Imaging," *Biophys. J.* **81**, 1265-1274 (2001).

[19] D. C. Johnston et al., "Dynamics of Magnetic Defects in Heavy Fermion LiV_2O_4 from Stretched Exponential ^{7}Li NMR Relaxation," *Phys. Rev. Lett.* **95**, 176408 (2005).

[20] D. C. Johnston, "Stretched exponential relaxation arising from a continuous sum of exponential decays," *Phys. Rev. B* **74**, 184430 (2006).

[21] R. Calarco et al., "Size-dependent Photoconductivity in MBE-Grown GaN-Nanowires," *Nano Lett.* **5**, 981-984 (2007).

[22] L. Li et al., "Observation of Hole Accumulation in Ge/Si Core/Shell Nanowires Using off-Axis Electron Holography," *Nano Lett.* **11**, 493-497 (2011).

[23] H. Roskos et al., "Cooling of a carrier plasma in germanium investigated with subpicosecond infrared pulses," *Appl. Phys. Lett.* **53**, 2406-2408 (1988).

[24] P. Yu and M. Cardona, "Fundamentals of Semiconductors: Physics and Materials Properties," Springer-Verlag Berlin Heidelberg, ISBN: 978-3-642-00709-5, Edition 4 (2010).

[25] D. Grischkowsky et al., "Far-infrared time-domain spectroscopy with terahertz beams of dielectrics and semiconductors," *J. Opt. Soc. Am. B* **7**, 2006-2015 (1990).

[26] W. Zhang et al., "Terahertz studies of carrier dynamics and dielectric response of n-type, freestanding epitaxial GaN," *Appl. Phys. Lett.* **82**, 2841-2843 (2003).

[27] J. Lloyd-Hughes and T.-I. Jeon, "A Review of the Terahertz Conductivity of Bulk and Nano-Materials," *J. Infrared Milli. Terahz. Waves* **33**, 871-925 (2012).
[28] H.-K. Nienhuys and V. Sundström, "Influence of plasmons on terahertz conductivity measurements," *Appl. Phys. Lett.* **87**, 012101 (2005).
[29] P. Parkinson et al., "Transient Terahertz Conductivity of GaAs Nanowires," *Nano Lett.* **7**, 2162-2165 (2007).
[30] P. Parkinson et al., "Carrier Lifetime and Mobility Enhancement in Nearly Defect-Free Core-Shell Nanowires Measured Using Time-Resolved Terahertz Spectroscopy," *Nano Lett.* **9**, 3349-3353 (2009).
[31] P. Parkinson et al., "Noncontact Measurement of Charge Carrier Lifetime and Mobility in GaN Nanowires," *Nano Lett.* **12**, 4600-4604 (2012).
[32] H. J. Joyce et al., "Ultralow Surface Recombination Velocity in InP Nanowires Probed by Terahertz Spectroscopy," *Nano Lett.* **12**, 5325-5330 (2012).
[33] H. J. Joyce et al., "Electronic properties of GaAs, InAs and InP nanowires studied by terahertz spectroscopy," *Nanotechnology* **24**, 214006 (2013).
[34] H. Tang et al., "Carrier Dynamics in Si Nanowires Fabricated by Metal-Assisted Chemical Etching," *ACS Nano* **6**, 7814-7819 (2012).
[35] K. S. Cole and R. H. Cole, "Dispersion and Absorption in Dielectrics I. Alternating Current Characteristics," *J. Chem. Phys.* **9**, 341-351 (1941).
[36] D. W. Davidson and R. H. Cole, "Dielectric Relaxation in Glycerol, Propylene Glycol, and n-Propanol," *J. Chem. Phys.* **19**, 1484-1490 (1951).
[37] T.-I. Jeon and D. Grischkowsky, "Nature of Conduction in Doped Silicon," *Phys. Rev. Lett.* **78**, 1106-1109 (1997).
[38] M. C. Beard et al., "Transient photoconductivity in GaAs as measured by time-resolved terahertz spectroscopy," *Phys. Rev. B* **62**, 15764-15777 (2000).
[39] S. Havriliak and S. Negami, "A complex plane representation of dielectric and mechanical relaxation processes in some polymers," *Polymer* **8**, 161-210 (1967).
[40] N. V. Smith, "Classical generalization of the Drude formula for the optical conductivity," *Phys. Rev. B* **64**, 155106 (2001).
[41] M. C. Beard et al., "Electronic Coupling in InP Nanoparticle Arrays," *Nano Lett.* **3**, 1695-1699 (2003).
[42] J. B. Baxter and C. A. Schmuttenmaer, "Conductivity of ZnO Nanowires, Nanoparticles, and Thin Films Using Time-Resolved Terahertz Spectroscopy," *J. Phys. Chem. B* **110**, 25229-25239 (2006).
[43] D. G. Cooke et al., "Transient terahertz conductivity in photoexcited silicon nanocrystal films," *Phys. Rev. B* **73**, 193311 (2006).
[44] K. Shimakawa et al., "The origin of non-Drude terahertz conductivity in nanomaterials," *Appl. Phys. Lett.* **100**, 132102 (2012).
[45] M. Lim et al., "Terahertz time-domain spectroscopy of anisotropic complex conductivity tensors in silicon nanowire films," *Appl. Phys. Lett.* **100**, 211102 (2012).
[46] M. Li, "Size and surface effects on transient photoconductivity in CdS nanobelts probed by time-resolved terahertz spectroscopy," *Appl. Phys. Lett.* **101**, 091104 (2012).
[47] J. M. Pitarke, "Theory of surface plasmons and surface-plasmon polaritons," *Rep. Prog. Phys.* **70**, 1-87 (2007).
[48] P. Tognini et al., "Ultrafast carrier dynamics in germanium nanoparticles," *Appl. Phys. Lett.* **75**, 208-210 (1999).
[49] S. Stagira et al., "Ultrafast measurements and modeling of electron relaxation in germanium nanoparticles," *Phys. Rev. B* **62**, 10318-10323 (2000).
[50] SchmuttenmaerNanoLett2002 M. C. Beard et al., "Size-Dependent Photoconductivity in CdSe Nanoparticles as Measured by Time-Resolved Terahertz Spectroscopy," *Nano Lett.* **2**, 983-987 (2002).
[51] E. G. Barbagiovanni et al., "Quantum confinement in Si and Ge nanostructures," *J. Appl. Phys.* **111**, 034307 (2012).
[52] O. Madelung, "Semiconductors: Data Handbook," Springer-Verlag Berlin Heidelberg, ISBN: 978-3-540-40488-0, Edition 3 (2004).
[53] M. Kira et al., "Microscopic theory of the semiconductor terahertz response," *Phys. Stat. Sol. B* **238** (3), 443-450 (2003).

[54] M. Kira and S.W. Koch, "Microscopic theory of optical excitations, photoluminescence, and terahertz response in semiconductors," *Eur. Phys. J. D* **36**, 143-157 (2005).
[55] M. Kira and S.W. Koch, "Many-body correlations and excitonic effects in semiconductor spectroscopy," *Prog. Quant. Electron.* **30**, 155-296 (2006).
[56] R. A. Kaindl et al., "Ultrafast terahertz probes of transient conducting and insulating phases in an electron-hole gas," *Nature* **423**, 734-738 (2003).
[57] R. A. Kaindl et al., "Transient terahertz spectroscopy of excitons and unbound carriers in quasi-two-dimensional electron-hole gases," *Phys. Rev. B* **79**, 045320 (2009).
[58] M. Kubouchi et al., "Study of Orthoexciton-to-Paraexciton Conversion in Cu_2O by Excitonic Lyman Spectroscopy," *Phys. Rev. Lett.* **94**, 016403 (2005).
[59] T. Suzuki and R. Shimano, "Time-Resolved Formation of Excitons and Electron-Hole Droplets in Si Studied Using Terahertz Spectroscopy," *Phys. Rev. Lett.* **103**, 057401 (2009).
[60] S. Zwerdling et al., "Exciton and Magneto-Absorption of the Direct and Indirect Transitions in Germanium," *Phys. Rev.* **114**, 80-89 (1959).
[61] G. G. Macfarlane at al., "Exciton and phonon effects in the absorption spectra of germanium and silicon," *J. Phys. Chem. Solids* **8**, 388-392 (1959).
[62] S. Zwerdling et al., "The direct and indirect transition excitons in germanium," *J. Phys. Chem. Solids* **8**, 397-400 (1959).
[63] T. P. Mclean and R. Loudon, "Exciton energy levels in germanium and silicon," *J. Phys. Chem. Solids* **13**, 1-9 (1960).
[64] T. Nishino et al., "Indirect exciton absorption in germanium," *J. Phys. Soc. Jpn.* **37** (4), 1016-1023 (1974).

Chapter 4
Conclusions and Further Directions

Section 4.1 Conclusions

Nanotechnology has recently enjoyed a tremendous scientific and engineering interest stimulated largely by the need for ever smaller and faster electronic and photonic devices and systems. Many emerging nanoscale and low-dimensional materials and devices, which hold promise to revolutionize and extend the semiconductor technology past its present limitations, are currently under active investigation.

In this dissertation, I studied systematically the physics of the ultrafast terahertz (THz) response and the hot-carrier relaxation and cooling dynamics in two sample classes of state-of-the-art nanoscale low-dimensional materials, namely graphene and semiconductor nanowires, by using ultrafast time-resolved THz spectroscopy. I looked specifically first at a wide variety of high quality graphene, including epitaxial and chemical-vapor-deposited (CVD), and second at high quality single-crystal germanium (Ge) and germanium/silicon (Ge/Si) core/shell nanowires (NWs). Both graphene and semiconductor nanowires have shown remarkable technological potential and have attracted enormous attention. The design and development of novel nanoelectronic and nanophotonic devices based on these materials and operating into the THz frequencies necessitates thorough understanding of the physics of their dynamic THz response and hot-carrier dynamics. Ultrafast time-resolved THz spectroscopy is an excellent experimental technique to provide such essential insight into the electronic and optical properties of nanoscale low-dimensional materials and to explore their device applications at THz frequencies. Here I list the major conclusions and accomplishments.

The conclusions for graphene include:

- The dynamic THz response of pristine epitaxial and CVD graphene is remarkably dispersionless in the detectable frequency range of ~0.2-2.5 THz under all experimental conditions. This response is qualitatively consistent with the simple Drude model and is characteristic for a pristine graphene layer with very low disorder.
- In pristine epitaxial and CVD graphene, the THz carrier dynamics depend critically on the doping density. The carrier relaxation times range from a few picoseconds in graphene with high doping of $\geq 10^{12}$ cm^{-2} to hundreds of picoseconds in graphene with very low doping of $\leq 10^{10}$ cm^{-2}. A microscopic density-matrix theory of carrier-carrier and carrier-phonon interactions accounts quantitatively for all experimental results without the need for any fitting parameters, phenomenological models or extrinsic effects such as disorder. Physically, the high-energy tail of the hot-carrier distribution relaxes via the emission of optical phonons, and the carrier-carrier scattering processes very efficiently and continuously rethermalize the carrier population. A Drude model approximation is only semi-qualitatively consistent with the data, but the full microscopic theory is required to explain the data quantitatively under all experimental conditions.
- In multilayer epitaxial graphene with a few highly doped and many lightly doped layers, the THz carrier dynamics at very low carrier energies slow down with the number of layers. The low-energy carrier relaxation times in the lightly doped layers extend up to hundreds of picoseconds and are consistent with a first-principles theory of hot-carrier equilibration based on interlayer energy transfer via screened Coulomb interactions. Physically, the hot carriers in the lightly doped layers cool down by scattering with and transferring their energy to the cold carriers in the highly doped layers, which act as a Coulomb-coupled heat sink. The interlayer energy transfer theory can account for all experimental trends without the need for any fitting parameters.
- In buckled epitaxial graphene, in which an energy gap of up to ~0.7 eV has been carefully engineered, the THz carrier dynamics are up to two orders of magnitude faster relative to pristine epitaxial graphene under identical experimental conditions. The carrier relaxation times are sub-picosecond under all experimental

conditions and are attributed to large enhancement of the phase-space available for carrier scattering due to the finite bandgap. Physically, the hot electrons and holes recombine across the strongly non-homogenously broadened bandgap via the emission of optical phonons, and the carrier-carrier scattering processes very efficiently and continuously rethermalize the carrier population.

- In epitaxial graphene nanoribbons, in which carriers are carefully quantum confined in two dimensions (2D), the THz carrier dynamics exhibit a pronounced anisotropy with the THz polarization relative to the nanoribbons orientation. The carrier lifetimes in the high-energy subbands extend up to on the order of a hundred picoseconds, which is a clear manifestation of the strong quantum confinement effects in the exceptionally high quality nanoribbons.

The conclusions for semiconductor nanowires include:

- The THz carrier dynamics of Ge and Ge/Si core/shell NWs are characterized by fast few-picosecond intraband carrier relaxation followed by slower sub-nanosecond interband carrier recombination processes. In both Ge and Ge/Si NWs, the recombination times scale linearly with the NW core diameter, which is a clear evidence for ballistic carrier transport on tens of nanometers. Surface defect states are identified as the dominant carrier recombination and scattering mechanism limiting carrier lifetime and transport. Physically, carriers scatter many times off the NW walls before they are captured by a surface defect state and recombine. The recombination times of Ge NWs are about an order of magnitude longer than those of Ge/Si NWs under identical experimental conditions, which is attributed to higher surface defect density at the Ge/Si interface.
- The dynamic THz response of Ge and Ge/Si core/shell NWs exhibits a pronounced anisotropy with the THz polarization relative to the NW orientation. Furthermore, the response is qualitatively inconsistent with the simple Drude model by having a resonance-like shape with a peak at a finite THz frequency. Three possible physical origins of the response were considered including bulk free-carrier response, bulk exciton response and quantum confinement effects.

- First, the dynamic THz response of the NWs was considered within the framework of two types of bulk free-carrier response, given by the Drude-Plasmon and the Drude-Smith models. The Drude-Plasmon model presumes that the pure Drude-like response observed in bulk semiconductors is modified by the existence of a surface plasmon resonance oscillations in the NW geometry due to the small volume-to-surface-area ratio. The Drude-Smith model presumes that the pure Drude-like response is modified by the strong carrier backscattering off the NW walls. Both phenomenological models can fit the experimental data equally well, but fail to account for the finite rise time of the dynamic THz response.
- Second, the dynamic THz response of the NWs was considered within the framework of a bulk exciton response. Within this model, the finite rise time of the dynamic THz response is attributed to the built-up of electron-hole correlations. The indirect exciton in bulk Ge is qualitatively consistent with the experimental data at cryogenic temperatures, but fails at room temperature.
- Third, quantum confinement effects on the dynamic THz response of the NWs were considered. The Coulomb interactions between carriers are substantially modified in the quasi-one-dimensional (1D) NW geometry, which affects the dynamic THz response arising from both free carriers and electron-hole correlations. This results in different longitudinal and transversal dielectric functions seen by the incident THz radiation for parallel and perpendicular polarization, respectively, which is qualitatively consistent with the observed highly anisotropic dynamic THz response.

Section 4.2 Further Directions

The field of novel nanoscale and low-dimensional materials and devices is rapidly growing at an ever accelerating pace. Therefore, there are plenty of opportunities for new research studies and exploration. Here I list some further directions for future work.

- The THz carrier dynamics of buckled epitaxial graphene are substantially faster than pristine epitaxial graphene due to the finite, but non-homogenous bandgap. It will be very interesting to study the THz carrier dynamics of buckled epitaxial graphene or other semiconducting forms of graphene with larger and more

homogenous bandgaps. It can be expected that in such semiconducting graphene the carrier relaxation times could be much longer than in metallic graphene, because optical phonon emission should be strongly suppressed, when the optical phonon energy is smaller than the bandgap energy. Thus, the carrier relaxation times could be tuned by many orders of magnitude by carefully controlling the size of the graphene bandgap.

- The THz carrier dynamics of epitaxial graphene nanoribbons are substantially modified due to the 2D quantum confinement and the carrier lifetimes in the high-energy subbands extend up to on the order of a hundred picoseconds. It will be very interesting to study the THz carrier dynamics in a wider array of epitaxial graphene nanoribbons including different physical dimensions and types of edges. By carefully tuning these physical parameters, both the edge state and inter-subband transitions in graphene nanoribbons could be probed, and the physical mechanisms responsible for the THz carrier dynamics could be investigated.
- Three possible physical origins of the dynamic THz response of Ge and Ge/Si core/shell NWs were considered. Quantum confinement effects were found to be important and qualitatively consistent with the dynamic THz response, but a theory which agrees quantitatively with the experimental data is still under work. It will be essential to develop the precise theoretical and numerical details of a quantum confinement model, which can explain completely the true physics behind the dynamic THz response under all experimental conditions. It will be also very interesting to study a wider array of NWs including different composition and doping density, and more complex physical structure (e.g. multi-shell, multi-segment, p-n junctions, etc.).
- The ultrafast time-resolved THz spectroscopy is a powerful experimental technique, which can be applied to study the dynamic THz response and the hot-carrier dynamics in the vast variety of emerging nanoscale and low-dimensional materials, including transition metal dichalcogenides (e.g. MoS_2, $MoSe_2$, WS_2, and WSe_2), topological insulators, multilayered and other van der Waals heterostructures.